10-30-2020

Gold mineralization in the Archean Wawa Gold Corridor, Wawa, Ontario

Elliot Andrew Wehrle
University of Windsor

Gold mineralization in the Archean Wawa Gold Corridor, Wawa, Ontario

By

Elliot A. Wehrle

A Thesis

Submitted to the Faculty of Graduate Studies
through the School of the Environment
in Partial Fulfillment of the Requirements for
the Degree of Master of Science
at the University of Windsor

Windsor, Ontario, Canada

2020

Gold mineralization in the Archean Wawa Gold Corridor, Wawa, Ontario

by

Elliot A. Wehrle

APPROVED BY:

_____

D. Kontak
Laurentian University

_____

T.J. Hammond
Department of Physics

_____

J. Gagnon
School of the Environment

_____

I. Samson, Advisor
School of the Environment

August 26, 2020

DECLARATION OF ORIGINALITY

I hereby certify that I am the sole author of this thesis and that no part of this thesis has been published or submitted for publication.

I certify that, to the best of my knowledge, my thesis does not infringe upon anyone's copyright nor violate any proprietary rights and that any ideas, techniques, quotations, or any other material from the work of other people included in my thesis, published or otherwise, are fully acknowledged in accordance with the standard referencing practices. Furthermore, to the extent that I have included copyrighted material that surpasses the bounds of fair dealing within the meaning of the Canada Copyright Act, I certify that I have obtained a written permission from the copyright owner(s) to include such material(s) in my thesis and have included copies of such copyright clearances to my appendix.

I declare that this is a true copy of my thesis, including any final revisions, as approved by my thesis committee and the Graduate Studies office, and that this thesis has not been submitted for a higher degree to any other University or Institution.

ABSTRACT

The Wawa Gold Corridor (WGC), located in the Michipicoten greenstone belt, comprises Au-bearing shear zones that crosscut the 2.75 Ga Jubilee Stock. Shear zones formed during protracted deformation (D_1 – D_3) and contain Au mineralization produced by two major events. The first comprises syn-deformation gold with arsenopyrite and pyrite in D_1 – D_2 schists and the second comprises post-deformation gold with Bi-Te minerals, chalcopyrite, and pyrite in carbonate ± riebeckite alteration rims around pyrite in D_3 shear veins. Observations of porosity and inclusions in D_1 arsenopyrite and D_2 pyrite suggest that these sulfides underwent coupled dissolution-precipitation reactions (CDR). Based on trace-element analysis by laser-ablation inductively-coupled plasma mass spectrometry, it is evident that the replacement of Au-rich minerals by Au-poor minerals during CDR generated native gold from Au previously in solid-solution. Textural relationships amongst gold and Bi-Te minerals are consistent with precipitation from a Bi-rich polymetallic melt during the second gold event. The rare presence of riebeckite in the siderite-rich coronae that host Au-Bi-Te assemblages suggests that this event was associated with the emplacement of 1.0 Ga lamprophyre dikes. However, overlap in the $\delta^{34}S$ values of pyrite in this event (0.4 – 2.4 ‰) with those of earlier pyrite (0.1 – 4.1 ‰) indicate recycling of pre-existing sulfide sulfur during the 1.0 Ga hydrothermal overprint. By comparing the Au contents of arsenopyrite (10s – 1,000s of ppm) to those of pyrite (<0.01 – 10s of ppm), it is determined that despite the textural and temporal variance with which gold occurs, almost all of the gold in the system originated as solid-solution Au in D_1 arsenopyrite. This work therefore highlights

the importance of discriminating between the introduction of new Au and the redistribution of existing Au within a deposit, an intricacy that can be resolved using mineral-chemical analysis and mass-balance calculations.

DEDICATION

To Mom and Gabriele, my favourite scientists.

ACKNOWLEDGEMENTS

I am grateful to Iain Samson, who helped me take important steps towards integrating passionate creativity with responsible and measured thinking. I am a better scientist now than I was two years ago, and I owe that to him. I want to thank Dan Kontak for his unending reservoir of questions designed to get me thinking outside of my box.

This project would not have been possible without the enthusiasm and expertise of JF Montreuil. Thank you for helping me to develop into a geologist who is occasionally able to recognize lineations in the field. Equally, I am indebted to Conrad Dix for his support and mentorship over the past two years.

The team at Red Pine Exploration was an endless source of help and moral support during my stints in the field. To Adam Clough, Rob Dyer, Naomi Jonker, Pat Lambert, Blake Mclaughlin, Wilkie Langille, Pete Olafson, Ruth Orloci-Goodison, Tim Porter, Olga Pridhodko, Jon Savard, Jolee Stewart, Nick Wray, and Dominique van der Byl: thanks for bringing some pizazz to my life in Wawa.

My sanity was maintained in no small part by Patrik Schmidt, Jordan Watts, Paul Sotiriou, Jim Greene, Jason Willson, and Namir Al-Aasm. Thanks for talking shop, and also for the parts where we didn't talk shop. To Melissa Price, thanks for commiserating with me when things went wrong, and for making sure they went right eventually. I also want to acknowledge Sharon Lackie and JC Barrette for their guidance in the lab.

Finally, thanks to Gabriele Wehrle for helping me balance basic redox equations, and to Charlotte Stone for being a more-or-less adequate friend.

TABLE OF CONTENTS

LIST OF TABLES

LIST OF FIGURES

LIST OF APPENDICES

LIST OF ABBREVIATIONS/SYMBOLS

ABG = Abitibi greenstone belt

Apy = arsenopyrite

BSE = back-scattered electron

Bsm = bismuthinite

Bt = biotite

Cal = calcite

Ccp = chalcopyrite

Chl = chlorite

Dol = dolomite

EDS = energy-dispersive X-ray spectroscopy

Ing = ingodite

ICP = Inductively coupled plasma spectroscopy

ICP-MS = Inductively coupled plasma mass-spectrometry

INAA = Instrumental neutron activation analysis

IRMS = isotope ratio mass spectrometry

Jon = jonassonite

LA-ICP-MS = laser ablation inductively coupled plasma mass-spectrometry

LOD = level of detection

MGB = Michipicoten greenstone belt

Mld = maldonite

Ms = muscovite

Po = pyrrhotite

Py = pyrite

Qz = quartz

Rbk = riebeckite

Sd = siderite

SEM = scanning electron microscope

SIMS = secondary ion mass spectrometry

Tsm = tsumoite

WGC = Wawa Gold Corridor

CHAPTER ONE – INTRODUCTION

1.1 – Introduction

Shear zone-hosted lode gold deposits (a descriptive term that includes mesothermal and orogenic gold deposits) in Archean greenstone belts are a globally important source of gold. Decades of research and exploration have successfully established the broad tectonic, structural, and mineralogical characteristics of these systems. They form in collisional environments and experience protracted deformation in the brittle-ductile regime (cf. Groves et al. 1998, Goldfarb et al. 2005). Numerous pulses of fluid flow (cf. Sibson et al. 1988) are channelled along actively deforming structures and stabilize, among others, hydrothermal quartz, phyllosilicates, carbonates, sulfides, and gold. The deformational processes responsible for the formation of shear-zone hosted lode gold deposits are regional in nature, and so multiple deposits tend to form contemporaneously along crustal-scale structural systems (Groves et al. 1987, Beirlein et al. 2006). Thus, individual gold deposits are typically grouped into broader gold provinces or camps, with a world-class example being the Neoarchean Abitibi gold province in northern Ontario and Québec (Robert 2001, Bateman et al. 2008).

Much of the modern research on gold deposits has shifted to the micro-scale and is focused around two complex issues that can be summarized by asking: (1) how do large amounts of Au (i.e., several to thousands of ppm) end up in small volumes of rock (on the scale of several cubic metres)? and (2) where do the fluids that carry Au come from? The first of these issues pertains to the fact that a typical fluid that passes through a shear zone-hosted lode gold deposit does not have adequate concentrations of Au to directly precipitate the volumes of native gold often

observed (Gammons & Williams-Jones 1997, Williams-Jones et al. 2009, Hastie et al. 2020). The second is borne out of the fact that fluids from the two most likely source reservoirs (magmas and metamorphic devolatilization) are indistinguishable in terms of their isotopic signatures and salinities (characteristics often used to identify fluid source in other environments; Goldfarb and Groves 2015).

Gold in shear zone-hosted lode gold deposits is regularly associated with Fe-As sulfide minerals (e.g., pyrite, arsenopyrite) and so these minerals have been interrogated using a variety of micro-analytical techniques in an effort to address the questions posed above. Such studies have determined that both arsenopyrite and pyrite can dissolve orders of magnitude more Au than the hydrothermal fluids from which they precipitate (e.g., Reich et al. 2005, Deditius et al 2014). It has therefore been suggested that the incorporation of Au into these phases during sulfide crystallization is a fundamental prerequisite to the formation of high-grade deposits (cf. Morey et al. 2008, Cook et al. 2013, Lawley et al. 2017, Hastie et al. 2020). Subsequent destruction of these Au-bearing sulfides during deformation or hydrothermal alteration might also enable the liberation of Au from the sulfide and formation of native gold. A second model for the generation of abundant native gold in shear zone-hosted gold deposits involves the precipitation of gold from a fluid phase that can dissolve substantially more Au than a typical aqueous-carbonic fluid: low melting point chalcophile element (LMCE; e.g., Bi, Te, Sb, Pb) polymetallic melts (e.g., Douglas et al. 2000, Tooth et al. 2008, Tooth et al. 2011). The importance of polymetallic melts in the formation of high-grade gold deposits has been documented in other environments like skarns (e.g., Cepedal et al. 2006, Cockerton and Tomkins 2012) and porphyry-epithermal systems (e.g., Zhou et al. 2016, 2018), but their role in the genesis of gold in shear zone-hosted lode gold deposits is not as well-constrained (e.g., Oberthür and Weiss 2008, Kerr et al. 2018, Hastie et al. 2020).

In fact, the occurrence of Au with LMCEs is also relevant to the second issue, that being the original source of Au-bearing fluids. Whether they precipitated from melts or not, Au-LMCE mineral assemblages are regularly documented in magmatic-hydrothermal environments, leading to the hypothesis that such an association in a shear zone-hosted lode gold deposit may be indicative of a magmatic-hydrothermal source (e.g., Oberthür and Weiss 2008, Voudouris et al. 2013, Ilmen et al. 2015, Liu et al. 2019). The presence of this geochemical association within single grains of pyrite has equally been proposed as a method of fingerprinting a magmatic-hydrothermal contributions of ore elements (e.g., Mathieu 2019).

The present study investigates Au mineralization in the Wawa Gold Corridor (WGC), a shear zone-hosted lode gold deposit located in the Neoarchean Michipicoten greenstone belt (MGB). The MGB hosts several other gold deposits, but an understanding of the regional processes that formed these systems is hampered by a relatively small number of studies (cf. Callan and Spooner 1988, Samson et al. 1997 Haroldson 2014, McDivitt et al. 2017, 2018, 2020, Jellico 2019, Ciufo 2019). The objectives of this work are to characterize the process(es) by which Au mineralization occurred in the WGC, to test the hypothesis that sulfide minerals can account for the volume of native gold presently observed in the deposit, and to evaluate if the geochemical and mineralogical associations of Au mineralization can be used to infer fluid source. In doing so, this work will help to establish a regional model for Au mineralization in the MGB and advance the understanding of the micro-scale processes that control Au mineralization in shear zone-hosted lode gold systems.

1.2 – References

Bateman, R., Ayer, J.A., and Dubé, B., 2008, The Timmins-Porcupine Gold Camp, Ontario: Anatomy of an Archean Greestone Belt and Ontogeny of Gold Mineralization: Economic Geology, v. 103, p. 1285-1308.

Beirlein, F.P., Groves, D.I., Goldfarb, R.J., and Dubé, B., 2006, Lithospheric controls on the formation of provinces hosting giant orogenic gold deposits: Mineralium Deposita, v. 40, p. 874-886.

Callan, N.J., and Spooner, E.T.C., 1988, Repetitive hydraulic fracturing and shear zone inflation in an Archean granitoid-hosted, ribbon banded, Au-quartz vein system, Renabie area, Ontario, Canada: Ore Geology Reviews, v. 12, p. 237-266.

Cepedal, A., Fuertes-Fuente, M., Martín-Izard, A., González-Nistal, S., and Rodríguez-Pevida, L., 2006, Tellurides, selenides and Bi-mineral assemblages from the Río Narcea Gold Belt, Asturias, Spain: genetic implications in Cu-Au and Au skarns: Mineralogy and Petrology, v. 87, p. 277-304.

Cockerton, A.B.D, and Tomkins, A.G., 2012, Insights into the Liquid Bismuth Collector Model Through Analysis of the Bi-Au Stormont Skarn Prospect, Northwest Tasmania: Economic Geology, v. 107, 667-682.

Douglas, N., Mavrogenes, J., Hack, A., and England, R., 2000, The liquid bismuth collector model: An alternative gold deposition mechanism, *in* Skilbeck, C.G., and Hubble, T.C.T., eds., Understanding planet Earth; searching for a sustainable future; on the starting blocks of the third millennium: Australian Geological Convention, 15th, Sydney, Abstracts: Sydney, Geological Society of Australia, 135 p.

Ilmen, S., Alansari, A., Bajddi, A., and Maacha, L., 2015, Cu-Au vein mineralization related to the Talat n'Imjjad shear zone (western High Atlas, Morocco): geological setting, ore mineralogy, and geochemical evolution: Arabian Journal of Geosciences, v. 8, p. 5039-5056.

Ciufo, T.J., 2019, Hydrothermal Alteration and Exploration Vectors at the Island Gold Deposit, Michipicoten Greenstone Belt, Wawa, Ontario: Unpublished M.Sc. thesis, Waterloo, University of Waterloo, 523 p.

Cook, N.J., Ciobanu, C.L., Meria, D., Silcock, D., and Wade, B., 2013, Arsenopyrite-Pyrite Association in an Orogenic Gold Ore: Tracing Mineralization History from Textures and Trace Elements: Economic Geology, v. 108, p. 1273-1283.

Deditius, A.P., Reich, M., Kesler, S.E., Utsunomiya, S., Chryssoulis, S.L., Walshe, J., and Ewing, R.C., 2014, The coupled geochemistry of Au and As in pyrite from hydrothermal ore deposits: Geochimica et Cosmochimica Acta, v. 140, p. 644-670.

Gammons, C.H., and Williams-Jones, A.E., 1997, Chemical Mobility of Gold in the Porphyry-Epithermal Environment: Economic Geology, v. 92, p. 45-59.

Goldfarb, R.J., Baker, T., Dubé, B., Groves, D.I., Hart, C.J.R., and Gosselin, P., 2005, Distribution, character, and genesis of gold deposits in metamorphic terranes: Economic Geology 100th Anniversary Volume, p. 407–450.

Goldfarb, R.J., and Groves, D.I., 2015, Orogenic gold: Common or evolving fluid and metal sources through time: Lithos, v. 233, 2-26.

Groves, D.I., Phillips, N., Ho, S.E., Houstoun, S.M., and Standing, C.A., 1987, Craton-Scale Distribution of Archean Greenstone Gold Deposits: Predictive Capacity of the Metamorphic Model: Economic Geology, v. 82, p. 2045-2058.

Groves, D.I., Goldfarb, R.J., Gebre-Mariam, M., Hagemann, S.G., and Robert, F., 1998, Orogenic gold deposits: A proposed classification in the context of their crustal distribution

Haroldson, E.L., 2014, Fluid inclusions and stable isotope study of magino; a magmatic related Archean gold deposit: Unpublished M.Sc. thesis, Madison, University of Wisconsin-Madison, 81 p.

Hastie, E.C.G., Kontak, D.J., and Lafrance, B., 2020, Gold Remobilization: Insights from Gold Deposits in the Archean Swayze Greenstone Belt, Abitibi Subprovince, Canada: Economic Geology, v. 115(2), p. 241-277.

Jellicoe, K., 2019, Structural Controls and Deformation History of the Orogenic Island Gold Deposit, Michipicoten Greenstone Belt, Ontario: Unpublished M.Sc. thesis, Waterloo, University of Waterloo, 84 p.

Kerr, M.J., Hanley, J.J., Kontak, D.J., Morrison, G.G., Petrus, J., Fayek, M., and Zajacz, Z., 2018, Evidence of upgrading gold tenor in an orogenic quartz-carbonate vein system by late magmatic-hydrothermal fluids at the Madrid Deposit, Hope Bay Greenstone Belt, Nunavut, Canada: Geochimica et Cosmochimica Acta, v. 241, p. 180-218.

Lawley, C.J.M., Jackson, S., Yang, Z., Davis, W., and Eglington, B., 2017, Tracing the Transition of Gold from Source to Sponge to Sink: Economic Geology, v. 112, p. 169-183.

Liu, J., Wang, Y., Huang, S., Wei, R., Sun, Z., Hu, Q., and Hao, J., 2019, The gold occurrence in pyrite and Te-Bi mineralogy of the Fancha gold deposit, Xiaoqinling gold field, southern margin of the North China Craton: Implication for ore genesis: Geological Journal, p. 1-21, doi: 10.1002/gj.3637

Mathieu, L., 2019, Detecting magmatic-derived fluids using pyrite chemistry: Example of the Chibougamau area, Abitibi Subprovince, Québec: Ore Geology Reviews, v. 144, 103127.

McDivitt, J.A., Lafrance, B., Kontak, D.J., and Robichaud, L., 2017, The Structural Evolution of the Missanabie-Renabie Gold District: Pre-orogenic Veins in and Orogenic Gold Setting and Their Influence on the Formation of Hybrid Deposits: Economic Geology, v. 112, p. 1959-1975.

McDivitt, J.A., Kontak, D.J., Lafrance, B., and Robichaud, L., 2018, Contrasting Fluid Chemistries, Alteration Characteristics, and Metamorphic Timing Relationships Recorded in Hybridized Orebodies of the Missanabie-Renabie Gold District, Archean Wawa Subprovince, Ontario, Canada: Economic Geology, v. 113(2), p. 397-420.

McDivitt, J.A., Kontak, D.J., Lafrance, B., Petrus, J.A., and Fayek, M., 2020, A trace metal, stable isotope (H, O, S), and geochronological (U-Pb titanite) characterization of hybridized fold orebodies in the Missanabie-Renabie district, Wawa subprovince (Canada): Mineralium Deposita, doi.10.1007/s00126-020-00983-9

Morey, A.A., Tomkins, A.G., Bierlein, F.P., Weinberg, R.F., and Davidson, G.J., 2008, Bimodal Distribution of Gold in Pyrite and Arsenopyrite: Examples from the Archean Boorara and Bardoc Shear Systems, Yilgarn Craton, Western Australia: Economic Geology, v. 103, p. 599-614.

Oberthür, T., and Weiser, T.W., 2008, Gold-bismuth-telluride-sulphide assemblages at the Viceroy Mine, Harare-Bindura-Shamva greenstone belt, Zimbabwe: Mineralogical Magazine, v. 72(4), p. 953-970.

Reich, M., Kesler, S.E., Utsunomiya, S., Palenik, C.S., Chryssoulis, S.L.,and Ewing, R.C., 2005, Solubility of gold in arsenian pyrite: Geochimica et Cosmochimica Acta, v. 69(11), p. 2781-2796.

Robert, F., 2001, Syenite-associated disseminated gold deposits in the Abitibi greenstone belt, Canada: Mineralium Deposita, v. 36, p. 503-516.

Samson, I.M., Bas, B., and Holm, P.E., 1997, Hydrothermal Evolution of Auriferous Shear Zones, Wawa, Ontario: Economic Geology, v. 92, p. 325-342.

Sibson, R.H., Robert, F., and Poulsen, K.H., 1988, High-angle reverse faults, fluid-pressure cycling, and mesothermal gold-quartz deposits: Geology, v. 16, p. 551-555.

Tooth, B., Brugger, J., Ciobanu, C.L., and Liu, W., 2008, Modeling of gold scavenging by bismuth melts coexisting with hydrothermal fluids: Geology, v. 36(10), p. 815-818.

Tooth, B., Ciobanu, C.L., Green, L., O'Neill, B., and Brugger, J., 2011, Bi-melt formation and gold scavenging from hydrothermal fluids: An experimental study: Geochimica et Cosmochimica Acta, v. 75, p. 5423-5443.

Voudouris, P.C., Spry, P.G., Mavrogonatos, C., Sakellaris, G.-A., Bristol, S.K., Melfos, V., and Fornadel, A.P., 2013, Bismuthinite derivatives, lillianite homologues, and bismuth sulfotellurides as indicators of gold mineralization in the Stanos shear-zone related deposit, Chalkidiki, Northern Greece: Canadian Mineralogist, v. 51, p. 119-142.

Williams-Jones, A.E., Bowell, R.J., and Migdisov, A.A., 2009, Gold in Solution: Elements, v. 5, p. 281-287.

Zhou, H., Sun, X., Fu, Y., Lin, H., and Jiang, L., 2016, Mineralogy and mineral chemistry of Bi-minerals: Constraints on ore genesis of the Beiya giant porphyry-skarn gold deposit, southwestern China: Ore Geology Reviews, v. 79, p. 408-424.

Zhou, H., Sun, X., Wu, Z., Yang, T., Li, D., Ren, Y., Liu, Q., Zhu, K., and Yu, H., 2018, Mineralogy of Bi-sulfosalts and tellurides from the Yaoan gold deposit, southwest China: Metallogenic implications: Ore Geology Reviews, v. 98, p. 126-140.

CHAPTER TWO – GEOLOGY AND METALLOGENY OF THE WAWA GOLD CORRIDOR: IMPLICATIONS FOR GOLD-FORMING PROCESSES IN OROGENIC SYSTEMS AND FOR REGIONAL AU MINERALIZATION IN THE MICHIPICOTEN GREENSTONE BELT, ONTARIO, CANADA

2.1 – Introduction

Precambrian greenstone belt-hosted gold deposits are rarely one-off occurrences; rather, they form contemporaneously with numerous other deposits along major crustal structures (e.g., Groves et al. 1987, Eisenlohr et al. 1989, Beirlein et al. 2006) and collectively define extensive gold provinces. Well-documented examples of such provinces include the Archean Abitibi greenstone belt (AGB) in the Superior province of northern Ontario and Quebec, Canada (e.g., Robert & Kelly 1987, Robert 2001, Bateman et al. 2008), the Paleoproterozoic Ashanti greenstone belt in the Birimian Craton, West Africa (e.g., Mumin et al. 1994, Oberthür et al. 1996, Béziat et al. 2008, Perrouty et al. 2014), and the Archean Goldfields province in the Yilgarn Craton, western Australia (e.g., Witt 1991, Morey et al. 2008, Hodkiewicz et al. 2009, Sung et al. 2009). The development of regional models for gold mineralization provides the basis for more efficient exploration tactics and furthers the understanding of the macro-scale processes responsible for the formation of major gold deposits. Although it is host to several historic and active mines and exploration projects and is considered to be an extension of the world-class AGB (e.g., Polat 2009), the gold deposits of the Michipicoten greenstone belt (MGB; Fig. 2.1a) have not been favoured with extensive research focus. Previous investigations include those of Samson et al. (1997) on the Wawa Gold Corridor (WGC), McDivitt et al. (2017, 2018) on the Missanabie-Renabie camp, Haroldson (2014) on the Magino deposit, and Ciufo (2019) and Jellicoe (2019) on the Island Gold deposit. McDivitt et al. (2017, 2018) were the first to propose a unifying model for gold mineralization in the MGB, in which they highlighted the importance of pre-orogenic introduction

of gold by magmatic-hydrothermal fluids. The WGC, an Archean lode gold district at the western extent of the MGB (Fig. 2.1a), is the subject of the present study. It comprises a series of gold-bearing shear zones and has been the focus of exploration and production for nearly a century (120,000 oz of Au was produced intermittently from several deposits between 1900 and 1989**;** Fig. 2.1b). The deposit currently hosts an indicated + inferred resource of over 700,000 oz of Au (https://redpineexp.com/projects/wawa-gold-project/).

Although the WGC has been studied previously (i.e., Samson et al. 1997), significant advances in the understanding of gold deposits have since been made, in particular the coprecipitation of invisible Au with Fe-As sulfides (e.g., pyrite and arsenopyrite; Large et al. 2009, Cook et al. 2013, Deditius et al. 2014, Zhang et al. 2014, Fougerouse et al. 2016, Gourcerol et al. 2018). This work has shown that pyrite and arsenopyrite are capable of incorporating a variety of trace metals and metalloids, either as lattice-bound substitutions (e.g., Ni, Co, Se, As, Au; Deditius et al. 2008, Large et al. 2014) or as micro- or nano-inclusions (e.g., Pb, Bi, Sb, Te, Ag, Au; Deditius et al. 2011, Large et al. 2014), and so provide an effective proxy for the chemistry of mineralizing fluids. Although such studies have provided insight into what governs the incorporation of gold into sulfide minerals and have highlighted the importance of this in removing Au from the fluid phase, large quantities of visible gold are also commonly present in these deposits (cf. Hastie et al. 2020, Petrella et al. 2020). Understanding the processes that may account for the formation of abundant native gold is crucial, given that restricted intervals of high-grade gold mineralization can significantly impact the economic feasibility of a gold deposit, and a commonly proposed hypothesis is that this gold originated as Au dissolved in sulfide minerals (e.g., Lawley et al. 2017, Hastie et al. 2020).

The present study integrates field studies with mineral-chemical and isotopic analysis to investigate Au enrichment in the WGC. A particular focus is to evaluate the capacity of the sulfide minerals to have been the source for the native gold that is present in the deposit. In so doing, this study also contributes to the evolving model for regional gold mineralization in the MGB and other similar settings globally.

2.2 – Geology of the Michipicoten greenstone belt and Jubilee stock

The MGB comprises bimodal mafic and felsic volcanic rocks belonging to three cycles at ca. 2890 Ma, 2750 Ma, and 2700 Ma, with the volcanic strata separated by clastic and chemical sedimentary rocks (Turek et al. 1982) and coeval felsic to intermediate plutonism associated with each of the volcanic cycles (Turek et al. 1992). The gold-bearing shear zones that constitute the WGC are hosted in one such intrusive, the Jubilee Stock, which crystallized during the second cycle of volcanic activity at 2745 ± 10 Ma (Sullivan et al. 1985).

The rocks that define the Jubilee Stock range in composition from tonalite to diorite and contain abundant xenoliths of biotite- or feldspar-phyric andesite or tuffaceous volcaniclastic rocks (Fig. 2.2a). A population of chloritized gabbroic dykes (Fig. 2.2b) crosscut the stock; these have a roughly SSE-NNW strike and dip moderately to the southwest. Due to the rare occurrence of gabbroic xenoliths within the intermediate rocks of the Jubilee stock, these dikes are interpreted to have been emplaced during the late stages of stock crystallization.

The area was also intruded by later mafic dykes, including those that may belong to the Matachewan dike swarm (e.g., Halls & Palmer 1990, Samson et al. 1997) and by both Archean and Proterozoic lamprophyres. Archean lamprophyres are pervasively carbonate-altered and sometimes foliated, which suggests a syn-deformation timing; these dikes may be related to the

emplacement of diamondiferous lamprophyres in the Wawa region dated at ca. 2700 Ma (Lefebvre et al. 2005, Stachel et al. 2006). Proterozoic lamprophyres, which are undeformed and associated with a diagnostic riebeckite-carbonate alteration assemblage, are related to the formation of the Firesand River Carbonatite Complex (Sage 1988), dated at ca. 1000 Ma (Symons 1989).

The Jubilee Stock hosts several shear zones of variable width and orientation that are characterized by the alteration of primary igneous minerals to assemblages that are dominated by quartz, carbonates, phyllosilicates, and sulfides. Within shear zones, these assemblages are associated with the development of penetrative planar and linear deformation fabrics, but alteration assemblages also exist in undeformed portions of the stock. The syn-Jubilee gabbro dikes are pervasively chloritized (Fig. 2.2b), which probably related to both pre-orogenic hydrothermal activity and to regional greenschist-facies metamorphism (cf. Studemeister 1985). Undeformed rocks in the Jubilee Stock also contain a pervasive albite-quartz-biotite-chlorite alteration assemblage, as well as biotite ± quartz ± chlorite veinlets (Fig. 2.2c). These alteration assemblages in undeformed rocks also contain arsenopyrite and trace amounts of pyrite, pyrrhotite, and molybdenite in intervals adjacent to major gold-bearing shear zones in the WGC (e.g., Fig. 2.2d).

2.3 – Methods

2.3.1 – Field work and sampling

Primary observations of the geology in the study area are based on detailed observations of outcrops and mechanically stripped areas and of representative diamond drill core. In addition, 120 samples of representative lithologies, alteration assemblages, structural fabrics, and gold-bearing intervals were taken from oriented drill core for preparation of polished thin sections.

2.3.2 – Petrography

Transmitted and reflected light optical microscopy was performed using an Olympus BX-51 microscope. Images were captured using the Infinity Analyze software. Mineral textures and morphologies were also investigated with scanning-electron microscopy back-scattered electron imaging (SEM-BSE), as noted below.

2.3.3 – Mineral chemistry

2.3.3.1 – Energy-dispersive X-ray spectroscopy

Qualitative major-element mineral chemistry and mineral identification was determined via scanning electron microscope energy-dispersive X-ray spectroscopy (SEM-EDS) using an FEI Quanta 200 FEG environmental SEM equipped with an EDAX EDS detector at the University of Windsor, Ontario. The operating voltage was 20.0 kV, the beam current was 222 µA, the spot size was 3.9 µm, and the acquisition time was 30 seconds.

2.3.3.2 – LA-ICP-MS transect analysis

Laser-ablation inductively-coupled plasma mass spectrometry (LA-ICP-MS) analysis, in the form of line transects, was conducted on grains of pyrite and arsenopyrite using a 193 nm nanosecond Ar-F laser coupled to an Agilent 7900 quadrupole mass spectrometer. The experiments were performed at the Element and Heavy Isotope Analytical Laboratory at the University of Windsor. The elements analyzed for were selected based on potential occurrence in pyrite or arsenopyrite (Co, Ni, Cu, Zn, As, Se, Mo, Ag, Cd, In, Sn, Sb, Te, W, Re, Os Au, Pb, and Bi) or their usefulness in discriminating between the target sulfide phase and potential inclusions of gangue minerals (Al, Si, S, Ca, Ti, and Fe). The isotopes detected (^{27}Al ^{29}Si, ^{34}S, ^{44}Ca, ^{48}Ti, ^{57}Fe, ^{59}Co, ^{60}Ni, ^{63}Cu, ^{66}Zn, ^{75}As, ^{78}Se, ^{82}Se, ^{95}Mo, ^{98}Mo, ^{107}Ag, ^{109}Ag, ^{114}Cd, ^{115}In, ^{120}Sn, ^{121}Sb,

^{130}Te, ^{184}W, ^{185}Re, ^{192}Os, ^{197}Au, ^{208}Pb, and ^{209}Bi) were chosen to assess potential isobaric interference. Analyses were conducted using a laser energy of 4.1 µJ, repetition rate of 20 Hz, a beam size of 25 µm, and a traverse rate of 5 µm/s. Thirty seconds of gas background was recorded at the beginning of each analysis, followed by up to 60 seconds of ablation. The reference material FeS-UQAC-1 was analyzed and used as the external standard during data processing and NIST-610 was also analyzed to ensure measurement accuracy. External standards were analyzed at the beginning of each experiment and in-between each set of 20 analyses of samples. Stoichiometric Fe was used as the internal standard for pyrite and arsenopyrite. Raw transect data were processed using the Iolite software (v. 3.0) and visualized afterwards using the ioGAS software (v. 7.0).

2.3.3.3 – LA-ICP-MS mapping

The analytical conditions for the two-dimensional mapping of pyrite grains are identical to those described for the transect analyses (above), except for the use of a 10 µm beam width for better resolution. Maps were collected using a series of stacked traverses and each map was bracketed by the analysis of two reference materials (FeS-UQAC-1 and NIST-610). Timeseries data (i.e., an individual datum value for each integration period during laser pulsing, as opposed to integration over multiple periods) were generated using the "natural" setting in Iolite and element maps were created using the Surfer software (v. 11.0).

2.3.4 – Stable isotopes

In situ stable S isotopes (^{32}S, ^{33}S, ^{34}S) of pyrite were analyzed at the Canadian Centre for Isotopic Microanalysis (CCIM) at the University of Alberta using an IMS-1280 multi-collector ion microprobe. Prior to analysis, regions of interest (2 – 4 mm across) were cored from polished thin sections and mounted along with reference materials (CCIM S0302A) in an epoxy mount.

High-contrast SEM-BSE imaging was used to characterize internal structures within pyrite grains and facilitate selection of points for analysis. A $^{133}Cs^{+}$ ion beam was operated under an acceleration voltage of 20 keV with a beam size of 15 µm and a beam current of 1.5 nA. Reference standards were analyzed after every four sample analyses; instrumental mass fractionation was assessed using these repeated measurements of standard materials and confirmed to be negligible. The 2σ uncertainties at the 95% confidence interval are ±0.13‰ for $\delta^{34}S$ and ±0.28‰ for $\Delta^{33}S$; both $\delta^{34}S$ and $\Delta^{33}S$ values reported herein are with respect to the Vienna-Canyon Diablo Troilite (V-CDT).

2.4– Results

2.4.1 – Structural evolution of the WGC and description of Au-bearing rocks

It must be noted that the structural nomenclature that follows does not correspond directly to a system where D_1 formed a regional, first-order structure (e.g., Eisenlohr et al. 1989). Instead, it represents the sequence of deformational events that are recorded at the scale of the Jubilee stock and WGC.

The D_1 event comprises the development of locally penetrative, NNW-striking (~320° - 350°) S_1 fabrics that dip steeply (50 – 60°) to the ENE and tight, isoclinal, F_1 folds within shear zones. S_1 is defined by the orientation of muscovite, biotite, and chlorite, which are the major phyllosilicate minerals that make up the schists in the shear zones of the WGC. L_1 describes a stretching lineation, often represented by elongated pyrrhotite or pyrite grains. The widths of D_1 shear zones ranges from approximately one to ten metres. Quartz veins are a volumetrically minor component of D_1 schists, with individual veins rarely exceeding a few centimetres in width. Sulfide mineralization in D_1 schists is dominated by arsenopyrite, with some pyrite and pyrrhotite, and

gold grades correlate positively with the abundance of arsenopyrite. Texturally, most arsenopyrite is fine grained and occurs in laminated bands parallel to S_1 (Fig. 2.3a).

The most abundant deformation features observed in the WGC are related to the D_2 event, which resulted in a penetrative NNE-striking S_2 (~020° - 060°) that dips moderately (35 – 50°) to the southeast. L_2 is a shallowly southward-plunging stretching lineation defined by stretched sulfide grains or elongated rods of quartz and carbonate (Fig. 2.3b); this structural feature is the major control on the geometry of lenses of gold and sulfide mineralization within D_2 shear zones. The overprinting of S_2 on S_1 produced F_2 microfolds (Fig. 2.3c) whose fold axes are co-linear with L_2. Although S_2 may be present in weakly deformed tonalite throughout the study area, the localization of D_2 shear zones and related schists was governed by the rheological contrasts between various phases of the Jubilee stock and, as a consequence, individual shear zones are anastomosing and variably discontinuous along strike (Fig. 2.3d). The D_2 shear zones may be up to approximately one hundred metres wide. The mineralogy of D_2 schists differs from those formed during D_1 deformation by the relative predominance of pyrite over arsenopyrite and of chlorite and muscovite over biotite. From a purely descriptive standpoint, quartz + carbonate veining in these rocks may be more aptly referred to as "silica flooding", whereby the volume of hydrothermal quartz and carbonate is so great that these minerals may locally appear to constitute the matrix of the rock instead of discrete shear or tension veins in a phyllosilicate-rich wall-rock. Where veins are discernible, they are often present as stretched rods in L_2. Most pyrite grains in these schists are equant and occur in clusters and seams, typically localized around bands of phyllosilicate minerals in a quartz-carbonate matrix. Visible gold is often observed in D_2 schists, particularly when silica flooding is pervasive.

The D_3 deformation event reflects a decrease in the intensity of ductile deformation and the transition to a brittle regime. This event formed a locally penetrative S_3 foliation (~310° - 340°) that dips moderately (40 – 50°) to the northeast and is defined by the alignment of chlorite and muscovite in sheared gabbroic dyke rocks and intermediate rocks of the Jubilee Stock. D_3 shear zones formed along the contacts between gabbroic dykes and tonalite, with the former accommodating the majority of the strain (Fig. 2.3e); the width of these zones rarely exceeds a few metres. The occurrence of quartz + tourmaline + carbonate veins with a shear-parallel orientation is a salient feature of the D_3 event. These veins crosscut D_2 shear zones, where they are discordant with S_2 and may incorporate fragments of D_2 schist (Fig. 2.3f). They are characterized by seams of tourmaline or chlorite-altered wall-rock and the dominant sulfide minerals are pyrrhotite, pyrite, and chalcopyrite. Small (i.e., millimetre-scale) carbonate veinlets crosscut the matrix of the shear veins. Visible gold is comparatively abundant in the shear veins as opposed to the schists and exhibits a strong nugget effect.

2.4.2 – Petrography and mineral paragenesis

Virtually all the sulfide- and gold-bearing rocks are restricted to the shear zones. However, a variety of coarse-grained, sub-euhedral arsenopyrite is rarely present as disseminations in undeformed intrusive phases of the Jubilee Stock (Fig. 2.4a). Although such rocks may contain anomalous concentrations of Au (<0.01 – 1 ppm), they do not represent a significant source of potentially-economic Au mineralization (i.e., >2-3 ppm) and so were not the focus of extensive microanalysis.

Most of the sulfide and gold mineralization in D_1 structures occurs as fine-grained disseminations hosted by schists. The dominant sulfide minerals in these rocks are arsenopyrite, pyrite, and pyrrhotite. Bands of fine-grained, disseminated arsenopyrite are contained in S_1 and

are co-spatial with layers of muscovite and sometimes biotite that define the foliation (Fig 4b) and that are spaced by lenses of quartz and carbonate minerals (calcite or Fe+Mg-bearing calcite). Fine-grained arsenopyrite in D_1 schists sometimes occurs in clusters, rather than bands (Fig. 2.4c). Based on the rhombic shape of these aggregates, this texture that may represent the replacement of previous coarse-grained arsenopyrite. Biotite in these rocks is commonly mantled by chlorite (Fig. 2.4d). Arsenopyrite grains are typically euhedral and free of inclusions and display complex internal textures under high-contrast BSE imaging (Fig. 2.4e). Two types of pyrite are present in the D_1 schists. The first type (Py_{1A}) occurs along with arsenopyrite as inclusions within stretched grains of pyrrhotite (Fig. 2.4f). The second type (Py_{1B}) is anhedral, elongated in line with S_1, and commonly mantles and postdates arsenopyrite (Fig. 2.4c). Of the two varieties of pyrite in D_1 schists, Py_{1B} is much more abundant.

The architecture of D_2 schists is similar to that of D_1 schists; the seams of muscovite and chlorite that define S_2 show pinch-and-swell morphology and are separated in two dimensions by rods of quartz and calcite that define L_2. Although the gangue mineralogy is still dominated by quartz, carbonates, and muscovite, chlorite is prevalent over biotite; where biotite is present it is variably replaced by chlorite (Fig. 2.5a). Transition from the D_1 stress regime to the D_2 stress regime was accompanied by a change in sulfide mineralogy from arsenopyrite- to pyrite-dominant. Accessory sulfide minerals include chalcopyrite and galena. Pyrite in D_2 schists is texturally distinct from both Py_{1A} and Py_{1B} and comprises coarse (up to several millimetres across), subhedral to euhedral grains with inclusion-rich cores and inclusion-poor margins (Fig. 2.5b). The mineralogy of inclusions is variable and includes arsenopyrite, pyrrhotite, chalcopyrite, gold, galena, bismuthinite, quartz, muscovite, chlorite, calcite, rutile, and apatite (Fig 2.5c). As with arsenopyrite, high-contrast BSE imaging reveals internal heterogeneities; the inclusion-rich cores

are characterized by oscillatory zonation, whereas the inclusion-poor rims are chemically homogenous and appear to have replaced and overgrown the zoned cores (Fig. 2.5d). Despite the clear temporal distinction between the core and rim material, entire grains of pyrite are commonly brecciated, with fractures that cut both core and rim and are infilled with quartz and carbonate minerals. Additionally, the margins of the inclusion-poor rims are corroded and bordered by D_2 phyllosilicates and quartz. These types of pyrite are referred to as Py_{2A} (cores) and Py_{2B} (rims).

The shear veins that host D_3 mineralization (sulfides and gold) consist of a granoblastic quartz matrix with bands of randomly oriented euhedral tourmaline and coarse patches of anhedral to subhedral calcite and ferroan dolomite. Sulfide minerals are volumetrically minor and formed proximally to laminations of tourmaline or wall-rock fragments. Anhedral pyrrhotite is the most abundant sulfide phase and sometimes occurs around rare grains of euhedral pyrite, which will be referred to as Py_{3A} (Fig. 2.6a); conversely, pyrrhotite is commonly mantled by anhedral pyrite, which will be referred to as Py_{3B} (Fig. 2.6b). This pyrite is itself rimmed, veined, and replaced by a siderite ± riebeckite assemblage and replaced by chalcopyrite (Fig. 2.6c). Chalcopyrite also occurs with siderite in veinlets that crosscut the shear veins. A population of fine-grained, euhedral pyrite grains is present in the coronae of Py_{3B}; unlike Py_{3B}, these grains share planar, regular boundaries with siderite (Fig. 2.6d) and, where present, with riebeckite (Fig. 2.6e). Given the textural evidence that the assemblage comprising siderite, riebeckite, chalcopyrite, and the euhedral pyrite crosscuts the D_3 veins, this generation of pyrite is referred to as Py_4. Blebs of Au-Bi-Te minerals (e.g., gold, bismuth, maldonite, tsumoite, bismuthinite) are found with the siderite ± chalcopyrite ± riebeckite ± Py_4 assemblage that enveloped and replaced pyrrhotite and Py_3, or along fractures in vein quartz; these minerals typically have mutual curvilinear boundaries (Fig. 2.7a, b) or globular morphologies (Fig. 2.7c).

Although not always visible at the hand-sample scale, native gold is common in mineralized samples from the WGC and occurs as: (1) inclusions or along fractures in arsenopyrite and Py_2 (Fig. 2.8a, b); (2) isolated grains in the quartz + carbonate + phyllosilicate matrices of D_1 and D_2 schists (Fig. 2.8c, d); and (3) grains that form part of chalcopyrite + Au-Bi-Te-bearing mineral assemblages in carbonate veinlets that post-date D_3 shear veins (Fig. 2.8e, f). It is important to note that with petrography alone, it is unclear if these textural varieties of gold represent discrete additions of gold to the system; still, based on the presented petrographic observations, a mineral paragenesis for the deposit may be established and the timing of potential gold events can be identified (Fig. 2.9).

2.4.3 – Sulfide mineral chemistry

The minor- and trace-element concentrations in arsenopyrite, Py_{1A}, Py_{1B}, Py_{2A}, Py_{2B}, Py_{3A}, Py_{3B} and Py_4 were determined using LA-ICP-MS. Box-whisker plots with the sulfide generations presented in order of paragenetic sequence are used to illustrate relative temporal changes in sulfide chemistry (Fig. 2.10). Key features of the chemistry of sulfides in the WGC are: (1) arsenopyrite, and to a lesser extent Py_{2A}, are enriched in Au compared to the other pyrite types; (2) pyrite in D_1-D_2 schists (i.e., Py_{1A-B} and Py_{2A-B}) are enriched in As compared to pyrite in D_3 quartz-tourmaline shear veins (i.e., Py_{3A}, Py_{3B}, and Py_4); and (3) arsenopyrite and Py_{2A} are somewhat enriched in Bi and clearly enriched in Te compared to Py_{3B} (Fig. 2.10).

The spatial distribution of Au within single grains of arsenopyrite that appear to record multiple generations based on high-contrast BSE imaging can be visualized with the profile of the LA transect (Fig. 2.11). Here, the BSE-dark material is notably poorer in Au than the BSE-bright material.

Compositional heterogeneities within grains belonging to the major Au-bearing generations of pyrite were investigated using LA element mapping. Maps for Py_{1B} (Fig. 2.12) reveal a core that is relatively depleted in trace metals and is overgrown by an anhedral rim that is relatively enriched in trace metals (e.g., Ni, Co, Ag, Pb, Bi, Au). Adjacent to the grain of Py_{1B} in Figure 2.12 are two smaller grains of arsenopyrite that are characterized by higher concentrations of As, Co, and Au as compared to Py_{1B}.

Element maps of Py_{2A-B} (Fig. 2.13) illustrate the compositional differences between the inclusion-rich cores (Py_{2A}) and inclusion-poor rims (Py_{2B}) that distinguish this generation of pyrite: Py_{2A} is enriched in As, Au, Cu, Ag, Sb, Pb, and Bi, whereas Py_{2B} is enriched in Ni and Co. As-poor regions within the grain core likely represent penetrative replacement of Py_{2A} by Py_{2B}, whereas the As-poor regions that define the grain rim represent overgrowth of Py_{2B} on Py_{2A}. Within the core, the spatial distributions of Au and As are antithetical to those of Cu and the low melting point chalcophile elements (LMCEs; e.g., Bi, Te, Sb, Ag, Pb); the latter reflect inclusions of minerals like chalcopyrite, galena, and bismuthinite (all documented petrographically as inclusions in Py_{2A}). The occurrence of several spots of elevated As along the borders of Py_{2A} and Py_{2B} within the core are probably inclusions of arsenopyrite. When considering the compositional characteristics of the mapped pyrite grains, Au appears to correlate either with As (e.g., Py_2) or with LMCEs (e.g., Py_1).

The element associations observed within maps of single grains of pyrite (Fig. 2.12, 2.13) can be tested using the LA transect data, which, statistically, is more robust given the greater number of data. The concentrations of Au in pyrite were plotted against the sum of the concentrations of Ag, Te, Pb, and Bi (Fig. 2.14a) and against As (Fig. 2.14b). It is apparent that enrichments either in As or in LMCEs may correspond to enrichments in Au. There is a positive

correlation between Au and LMCEs, and the grains of pyrite that have the highest As concentrations (i.e., Py_{2A}) also have the highest Au concentrations.

2.4.4 – Stable sulfur isotopes

$\Delta^{33}S$ values for Py_{1B}, Py_{2A}, Py_{2B}, Py_{3B}, and Py_4 are clustered around 0.0 ‰ and $\delta^{34}S$ for these same sulfides are constrained within a low positive range (0.1 – 4.1 ‰; Fig. 2.15). In both cases, there is significant overlap with the range of S isotope values documented for the Island Gold deposit (1.2 – 2.9 ‰; Ciufo 2019) (Fig. 2.15), whereas $\delta^{34}S$ values for pyrite from Missanabie-Renabie are markedly different (-3.1 to -5.8 ‰; McDivitt et al. 2020) (Fig. 2.15). With the exception of Py_{2A} and Py_{2B}, no significant intra-grain variation was observed in $\delta^{34}S$ values. Whereas all Py_{1B}, Py_{3B}, and Py_4 analyses have values between 0.1 and 2.2 ‰, Py_{2A} and Py_{2B} are contained within the range of 2.0 – 4.1 ‰.

5 – Discussion

2.5.1 – Interpreting the mineral paragenesis for the WGC

Although numerous temporal and textural varieties of sulfide minerals in the WGC have been described above, there are several key sulfide assemblages that are more abundant than others: (1) arsenopyrite + Py_{1B}; (2) Py_{2A} + Py_{2B}; and (3) Py_{3B} + Py_4. Of these, arsenopyrite and Py_{2A} are enriched in Au compared to other sulfides (Fig. 2.10), and native gold is found in spatial proximity to all three of these assemblages; a more detailed assessment of the development of these assemblages is therefore an important precursor to understanding the genesis of gold mineralization in the WGC.

Single grains of arsenopyrite in the WGC are composed of multiple generations that may be distinguished under high-contrast BSE imaging. In particular, dark-BSE arsenopyrite is

observed to replace earlier, light-BSE arsenopyrite and porosity is sometimes present in areas of the grain in which this replacement occurred (Fig. 2.4e). The occurrence of intragrain replacement by multiple generations of the same mineral, along with the development of porosity, is indicative of coupled dissolution-reprecipitation reactions (CDR; Putnis 2009). When combining these paragenetic interpretations with LA transect analysis, it becomes apparent that the earlier arsenopyrite is Au-rich, and the later arsenopyrite is Au-poor (Fig. 2.11). Arsenopyrite was also out of equilibrium with the fluids that precipitated Py_{1B}, with the latter mineral typically mantling and replacing the former (Fig. 2.4c). Figure 2.12 shows element maps for a grain of Py_{1B}, adjacent to which are two grains of arsenopyrite that are characterized by higher concentrations of Au, As, and Co. Within the grain of Py_{1B}, there is a euhedral zone of strong Co enrichment and moderate As enrichment. Taking these chemical observations in combination with the textual evidence for the replacement and overprinting of arsenopyrite by Py_{1B}, it is possible that the discrete zone of Co and As enrichment within Py_{1B} was previously a grain of arsenopyrite. This region is not enriched in Au (as are the grains of arsenopyrite adjacent to Py_{1B}) and could therefore indicate the replacement of Au-rich arsenopyrite by Au-poor pyrite.

The arsenopyrite + Py_{1B} assemblage is also an important marker for the structural evolution of the WGC. Although these minerals are most common in D_1 schists, they may also occur in restricted domains in D_2 shear zones, the geometries of which follow L_2. This observation, in conjunction with that of the development of F_2 microfolds via the modification of S_1 (Fig. 2.3c), is evidence that D_2 shear zones developed in part through structural and hydrothermal overprinting of D_1 schists.

Py_{2A-B} is the most common sulfide mineral in D_2 schists. Individual grains of pyrite comprising these two generations are defined by a Py_{2A} core that is rich in inclusions and trace

metals and a Py_{2B} rim that is poor in inclusions and trace metals (Fig. 2.13). Although most of the Py_{2B} generation occurs in the rims of grains, it is also seen to infiltrate and replace Py_{2A} in the cores; it is also these zones of replacement that mineral inclusions (including gold) and pores developed. Thus, the formation of Py_{2B} after Py_{2A} occurred by both replacement and overgrowth, although the relative volume of Py_{2B} formed through each process appears to vary from grain to grain. The development of porosity and precipitation of mineral inclusions in zones of replacement in Py_{2A-B} is consistent with CDR, and it is likely that the trace metals present in Py_{2A} were mobilized to form these mineral inclusions during such processes (cf. Velásquez et al. 2014, Lawley et al. 2017, Hastie et al. 2020).

Although Py_{3B} shows neither internal zonation nor porosity, it is regularly rimmed by an alteration assemblage of siderite + Py_4, in which gold and Bi-Te minerals may be found. Whereas siderite veinlets are observed throughout the D_3 shear veins, Py_4, gold, and Bi-Te minerals are found only where this siderite replaced blebs of Py_{3B}. Thus, the dissolution of Py_{3B} and associated crystallization of siderite + Py_4 may have been an important process in the development of gold-bearing assemblages in D_3 shear veins.

2.5.2 – Discriminating between primary and secondary gold events and the formation of native gold

2.5.2.1 – Preamble

Whether they are derived from the metamorphic devolatilization of crustal rocks (e.g., Murphy and Roberts 1997, Buhn et al. 2012, Mishra et al. 2018) or from felsic magmas (e.g., Lawrence et al. 2013, McDivitt et al. 2018, Kerr et al. 2018), the hydrothermal fluids that mineralize orogenic systems are likely to be undersaturated with respect to gold at their source

(e.g., Gammons & Williams-Jones 1997, Williams-Jones et al. 2009). Such fluids are therefore incapable of directly precipitating gold and so physiochemical variations at the site of deposition are necessary to separate Au from the hydrothermal fluid (e.g., decreasing fO_2, fluid boiling; Williams-Jones et al. 2009); a commonly documented process involves the incorporation of Au into actively-precipitating Fe-As sulfide minerals, such as (arsenian) pyrite (e.g., Hazarika et al. 2013) and arsenopyrite (e.g., Gourcerol et al. 2020), during the destabilization of the bisulfide complexes that contain Au in solution (Williams-Jones et al. 2009). Both of these minerals are capable of dissolving up to thousands of ppm Au (Cabri et al. 1989, Reich et al. 2005; Hastie et al., 2020), so their crystallization in the presence of Au-bearing fluids (and contemporaneous destabilization of the Au-bisulfide complex(es) is an efficient method of trapping and concentrating Au. In this form (i.e., dissolved in sulfide minerals), Au is termed "invisible" and, given its formation directly from the Au-mineralizing fluid, is described here as primary. Several processes have been proposed to account for the generation of remobilized (i.e., secondary) gold from this invisible state and an evaluation of these is presently warranted given the abundance of both invisible and visible gold in the WGC.

2.5.2.2 – Mass-balance constraints on the redistribution of gold

In the studied samples, gold occurs as: (1) Au dissolved in arsenopyrite and pyrite; (2) gold as inclusions in, along fractures in, or on the margins of D_1 arsenopyrite and D_2 Py_2; and (3) gold with chalcopyrite and Bi-Te phases hosted by carbonate-rich veinlets in brittle fractures that cross-cut D_3 shear veins and overprint Py_{3B}. The liberation of invisible Au during dissolution of a host sulfide mineral (i.e., pyrite or arsenopyrite) has been proposed to explain the occurrence of abundant gold in several deposits (e.g., Morey et al. 2008, Lawley et al. 2017, Hastie et al. 2020). When considering this model for the WGC, it is relevant to note that the most abundant Au-bearing

sulfides in the WGC (these being arsenopyrite, Py_{2A-B}, and Py_{3B}, in D_1, D_2, and D_3 schists, respectively) underwent post-crystallization modification. Mass-balance calculations were employed to assess the potential of these Au-bearing sulfides to have been the source for the native gold in the deposit. To calculate the amount of Au contained in such sulfides, the average concentration of Au from multiple LA-ICP-MS analyses of sulfides belonging to a single generation (e.g., Py_{2A}) in a single sample was multiplied by the modal abundance of that sulfide over a given assay interval (approximately one metre). When plotted against the whole-rock assay value for Au, these values provide a reasonable visualization of the proportion of invisible to visible gold in a given sample interval (Fig. 2.16). Here, the contours represent the percentage of Au that is present in the sulfides compared to the total measured concentration of Au. Several pertinent observations can be made: (1) the Au grade in samples in which the dominant sulfide is arsenopyrite is represented almost entirely by invisible Au in arsenopyrite, although for three samples the arsenopyrite only accounts for ~1% of the measured gold grade; (2) samples containing mainly Py_{2A} have 1 – 10 % of the gold grade represented by invisible Au in sulfides; and (3) with the exception of one low-grade outlier, all samples containing Py_{3B} have <0.5% of the Au grade represented by invisible Au in sulfides. The samples of arsenopyrite that plot close to the line y = x ("100 %") in Figure 2.16 likely represent the preservation of primary invisible Au mineralization; that is, most of the grade in the rock is accounted for by Au in arsenopyrite and so remobilization of invisible Au out of arsenopyrite was minimal in these samples. For the remaining samples that plot away from the line y = x, it is possible that some form of gold mobilization has occurred.

2.5.2.3 – Mobilization of gold in molten form

The association of Au with LMCEs and the presence of Au-LMCE mineral assemblages with textural relationships like curvilinear grain boundaries and trails of globular blebs (Fig. 2.7) have been used to invoke the transport of gold in polymetallic LMCE-rich melts (e.g., Ciobanu et al. 2006, Ciobanu et al. 2010, Cockerton & Tomkins 2012, Guimarães et al. 2019, Hastie et al. 2020). When documented in shear zone hosted gold systems, such assemblages are typically parageneticallly-late (e.g., Oberthür & Weiser 2008, Voudouris et al. 2013, Novoselov et al. 2015) and may form within or on the margins of pyrite or arsenopyrite (e.g., Kerr et al. 2018, Cave et al. 2019, Hastie et al. 2020), leading to the suggestion of Au mobilization in LMCE melts from original invisible Au (±Te-Bi-Cu-Pb). Given its textural and mineralogical characteristics, the visible gold in D_3 veins of the WGC is likely secondary and was mobilized from earlier Au-bearing sulfides and transported in polymetallic melts. The occasional presence of riebeckite in these assemblages suggests that the timing overlaps with emplacement of Proterozoic lamprophyres that crosscut the deposit area and that mobilization was thus mediated by hydrothermal fluids related to these dikes. It is important to note that the pyrite in closest proximity to the Au-LMCE mineral assemblages (i.e., Py_{3B}) is Au-poor (0.1 – 1 ppm) and was probably not an exclusive source of Au during this event. Given the ability of LMCE melts to travel significant distances (e.g., potentially up to several kilometres; Tomkins et al. 2004), it is reasonable to assume that elements forming the Au-LMCE assemblages were sourced from other orogenic sulfides more enriched in these elements (e.g., arsenopyrite, Py_{2A}).

2.5.2.4 – Importance of sulfide replacement and dissolution reactions

Mineral-chemical data indicate that moderate invisible Au enrichment within pyrite grains is sometimes associated with enrichments in LMCEs (even in the absence of As; Fig. 2.14); however, an association with LMCE minerals is noticeably lacking for the visible gold that occurs in D_1-D_2 schists, whose sulfide mineralogy is dominated by arsenopyrite or Py_2. Here, visible gold occurs on the margins of or within arsenopyrite and Py_{2A-B}, or amongst the gangue minerals that make up D_1 and D_2 schists (Fig. 2.8a-d). The remobilization of this gold via transport in a LMCE melt can therefore be discounted and other possibilities must be considered. During CDR reactions involving Au-bearing sulfides, Au may have precipitated along fissures in the original host sulfide or in pores that developed during replacement of the original host sulfide (cf. Morey et al. 2008, Cook et al. 2013, Hastie et al. 2020). Although the textural characteristics of Py_{2A-B} are consistent with CDR reactions and thus the liberation of gold into fractures and inclusions, mass-balance constraints must also be assessed. At most, the concentration of Au in Py_{2A} over a given core interval is 20 ppm and the modal abundance of Py_{2A-B} in a typical D_2 schist rarely exceeds 5 %. Assuming that all Py_{2A} was replaced by Py_{2B}, and assuming that Py_{2B} incorporated little Au (the average Au content in Py_{2B} is 0.15 ppm), a maximum of 1 ppm could have been released during replacement. However, this is an order of magnitude short of the observed whole-rock concentrations as a high-grade interval in a D_2 schist contains around 10 ppm whole-rock Au (of which the remaining 9 ppm, as outlined in this calculation, would be present as native gold). This disparity requires reconciliation, as Py_{2A-B} is the dominant sulfide in D_2 schists, which themselves host most of the gold in the WGC. Before discounting Py_{2A} as a major source of visible gold in the WGC, however, several potential complications to the mass-balance calculations must be considered: (1) gold was possibly remobilized on a scale of metres to tens of metres, such that the

single-assay system (i.e., <1 m) is inappropriate for mass-balance calculations; (2) the hydrothermal fluids driving CDR reactions in Py_{2A-B} were themselves Au-bearing and this Au was added to the system via precipitation on pre-existing gold grains in Py_{2A-B} (i.e., an open system); and (3) the amount of Py_{2A} dissolved exceeded the amount of Py_{2B} precipitated, such that the presently observed volume of pyrite does not represent the original volume. As mentioned previously, the mobilization of large quantities of gold over significant distances requires a fluid phase that can dissolve high concentrations of Au, such as LMCE melts (e.g., Tomkins et al. 2004, Hastie et al. 2020); typical aqueous-carbonic fluids do not meet this criterion, which is why, in the absence of LMCE melts, remobilized Au that is thought to have been derived from a sulfide would be expected to have precipitated proximally to the source sulfide grain. Given the absence of Au-LMCE assemblages, it is unlikely that remobilization occurred on a metre-scale and so the single-assay mass-balance approach is considered appropriate. It cannot be discounted that gold was added to the system by the hydrothermal fluids that mediated CDR reactions in Py_2. Mass-balance calculations have led to such conclusions for the Detour Lake deposit in Ontario, where it was proposed that the expulsion of gold from pyrite during recrystallization was inadequate to account for the total deposit endowment and that micro-structures within deformed pyrite crystals acted as precipitation traps for later gold-bearing metamorphic fluids (Dubosq et al. 2018). If significant addition of gold did occur during CDR, however, it should be evident on the grain-scale. Following the approach of Mumin et al. (1994) and Hastie et al. (2020), the mass-balance of single pyrite grains can be evaluated. Taking into account the density of pyrite (0.00502 g mm^{-3}) and gold (0.01932 g mm^{-3}), a 1 mm^3 grain of pyrite with 20 ppm Au (a reasonable value for a grain of Py_{2A}) could produce a cubic grain of gold approximately 17 μm across. This is compatible with the observed size of gold inclusions in Py_{2A}, the dimensions of which are usually in range of several

to a few tens of microns, and with the fact that typically no more than a few such inclusions of gold are observed within a single grain (Fig. 2.5c). So, it is likely that any gold added to the system during the precipitation of Py_{2B} was negligible. Finally, if the amount of pyrite that was dissolved was greater than that that reprecipitated, it is possible that the volume of pyrite observed in the samples is less than the volume of primary Au-bearing pyrite that existed initially. Indeed, individual grains of Py_2 consistently have subhedral, brecciated morphologies with irregular, corroded margins, pores, and variably developed rims of Py_{2B} (Fig. 2.5b); these textures are indicative of volume loss during CDR. Still, a metre interval with a grade of 10 ppm Au would require an initial modal abundance of 50 % Py_{2A} with a concentration of 20 ppm; this is unreasonable for the WGC, which is a low sulfide deposit that lacks any evidence for pre-existing zones of massive pyrite. Despite abundant textural and mineral-chemical evidence for the release of invisible gold during CDR reactions, as well as its volumetric predominance over arsenopyrite, pyrite could not have been the source for most of the visible gold in the deposit.

With reference again to Figure 2.16, which shows the significant contribution of invisible Au in arsenopyrite to whole-rock grade, the potential for arsenopyrite to have been the source for the native gold in D_2 shear zones cannot be ignored. Whereas this mineral only predominates in D_1 structures largely free of hydrothermal and structural D_2 overprint, it sometimes occurs as a minor component of the ore assemblage in D_2 schists. Where present, it shows textural relationships to pyrite suggesting that it was replaced by the latter (Fig. 2.4c). Laser ablation element mapping of Py_1 also provides evidence for replacement of arsenopyrite by pyrite; if this is the case, it indicates that the invisible Au once present in the arsenopyrite was not incorporated into the pyrite (Fig. 2.12). Furthermore, the disparity in As concentrations between pyrite that occurs disseminated in D_1-D_2 schists (relatively high) and pyrite that occurs isolated within D_3

shear veins (relatively low) is consistent with recycling of some As from arsenopyrite as the hydrothermal fluids moved from arsenopyrite-stable to pyrite-stable conditions (whereas the pyrite that crystallized within D_3 shear veins may not have formed in an environment with pre-existing As). It is clear that the primary enrichment of Au in arsenopyrite (10s – 1,000s of ppm) was orders of magnitude greater than that of any subsequent pyrite generation (<0.1 – 10s of ppm) such that the replacement of arsenopyrite by pyrite would have liberated invisible gold from arsenopyrite.

Another simple mass-balance calculation demonstrates that a one-metre assay interval of 10 ppm Au would require the complete dissolution of 5 modal % arsenopyrite if that arsenopyrite had an average concentration of 200 ppm Au (as opposed to 50% pyrite by modal abundance at an average concentration of 20 ppm Au). By synthesizing the structural, mineralogical, and geochemical data for the deposit, the following model is proposed for the generation of native gold in the WGC: (1) primary Au enrichment occurred as invisible Au in arsenopyrite hosted by D_1 structures; (2) structural overprint of D_1 shear zones by D_2 deformation, contemporaneous with a shift in fluid conditions from arsenopyrite-stable to pyrite-stable and the replacement of Au-rich arsenopyrite by Au-poor pyrite, produced D_2 shear zones hosting pyrite and native gold; and (3) later mobilization occurred via LMCE melts, likely mediated by post-orogenic hydrothermal overprinting, that precipitated visible gold with Bi-Te minerals in brittle fractures of D_3 shear veins. Thus, simple mass-balance considerations are crucial in resisting the temptation to invoke multiple discrete events of novel introduction of gold based on textural, mineralogical, and geochemical differences; almost all of the gold added in the WGC can be explained by a single Au-As event in the early stages of deformation.

2.5.3 – The destabilization of Au-bearing arsenopyrite

Given the above model in which arsenopyrite was the original host for most of the gold in the deposit, and because the replacement of this Au-rich arsenopyrite by comparatively Au-poor pyrite was responsible for the formation of most of the native gold in the deposit, an appraisal of the factors that may have favoured arsenopyrite dissolution is necessary to obtain a more complete model for deposit formation. The following reaction can be used to describe the replacement of arsenopyrite by pyrite in the WGC:

$$8FeAsS + 8H_2S + 5H^+ + 5HCO_3^- + 9H_2O \rightarrow 8FeS_2 + 8As(OH)_3 + 5CH_4 \quad \text{[Reaction 2.1]}$$

Here, C^{4+} in HCO_3^- is reduced to C^{4-} in CH_4, which is commensurate with the oxidation of As^{1-} in arsenopyrite to aqueous As^{3+} in $As(OH)_3$. Note that the presence of CH_4 and CO_2 was documented in syn-deformation aqueous-carbonic fluid inclusions by Samson et al. (1997), such that both CH_4 and HCO_3^- are considered reasonable species. When considering this reaction in conjunction with a phase diagram for the Fe-As-S system in T-fS_2 space (Fig. 2.17), it is apparent that the following factors would favour the dissolution of arsenopyrite and formation of pyrite: (1) the introduction of fluids with lower concentrations of As; (2) a decrease in the temperature of the system; (3) the introduction of fluids with higher concentrations of H_2S (i.e., higher fS_2); and (4) the introduction of fluids with greater concentrations of HCO_3^-.

A disparity in As concentration exists between the pyrite disseminated in D_1-D_2 schists (Py_{1A-B} and Py_{2A-B}) and that within D_3 shear veins (Py_{3A-B}, Py_4), with the latter group being substantially poorer in As (the mean values of As concentration are between 119 – 978 ppm for the former group, compared to 3 – 5 ppm for the latter group). This mirrors what is noted at the

grain scale in Py_{2A-B}, where relatively As-rich Py_{2A} (mean: 978 ppm) was replaced by relatively As-poor Py_{2B} (mean: 190 ppm). These observations are compatible with the hypothesis that successive pulses of hydrothermal fluids in the WGC were progressively poorer in As and thus advanced the replacement of arsenopyrite by pyrite.

Paragenetic relationships amongst metamorphic biotite and chlorite are known to reflect changes in temperature (cf. Yau et al. 1984), with chlorite being stable at lower temperatures than biotite, and these minerals have been used to assess metamorphic pathways in gold deposits hosted in greenschist metamorphic terranes (e.g., Morey et al. 2007). Similarly, the magmatic-hydrothermal fluids that form porphyry Cu deposits typically evolve spatially and temporally from biotite-stable to chlorite-stable, a transition that reflects in part a decrease in temperature of the fluids (cf. Lowell and Guilbert 1970). In the WGC, biotite is common in D_1 schists with arsenopyrite (e.g., Fig. 4b), where it may be mantled and pseudomorphed by chlorite (e.g., Fig. 2.4d); conversely, chlorite is common in D_2 schists and may occur as inclusions in Py_2. Chlorite is also a regular accessory phase in D_3 shear veins. These observations indicate the chloritization of biotite, a paragenesis consistent with decreasing temperature. Although regional metamorphism is thought to have influenced the mineralogy of the shear zones that crosscut the Jubilee Stock (Studemeister 1985), these environments were also dominated by hydrothermal fluid flow that was not regional in nature (based on the localization of hydrothermal quartz, carbonates, and sulfides in the shear zones, for example). It could therefore be posited that the replacement of biotite by chlorite was not the product of a reduction in metamorphic or hydrothermal temperature, but rather the introduction of a fluid that was undersaturated with respect to biotite. Although the petrographic observations made in this study (i.e., the replacement of biotite by chlorite) fail to disprove the hypothesis that temperature decreased throughout the evolution of the WGC, they are

also permissive of other explanations, and so the role of temperature in the dissolution of arsenopyrite remains equivocal.

Variations in fS_2 throughout the evolution of the system are reflected by the stable sulfide mineral assemblages. In D_1 structures, arsenopyrite co-exists with pyrrhotite and Py_{1A} (Fig. 4f), an assemblage that can be plotted in T-fS_2 space (Fig. 2.17). Conversely, Py_{1B} is seen to partially and completely replace arsenopyrite (e.g., Figs. 2.4c, 2.12). In D_2 structures, Py_2 is the dominant sulfide and arsenopyrite and pyrrhotite occur only as inclusions inside the former. Although it is possible that these inclusions represent vestiges of pre-existing arsenopyrite and pyrrhotite, both appear to occupy pores in Py_{2A}, which is consistent with formation during CDR reactions when Py_{2A} was infiltrated and replaced by Py_{2B}; i.e., arsenopyrite and pyrrhotite formed during dissolution of Py_{2A} and precipitation of Py_{2B}.

Thus, while the transition from arsenopyrite to Py_{1B} appears to represent a shift towards arsenopyrite-unstable conditions, the formation of arsenopyrite and pyrrhotite inclusions during the crystallization of Py_{2B} indicates that physiochemical conditions during D_2 fluid flow were similar to those that enabled arsenopyrite formation during early D_1 fluid flow. This is, however, inconsistent with the hypothesis that unidirectional changes in fS_2 drove the replacement of arsenopyrite by pyrite and the associated liberation of gold. To address this inconsistency, the mineral chemistry of and the spatial distribution of inclusions within $Py_{2A\text{-}B}$ must be considered. Whereas arsenopyrite inclusions occur within domains where Py_{2B} has replaced Py_{2A}, they are spatially restricted to the original extent of Py_{2A}; that is no arsenopyrite inclusions are observed in the rims of Py_{2B} that overgrow Py_{2A}. Py_{2B} is also depleted in As relative to Py_{2A} (Fig. 2.10). Thus, it is probable that the generation of these arsenopyrite inclusions was a function of the local physiochemical environment (i.e., an input of As to the micro-system during the replacement of

As-rich Py_{2A} by As-poor Py_{2B}) and is not a reflection of the broader geochemical environment during D_2 deformation. This is consistent with the observation that, in contrast to D_1 arsenopyrite mineralization, isolated grains of arsenopyrite in D_2 rocks (i.e., disseminated in the silicate matrix, not as inclusions in Py_{2A-B}) are typically mantled and partially replaced by pyrite.

The same line of reasoning that inhibits the identification of an equilibrium pyrite + arsenopyrite + pyrrhotite assemblage during D_2 sulfide mineralization based on mineral inclusions equally precludes estimation of fS_2 conditions at that time. Several sulfide phases exist as inclusions within Py_{2A} (e.g., arsenopyrite, pyrrhotite, chalcopyrite, galena, bismuthinite), but these phases occur in pores or along fractures within relatively trace-metal-rich Py_{2A} and are absent from both trace-metal-poor Py_{2B} rims and from the silicate matrix; such observations are compatible with the hypothesis that the sulfide mineral inclusions formed from in situ CDR reactions involving Py_{2A} and Py_{2B} and that the stabilities of these minerals were dependent on grain-scale redistribution of elements like As, Cu, Pb, and Bi. The inclusion assemblages in Py_{2A-B} cannot be considered representative of the larger-scale system (e.g., the shear zone) and are therefore unsuitable to constrain the physiochemical conditions. If fS_2 did vary during the evolution of the system, thus playing a role in the relative stability of arsenopyrite, it probably increased with time (based on the phase relationships in Fig. 2.17); but this cannot be completely constrained from the sulfide assemblages in the WGC.

A final parameter that may have influenced the destruction of arsenopyrite, as outlined by Reaction 1, is the ingress of fluids with higher concentrations of HCO_3^-. Samson et al. (1997) noted a wide range in the ratio of CO_2 : CH_4 in fluid inclusions from the WGC (the former of these being the species that would correspond to higher concentrations of HCO_3^- in the fluid) and posited that this ratio increased throughout deposit formation. The deposit paragenesis as interpreted by

Samson et al. (1997) is different from that presented in this work (as will be discussed below), meaning that the former's interpretations cannot be directly applied here. The existence of fluid inclusions with diverse concentrations of CH_4 and CO_2 allows for speculation that these species were relevant to the progression of Reaction 1, but this additional analyses of fluid inclusions from samples collected and described in the present study would be required to place these fluids in the current paragenetic context.

2.5.4 – Towards a regional model for gold mineralization in the Michipicoten greenstone belt

2.5.4.1 – Re-evaluating the deposit model for the WGC

A previous study on gold mineralization in the WGC (Samson et al. 1997) proposed the following sequence of events for deposit evolution: (1) pre-kinematic quartz + carbonate + chlorite + tourmaline veining within shear zones; (2) later syn-kinematic quartz + tourmaline extension veins; and (3) post-kinematic quartz + carbonate veins. Importantly, the first veining event (i.e., the pre-kinematic veins) was suggested as the major Au host and thus mineralization as pre-kinematic. This contrasts with the current study, which relates the main gold event to syn-deformation arsenopyrite formation. The investigations of Samson et al. (1997) were focused on the isotopic and chemical characteristics of the mineralizing fluids; given that the structural and mineralogical character of the deposit is now much better constrained, it is possible to reconcile the differences in interpretations between the two studies, and a part of this exercise is the timing of the major vein types in the deposit.

Samson et al. (1997) discerned two styles of quartz + tourmaline + carbonate ± chlorite veining based on their relationships to the structural fabrics (i.e., either contained within the foliation or discordant to and deformed by the foliation). In fact, these vein sets likely belong to the same

hydrothermal event (syn-D_3), and their relationship to deformation fabrics is determined by the shear zone in which they occur. For example, a quartz + tourmaline vein that crosscuts a D_2 shear zone during the waning stages of D_2 deformation may be discordant to the foliation and have irregular margins. Such a vein may have been identified as an en echelon vein by Samson et al. (1997). Conversely, the quartz + tourmaline veins whose margins are parallel to the schistosity and were described by Samson et al. (1997) as pre-deformational dominantly occur in D_3 shear zones, where their relationship to the structural fabric (i.e., parallel) supports syn-D_3 formation. Additionally, all investigated gold mineralization in quartz + tourmaline veins in this study clearly post-dates vein formation and occurs with Bi-Te-minerals in cross-cutting carbonate-rich veinlets; this style of gold mineralization is interpreted here to be related to mobilization of earlier syn-deformation gold and does not represent primary gold mineralization during quartz + tourmaline vein formation. Even if some individual veins studied by Samson et al. (1997) were in fact pre-deformation (although such observations were not verified in the current investigation), it is likely that any gold mineralization hosted in such veins did not form prior to deformation.

A focused discussion on the timing of formation for various vein types is tangential to the fact that most of the gold in the deposit is found in quartz + carbonate + muscovite ± chlorite ± biotite schists with either disseminated arsenopyrite (in D_1 structures) or As-bearing pyrite (in D_2 structures). A syn-deformational timing for gold introduction is characteristic of Archean orogenic gold systems (e.g., Groves et al. 1998, Goldfarb & Groves 2015), as is the occurrence of primary Au dissolved in Fe-As sulfides and later formation of secondary native gold via liberation of Au from these minerals during recrystallization (e.g., Mumin et al. 1994, Morey et al. 2008, Deol et al. 2012, Cook et al. 2013, Kerr et al. 2018, Gourcerol et al. 2018, Gourcerol et al. 2020); these statements are true for gold mineralization in the WGC. Greenstone belt-hosted orogenic gold

deposits also tend to form during regional greenschist facies metamorphism (Groves et al. 1998, Goldfarb et al. 2005). Although placing the deformation and hydrothermal alteration that formed the WGC in a regional metamorphic context was not a focus of this study, previous work has suggested that the development of shear zones in the Jubilee Stock was contemporaneous with greenschist facies metamorphism in the MGB (Studemeister 1985). Based on these criteria, the WGC is best described as an orogenic gold deposit.

2.5.4.2 – Comparison with other gold deposits in the MGB

Given the modifications made above to the model for gold mineralization in the WGC, a re-examination of interpretations (i.e., those of McDivitt et al. 2017, 2018; and Haroldson 2014) that incorporated the information presented in Samson et al. (1997) is required. Through structural (McDivitt et al. 2017) and geochemical (McDivitt et al. 2018) analysis of the Missanabie-Renabie system, these researchers determined that pre-ductile deformation quartz veins and associated alteration envelopes acted as planes of rheological contrast that focused later orogenic deformation. Because these pre-orogenic veins are gold-bearing, they proposed a hybrid model for the deposit (i.e., contributions of Au from both magmatic-hydrothermal and syn-orogenic fluids; McDivitt et al. 2018). Similar conclusions were drawn by Haroldson (2014) for the Magino deposit, who noted that, although numerous hydrothermal fluids infiltrated the host rocks, gold-bearing assemblages occur in: (1) pre-, or possibly syn-orogenic porphyry-like veins that contain gold with pyrite, chalcopyrite, sphalerite, pyrrhotite, galena, and molybdenite; and (2) post-orogenic carbonate veinlets with gold and Au-Ag-Te-Bi-minerals. The resemblances in apparent gold-forming processes between the studies at Missanabie-Renabie (McDivitt et al. 2017, 2018), Magino (Haroldson 2014), and the WGC (Samson et al. 1997) prompted McDivitt et al. (2017, 2018) to posit a regional model for gold mineralization in the MGB involving Au-bearing

magmatic-hydrothermal activity as a precursor to orogenesis and subsequent formation of hybrid deposits. The occurrence of randomly oriented quartz + biotite veinlets that crosscut massive, albitized tonalite (Fig. 2c) is compatible with the hypothesis that pre-orogenic magmatic-hydrothermal activity affected the Jubilee stock. Such alteration assemblages may coexist with sulfide mineralization (e.g., pyrite, pyrrhotite, chalcopyrite, molybdenite, arsenopyrite) and grades up to 1 g/t Au, although this has only been documented adjacent to major Au-bearing shear zones. Based on the available field and drill-core observations and assay data, it is probable that a magmatic-hydrothermal system developed prior to the onset of deformation. Without detailed petrographic and geochemical investigations, the hypothesis that this gold mineralization relates to the syn-deformation fluids that migrated along the nearby shear zones, and not to the pre-orogenic magmatic-hydrothermal fluids that affected the tonalite, cannot be discarded, and so the source of gold in these locations is equivocal. Furthermore, although the silicate mineral assemblages that may be associated with magmatic-hydrothermal alteration (e.g., quartz ± albite ± biotite ± chlorite) are widespread, occurring up to several kilometres away from major shear zones, potentially economic gold mineralization (> 2-3 g/t) is restricted to the shear zones. This restricted spatial distribution is inconsistent with ore-grade enrichment of Au during pre-deformation magmatic-hydrothermal activity; introduction of gold to the shear zones that constitute the WGC was syn-deformation and the deposit is probably best considered as belonging to the orogenic class of gold deposits, rather than a hybrid between magmatic-hydrothermal and orogenic styles.

Unraveling the timing of gold mineralization in systems that experienced a protracted and diverse hydrothermal history is challenging; given the present discussion, it is important to acknowledge that magmatic-hydrothermal activity may have preceded deformation and syn-

orogenic fluid flow without contributing gold to the system; in these cases, it would not be appropriate to classify the deposit as a hybrid gold deposit. Clear identification of the timing of gold mineralization with respect to deformation, while difficult, is essential. As established previously, a syn-orogenic timing for gold mineralization is likely for the WGC. Investigations of the Island Gold deposit report similar findings, in that gold occurs with pyrite in syn-D_2 quartz veins (e.g., Jellicoe 2019, Ciufo 2019). The timing of gold mineralization at the Magino deposit, however, is not well-constrained. Although Haroldson (2014) invoked a magmatic source for the mineralizing fluids that formed the Magino deposit, and documented pre-deformation, magmatically-derived quartz veins that host gold, it is also noted that gold mineralization post-dates these veins and suggested that they only served as a rheological and potentially chemical heterogeneity that focused the formation of ore. Furthermore, gold + arsenopyrite + base-metal sulfide inclusions in pyrite were described, which were taken to indicate the envelopment of pre-existing porphyry-style gold mineralization in later pyrite that is zoned with respect to As (Haroldson 2014). The occurrence of gold and sulfide inclusions in As-bearing pyrite is more commonly attributed to the liberation of trace metals, including Au, during pyrite CDR (cf. Morey et al. 2008, Kerr et al. 2018, Hastie et al. 2020) and this hypothesis was not discounted by Haroldson (2014). Thus, the timing of pyrite formation with respect to deformation at Magino may be critical in determining the timing of the principal gold-mineralizing event. Given that a well-constrained structural framework for the deposit does not appear to have been developed, it is argued here that, while evidence for pre-orogenic magmatic-hydrothermal activity exists, the timing of gold mineralization at Magino remains equivocal. Although the hybrid hypothesis, meaning contributions of Au from both pre-orogenic magmatic-hydrothermal activity and syn-orogenic fluid flow (McDivitt et al., 2017, 2018), appears to be appropriate for the Missanabie-

Renabie camp and may apply to the Magino deposit (Haroldson 2014), it is inconsistent with observations at the Island Gold deposit (Jellicoe 2019, Ciufo 2019) and the WGC.

The timing of gold mineralization in the WGC and Island Gold deposits (i.e., syn-deformation) appears to distinguish them from the Missanabie-Renabie deposit (i.e., mostly pre-deformation, with a second syn-deformation event). The isotopic characteristics ($\delta^{34}S$) of the sulfides in these systems portray a similar division (Fig. 2.15), in that the sulfides in the WGC (present study) and Island Gold deposit (Ciufo 2019) overlap in the range of 0.1 to 4.1 ‰, whereas those from Missanabie-Renabie (McDivitt et al. 2020) have values in the range of -3.1 to -5.8 ‰. These contrasting signatures support a different source of sulfur in the fluids that formed the Missanabie-Renabie deposit as compared to the WGC and Island Gold systems, and equally do not discount a different source of Au-mineralizing fluids for the former deposit.

2.5.4.3 – Foundations for a new model

Despite unresolved differences in the timing of gold mineralization, empirical similarities exist among deposits in the Michipicoten greenstone belt. Previous evidence for common fluid sources amongst the deposits was summarized by McDivitt et al. (2018), who noted: (1) observations of an unmixed H_2O-CO_2 fluid at the Missanabie-Renabie deposit (McDivitt et al. 2018), Magino deposit (Haroldson 2014), and WGC (Samson et al., 1997); and (2) similar enrichment in ^{18}O of vein carbonates and how these contrast with other Archean gold deposits, such as those in the Abitibi greenstone belt (e.g., Kerrich 1990, Samson et al. 1997, McDivitt et al. 2018). Recent investigations of the $\Delta^{33}S$ values of ore sulfides at the Island Gold deposit (pyrite and pyrrhotite; Ciufo 2019) and Renabie (pyrite; McDivitt et al. 2020) are similar to those for the WGC (present study; pyrite), overlapping in a limited range of $\Delta^{33}S$ values centered around zero

per mil (Fig. 2.15). The lack of positive or negative anomalies (relative to zero) in $\Delta^{33}S$ for the WGC pyrite is consistent with an igneous or metamorphic source of S and indicates an absence of surficial S contributions (cf. Sakthi Saravanan & Mishra 2009, Zhao et al. 2013, Laflamme et al. 2018). This mirrors the conclusions of Ciufo (2019) and McDivitt et al. (2020), who suggested that the ore-forming fluids responsible for mineralization in the Island Gold and Missanabie-Renabie deposits, respectively, were derived from magmas or metamorphic devolatilization below the deposit. Even if the deposit-scale fluid parageneses are different among these deposits, the broad overlap in fluid chemistry and isotopic composition of hydrothermal carbonates and sulfides speak to a common hydrothermal parentage for deposits in the MGB.

Another consistent feature among these deposits is the occurrence of pre-kinematic hydrothermal activity: this is represented in the WGC by hydrothermal albite, biotite, and quartz in massive tonalite and hydrothermal chlorite in massive gabbro dykes; in the Missanabie-Renabie district by phyllic alteration bordering Au-bearing quartz veins (McDivitt et al. 2017); and in the Magino deposit by quartz veins associated with porphyry dykes that cross-cut the host Webb Lake stock (Haroldson 2014). In contrast to a magmatic-hydrothermal source, pre-deformation alteration of the host rocks to the Island Gold deposit is attributed to the onset of greenschist-facies metamorphism (Jellicoe 2019, Ciufo 2019). Regardless of fluid origin (i.e., magmatic-hydrothermal or metamorphic), the formation of alteration assemblages in the intermediate stocks enhanced the competency contrast between various units within and marginal to the stocks and these rheological contacts acted as focal points for the formation of shear zones during later deformation (e.g., Haroldson 2014, McDivitt et al. 2017, Jellicoe 2019). Rheological heterogeneity is an essential ingredient in the localization of shear zones and gold-mineralizing fluids and, in certain cases, can provide an explanation for the spatial association between orogenic gold deposits

and intermediate to felsic plutonic rocks without invoking the pluton as a source of gold (e.g., Witt 1992, Kisters et al. 2000, Hough et al. 2010).

Finally, the occurrence of gold and Bi-Te(-Ag)-minerals in post-deformation, carbonate-rich veinlets is observed in both the WGC and the Magino deposit and, in both cases, attributed to mobilization of earlier gold by post-orogenic magmatic-hydrothermal fluids during alkalic magmatism (Haroldson 2014). A model for the formation of the gold deposits in the Michipicoten greenstone belt that relies on the introduction of gold by pre-deformation magmatic-hydrothermal fluids fails to account for several of the deposits (e.g., the WGC and the Island Gold deposit). At the cost of some specificity, a more inclusive model may be summarized as follows: (1) modification of intermediate, K-poor intrusive rocks by greenschist-facies metamorphism or magmatic fluids and associated enhancement of rheological heterogeneity; (2) localization of shear zones and other brittle-ductile structures in regions of high competency contrast during deformation; (3) focusing of syn-deformation hydrothermal fluids, sourced from devolatilization of metamorphic rocks or magmas at depth, along actively deforming structures; and (4) a post-deformation magmatic-hydrothermal overprint that formed Au-LMCE assemblages in brittle structures. Gold may be introduced during Stage 1 (e.g., Missanabie-Renabie) or Stage 3 (e.g., the WGC or the Island Gold deposit). Importantly, this model accounts for the repeated occurrence of gold deposits adjacent to or cross-cutting various intermediate to felsic stocks in the Michipicoten greenstone belt and future exploration in the region should focus on these environments. Still, given the differences in timing of gold mineralization and in the source of sulfur (and thus potentially Au-mineralizing fluids) in the studied systems, it is reasonable to question whether a single model can or should be developed to account for the formation of gold deposits in the MGB. Further structural, mineralogical, and geochemical research on these deposits and others in the

Michipicoten greenstone belt will help to refine deposit-scale parageneses and to assess the extent to which Au enrichment in these systems can be explained by a common genetic model.

2.6 – Conclusions

The WGC is an important example of how a single episode of Au enrichment (i.e., D_1 gold + arsenopyrite) can be modified and mobilized to generate multiple temporally, mineralogically, and geochemically distinct gold-bearing assemblages (i.e., D_2 gold + $Py_{2A\text{-}B}$, post-deformation gold + Bi-Te minerals). Given that shear zone-hosted gold deposits in metamorphic terranes are typically characterized by protracted hydrothermal and structural histories, the hypothesis that gold mineralization was the product of an initial event (i.e., primary enrichment) and was then modified during subsequent mobilization events (i.e., secondary enrichment) should always be tested before multiple episodes of Au introduction to the system are invoked. Mass-balance calculations involving comparisons of the concentrations of Au in sulfide minerals to those of whole-rock Au can be helpful in this exercise.

Gold deposits in the MGB appear to be characterized by pre-deformation hydrothermal modification of the igneous host rocks, by syn-deformation fluids sourced from magmas or metamorphic degassing, and sometimes by post-deformation magmatic-hydrothermal overprinting. Most of the gold in these deposits is interpreted to have been introduced either during the pre-deformation fluid event (e.g., Missanabie-Renabie) or during the syn-deformation fluid event (e.g., the WGC, Island Gold). It is unclear whether this key difference in timing is a result of variations on a single model for deposit formation (a possible model was proposed in the present work), or of fundamentally different processes and fluid sources.

2.7 – References

Barton Jr., P.B., 1969, Thermochemical study of the system Fe-As-S: Geochimica et Cosmochimica Acta, v. 33(7), p. 841-857.

Bateman, R., Ayer, J.A., and Dubé, B., 2008, The Timmins-Porcupine Gold Camp, Ontario: Anatomy of an Archean Greestone Belt and Ontogeny of Gold Mineralization: Economic Geology, v. 103, p. 1285-1308.

Beirlein, F.P., Groves, D.I., Goldfarb, R.J., and Dubé, B., 2006, Lithospheric controls on the formation of provinces hosting giant orogenic gold deposits: Mineralium Deposita, v. 40, p. 874-886.

Béziat D., Dubois, M., Debat, P., Nikiéma, S., Salvi, S., and Tollon, F., 2008, Gold metallogeny in the Birimian craton of Burkina Faso (West Africa): Journal of African Earth Sciences, v. 50, p. 215-233.

Buhn, B., Santos, R.V., Dardenne, M.A., and de Oliveira, C.G., 2012, Mass-dependent and mass-independent sulfur isotope fractionation ($\delta^{34}S$ and $\delta^{33}S$) from Brazilian Archean and Proterozoic sulfide deposits by *laser* ablation multi-collector ICP-MS: Chemical Geology, v. 312-313, p. 163-176.

Cabri, L.J., Chryssoulis, S.L., de Villiers, J.P.R., Laflamme, J.H.G., and Buseck, P.R., 1989, The nature of “invisible” gold in arsenopyrite: Canadian Mineralogist, v. 27, p. 353-362.

Cave, B.J., Barnes, S.-J., Pitcairn, I.K., Sack, P.J., Kuikka, H., Johnson, S.C., and Duran, C.J., 2019, Multi-stage precipitation and redistribution of gold, and its collection by lead-

bismuth and lead immiscible liquids in a reduced-intrusion related gold system (RIRGS); Dublin Gulch, western Canada: Ore Geology Reviews, v. 106, 28-55.

Ciobanu, C.L., Cook, N.J., Damian, F., and Damina, G., 2006, Gold scavenged by bismuth melts: An example from Alpine shear-remobilizates in the Highiş Massif, Romania: Mineralogy and Petrology, v. 87, p. 351-384.

Ciobanu, C.L., Birch, W.D., Cook, N.J., Pring, A., and Grundler, P.V., 2010, Petrogenetic significance and Au-Bi-Te-S associations: The example of Maldon, Central Victorian gold province, Australia: Lithos, v. 116, p. 1-17.

Ciobanu, C.L., Cook, N.J., Utsunomiya, S., Kogagwa, M., Green, L., Gilbert, S., and Wade, B., 2012, Gold-telluride nanoparticles revealed in arsenic-free pyrite: American Mineralogist, v. 97, p. 1515-1518.

Ciufo, T.J., 2019, Hydrothermal Alteration and Exploration Vectors at the Island Gold Deposit, Michipicoten Greenstone Belt, Wawa, Ontario: Unpublished M.Sc. thesis, Waterloo, University of Waterloo, 523 p.

Cockerton, A.B.D, and Tomkins, A.G., 2012, Insights into the Liquid Bismuth Collector Model Through Analysis of the Bi-Au Stormont Skarn Prospect, Northwest Tasmania: Economic Geology, v. 107, 667-682.

Cook, N. J., Ciobanu, C.L., and Mao, J., 2009b, Textural control on gold distribution in As-free pyrite from the Dongping, Huangtuliang and Hougou gold deposits, North China Craton (Hebei Province, China): Chemical Geology, v. 204, p. 101-121.

Cook, N.J., Ciobanu, C.L., Meria, D., Silcock, D., and Wade, B., 2013, Arsenopyrite-Pyrite Association in an Orogenic Gold Ore: Tracing Mineralization History from Textures and Trace Elements: Economic Geology, v. 108, p. 1273-1283.

Deditius, A.P., Utsunomiya, S., Renock, D., Ewing, R.C., Ramana, C.V., Becker, U., and Kesler, S.E., 2008, A proposed new type of arsenian pyrite: Composition, nanostructure and geological significance: Geochimica et Cosmochimica Acta, v. 72, p. 2919-2933.

Deditius, A.P., Utsunomiya, S., Reich, M., Kesler, S.E., Ewing, R.C., Hough, R., and Walshe, J., 2011, Trace metal nanoparticles in pyrite: Ore Geology Reviews, v. 42, p. 32-46.

Deditius, A.P., Reich, M., Kesler, S.E., Utsunomiya, S., Chryssoulis, S.L., Walshe, J., and Ewing, R.C., 2014, The coupled geochemistry of Au and As in pyrite from hydrothermal ore deposits: Geochimica et Cosmochimica Acta, v. 140, p. 644-670.

Deol, S., Deb, M., Large, R.R., and Gilbert, S., 2012, LA-ICPMS and EPMA studies of pyrite, arsenopyrite and loellingite from the Bhukia-Jagpura gold prospect, southern Rajasthan, India: Implications for ore genesis and gold remobilization: Chemical Geology, v. 326-327, p. 72-87.

Dubosq, R., Lawley, C.J.M., Rogowitz, A., Schneider, D.A., and Jackson, S., 2018, Pyrite deformation and connections to gold mobility: Insight from micro-structural analysis and trace element mapping: Lithos, v. 310-311, p. 86-104.

Eisenlohr, B.N., Groves D., and Partington, G.A., 1989, Crustal-scale shear zones and their significance to Archaean gold mineralization in Western Australia: Mineralium Deposita, v. 24, p. 1-8.

Fielding, I.O.H., Johnson, S.P., Meffre, S., Zi, J., Sheppard, S., Large, R.R., and Rasmussen, B., 2019, Linking gold mineralization to regional-scale drivers of mineral systems using in situ U-Pb geochronology and pyrite LA-ICP-MS element mapping: Geoscience Frontiers, v. 10, p. 89-105.

Fougerouse, D., Reddy, S.M., Saxey, D.W., Rickard, W.D.A., van Riessen, A., and Micklethwaite, S., 2016, Nanoscale gold clusters in arsenopyrite controlled by growth rate not concentration: Evidence from atom probe microscopy: American Mineralogist, v. 101, p. 1916-1919.

Gammons, C.H., and Williams-Jones, A.E., 1997, Chemical Mobility of Gold in the Porphyry-Epithermal Environment: Economic Geology, v. 92, p. 45-59.

George, L.L., Cook, N.J., Crowe, B.B.P., and Ciobanu, C.L., 2018, Trace elements in hydrothermal chalcopyrite: Mineralogical Magazine, v. 82(1), p. 59-88.

Goldfarb, R.J., Baker, T., Dubé, B., Groves, D.I., Hart, C.J.R., and Gosselin, P., 2005, Distribution, character, and genesis of gold deposits in metamorphic terranes: Economic Geology 100th Anniversary Volume, p. 407–450.

Goldfarb, R.J., and Groves, D.I., 2015, Orogenic gold: Common or evolving fluid and metal sources through time: Lithos, v. 233, 2-26.

Gourcerol, B., Kontak, D.J., Thurston, P.C., and Petrus, J.A., 2018, Results of LA-ICP-MS sulfide mapping from Algoma-type BIF gold systems with implications for the nature of mineralizing fluids, metal sources, and deposit models: Mineralium Deposita, v. 53, p. 871-894.

Gourcerol, B., Kontak, D.J., Petrus, J.A., and Thurston, P.C., 2020, Application of LA ICP-MS analysis of arsenopyrite to gold metallogeny of the Meguma Terrane, Nova Scotia, Canada: Gondwana Research, v. 81, p. 265-290.

Groves, D.I., Phillips, N., Ho, S.E., Houstoun, S.M., and Standing, C.A., 1987, Craton-Scale Distribution of Archean Greenstone Gold Deposits: Predictive Capacity of the Metamorphic Model: Economic Geology, v. 82, p. 2045-2058.

Groves, D.I., Goldfarb, R.J., Gebre-Mariam, M., Hagemann, S.G., and Robert, F., 1998, Orogenic gold deposits: A proposed classification in the context of their crustal distribution and relationship to other gold deposit types: Ore Geology Reviews, v. 13, p. 7-27.

Guamarães, F.S., Cabral, A. R., Lehmann, B., Rios, F. J., Ávila, M.A.B., de Castro, M.P., and Queiroga, G.N., 2019, Bismuth-melt trails trapped in cassiterite-quartz veins: Terra Nova, v. 31, p. 358-365.

Halls, H.C., and Palmer, H.C., 1990, The tectonic relationship of two Early Proterozoic dyke swarms to the Kapuskasing Structural Zone: a paleomagnetic and petrographic study: Canadian Journal of Earth Sciences, v. 27, p. 87-103.

Haroldson, E.L., 2014, Fluid inclusions and stable isotope study of magino; a magmatic related Archean gold deposit: Unpublished M.Sc. thesis, Madison, University of Wisconsin-Madison, 81 p.

Hastie, E.C.G., Kontak, D.J., and Lafrance, B., 2020, Gold Remobilization: Insights from Gold Deposits in the Archean Swayze Greenstone Belt, Abitibi Subprovince, Canada: Economic Geology, v. 115(2), p. 241-277.

Hazarika, P., Mishra, B., Chinnasamy, S.S., and Bernhardt, H.-J., 2013, Multi-stage growth and invisible gold distribution in pyrite from the Kundarkocha sediment-hosted gold deposit, eastern India: Ore Geology Reviews, v. 55, p. 134-145.

Hodkiewicz, P.F., Groves, D.I., Davidson, G.J., Weinberg, R.F., and Hagemann, S.G., 2009, Influence of structural setting on sulphur isotopes in Archean orogenic gold deposits, Eastern Goldfields Province, Yilgarn, Western Australia: Mineralium Deposita, v. 44, p. 129-150.

Hough, M.A., Bierlein, F.P., Ailleres, L., and McKnight, S., 2010, Nature of gold mineralisation in the Walhalla Goldfield, southeast Australia: Australian Journal of Earth Sciences, v. 57, p. 969-992.

Jellicoe, K., 2019, Structural Controls and Deformation History of the Orogenic Island Gold Deposit, Michipicoten Greenstone Belt, Ontario: Unpublished M.Sc. thesis, Waterloo, University of Waterloo, 84 p.

Kerr, M.J., Hanley, J.J., Kontak, D.J., Morrison, G.G., Petrus, J., Fayek, M., and Zajacz, Z., 2018, Evidence of upgrading gold tenor in an orogenic quartz-carbonate vein system by late magmatic-hydrothermal fluids at the Madrid Deposit, Hope Bay Greenstone Belt, Nunavut, Canada: Geochimica et Cosmochimica Acta, v. 241, p. 180-218.

Kerrich, R., 1990, Carbon-isotope systematics of Archean Au-Ag vein deposits in the Superior province: Canadian Journal of Earth Sciences, v. 27, p. 40-56.

Kisters, A.F.M., Meyer, F.M., Znamensky, S.E., Seravkin, I.B., Ertl, R.G.W., and Kosarev, A.M., 2000, Structural controls of lode-gold mineralization by mafic dykes in late-

Paleozoic granitoids of the Kochkar district, southern Urals, Russia: Mineralium Deposita, v. 35, p. 157-168.

Kouhestani, H., Ghaderi, M., Large, R.R., and Zaw, K., 2017, Texture and chemistry of pyrite at Chah Zard epithermal gold-silver deposit, Iran: Ore Geology Reviews, v. 84, p. 80-101.

Kretschmar, U., and Scott, S.D., 1976, Phase relations involving arsenopyrite in the system Fe-As-S and their application: Canadian Mineralogist, v. 14, p. 364-386.

Laflamme, C., Jamieson, J.W., Fiorentini, M.L., Thébaud, N., Caruso, S., and Selvaraja, V., 2018, Investigating sulfur pathways through the lithosphere by tracing mass independent fractionation of sulfur to the Lady Bountiful orogenic gold deposit, Yilgarn Craton: Gondwana Research, v. 58, p. 27-38.

Large, R.R., Danyushevsky, L., Hollit, C., Maslennikov, V., Meffre, S., Gilbert, S., Bull, S., Scott, R., Emsbo, P., Thomas, H., Singh, B., and Foster, J., 2009, Gold and Trace Element Zonation in Pyrite Using a Laser Imaging Technique: Implications for the Timing of Gold in Orogenic and Carlin-Style Sediment-Hosted Deposits: Economic Geology, v. 104, p. 635-668.

Large, R.R., Halpin, J.A., Danyushevsky, L.V., Maslennikov, V.V, Bull, S.W., Long, J.A., Gregory, D.D., Lounejeva, E., Lyons, T.W., Sack, P.J., McGoldrick, P.J., and Calver, C.R., 2014, Trace element content of sedimentary pyrite as a new proxy for deep-time ocean-atmosphere evolution: Earth and Planetary Science Letters, v. 389, p. 209-220.

Lawley, C.J.M., Jackson, S., Yang, Z., Davis, W., and Eglington, B., 2017, Tracing the Transition of Gold from Source to Sponge to Sink: Economic Geology, v. 112, p. 169-183.

Lawrence, D.M., Treloar, P.J., Rankin, A.H., Boyce, A., and Harbidge, P., 2013, A Fluid Inclusion and Stable Isotope Study at the Loulo Mining District, Mali, West Africa: Implications for Multifluid Sources in the Generation of Orogenic Gold Deposits: Economic Geology, v. 108, p. 229-257.

Lefebvre, N., Kopylova, M., and Kivi, K., 2005, Archean calc-alkaline lamprophyres of Wawa, Ontario, Canada: Unconventional diamondiferous volcaniclastic rocks: Precambrian Research, v. 138, p. 57-87.

Lowell, J.D., and Guilbert, J.M., 1970, Lateral and Vertical Alteration-Mineralization Zoning in Porphyry Ore Deposits: Economic Geology, v. 65(4), p. 373-408.

McDivitt, J.A., Lafrance, B., Kontak, D.J., and Robichaud, L., 2017, The Structural Evolution of the Missanabie-Renabie Gold District: Pre-orogenic Veins in and Orogenic Gold Setting and Their Influence on the Formation of Hybrid Deposits: Economic Geology, v. 112, p. 1959-1975.

McDivitt, J.A., Kontak, D.J., Lafrance, B., and Robichaud, L., 2018, Contrasting Fluid Chemistries, Alteration Characteristics, and Metamorphic Timing Relationships Recorded in Hybridized Orebodies of the Missanabie-Renabie Gold District, Archean Wawa Subprovince, Ontario, Canada: Economic Geology, v. 113(2), p. 397-420.

Mishra, B., Pruseth, K.L., Hazarika, P., and Chinnasamy, S.S., 2018, Nature and source of the ore-forming fluids associated with orogenic gold deposits in the Dharwar Craton: Geoscience Frontiers, v. 9, p. 715-726.

Morey, A.A., Weinberg, R.F., Bierlein, F.P., and Davidson, G.J., 2007, Gold deposits of the Bardoc Tectonic Zone: a distinct style of orogenic gold in the Archaean Eastern

Goldfields Province, Yilgarn Craton, Western Australia: Australian Journal of Earth Sciences, v. 54, p. 783-800.

Morey, A.A., Tomkins, A.G., Bierlein, F.P., Weinberg, R.F., and Davidson, G.J., 2008, Bimodal Distribution of Gold in Pyrite and Arsenopyrite: Examples from the Archean Boorara and Bardoc Shear Systems, Yilgarn Craton, Western Australia: Economic Geology, v. 103, p. 599-614.

Mumin, A.H., Fleet, M.E., and Chryssoulis, S.L., 1994, Gold mineralization in As-rich mesothermal gold ores of the Bogosu-Prestea mining district of the Ashanti Gold Belt, Ghana: remobilization of "invisible" gold: Mineralium Deposita, v. 29, p. 445-460.

Murphy, P.J. and Roberts, S., 1997, Evolution of a metamorphic fluid and its role in lode gold mineralisation in the Central Iberian Zone: Mineralium Deposita, v. 32, p. 459-474.

Novoselov, K., Belogub, E., Kotlyarov, V., and Mikhailov, A., 2015, Ore mineralogy and formation conditions of the Pirunkoukku gold occurrence (Finland): European Journal of Mineralogy, v. 27, p. 639-649.

Oberthür, T., Schmidt Mumm, A., Vetter, U., Simon, K., and Amanor, J.A., 1996, Gold Mineralization in the Ashanti Belt of Ghana: Genetic Constraints of the Stable Isotope Geochemistry: Economic Geology, v. 91, p. 289-301.

Oberthür, T., and Weiser, T.W., 2008, Gold-bismuth-telluride-sulphide assemblages at the Viceroy Mine, Harare-Bindura-Shamva greenstone belt, Zimbabwe: Mineralogical Magazine, v. 72(4), p. 953-970.

Ontario Geological Survey 2011. 1:250 000 scale bedrock geology of Ontario; Ontario Geological Survey, Miscellaneous Release---Data 126-Revision 1.

Perrouty, S., Lindsay, M.D., Jessell, M.W., Aillères, L., Martin, R., and Bourassa, Y., 2014, 3D modeling of the Ashanti Belt, southwest Ghana: Evidence for a litho-stratigraphic control on gold occurrences within the Birimian Sefwi Group: Ore Geology Reviews, v. 63, p. 252-264.

Petrella, L., Thébaud, N., Fougerouse, D., Evans, K., Quadir, Z., and Laflamme, C., 2020, Colloidal gold transport: a key to high-grade gold mineralization?: Mineralium Deposita, doi.org/10.1007s00126-020-00965-x.

Polat, A., 2009, The geochemistry of Neoarchean (ca. 2700) tholeiitic basalts, transitional to alkaline basalts, and gabbros, Wawa Subprovince, Canada: Implications for petrogenetic and geodynamic processes: Precambrian Research, v. 168, p. 83-105.

Putnis, A., 2009, Mineral replacement reactions: Reviews in Mineralogy and Geochemistry, v. 70, p. 87-124.

Reich, M., Kesler, S.E., Utsunomiya, S., Palenik, C.S., Chryssoulis, S.L.,and Ewing, R.C., 2005, Solubility of gold in arsenian pyrite: Geochimica et Cosmochimica Acta, v. 69(11), p. 2781-2796.

Robert, F., 2001, Syenite-associated disseminated gold deposits in the Abitibi greenstone belt, Canada: Mineralium Deposita, v. 36, p. 503-516.

Robert, F., and Kelly, W.C., 1987, Ore-Forming Fluids in Archean Gold-Bearing Quartz Veins at the Sigma Mine, Abitibi Greenstone Belt, Quebec, Canada: Economic Geology, v. 82, p. 1464-1482.

Sage, R.P., 1988, Geology of carbonatite-alkalic rock complexes of Ontario: Firesand River Carbonatite Complex, District of Algoma: Ontario Geological Survey Study 47, 81 p.

Sakthi Saravanan, C., and Mishra, B., 2009, Uniformity in sulfur isotope composition in the orogenic gold deposits from the Dharwar Craton, southern India: Mineralium Deposita, v. 44, p. 597-605.

Samson, I.M., Bas, B., and Holm, P.E., 1997, Hydrothermal Evolution of Auriferous Shear Zones, Wawa, Ontario: Economic Geology, v. 92, p. 325-342.

Stachel, T., Banas, Anetta, Muehlenbachs, K., Kurszlaukis, S., and Walker, E.C., 2006, Archean diamonds from Wawa (Canada): samples from deep cratonic roots predating cratonization of the Superior Province: Contributions to Mineralogy and Petrology, v. 151, p. 737-750.

Su, W., Xia, B., Zhang, H., Zhang, X., and Hu, R., 2008, Visible gold in arsenian pyrite at the Shuiyindong Carlin-type gold deposit, Guizhou, China: Implications for the environment and processes of ore formation: Ore Geology Reviews, v. 33, p. 667-679.

Sullivan, R.W., Sage R.P., and Card, K.D., 1985, U-Pb zircon age of the Jubilee stock in the Michipicoten greenstone belt near Wawa, Ontario: Geological Survey of Canada paper, n. 85-1B, p. 361-365.

Sung, Y.-H., Brugger, J., Ciobanu, C.L., Pring, A., Skinner, W., and Nugus, M., 2009, Invisible gold in arsenian pyrite and arsenopyrite from a multistage Archaean gold deposit: Sunrise Dam, Eastern Goldfields Province, Western Australia: Mineralium Deposita, v. 44, p. 765-791.

Symons, D.T.A., 1989, Age of the Firesand River carbonatite complex from paleomagnetism: Canadian Journal of Earth Sciences, v. 26, p. 2401-2405.

Tomkins. A.G., Pattison, D.R.M., and Zaleski, E., 2004, The Hemlo Gold Deposit, Ontario: An Example of Melting and Mobilization of a Previous Metal-Sulfosalt Assemblage during Amphibolite Facies Metamorphism and Deformation: Economic Geology, v. 99, p. 1063-1084.

Turek, A., Smith, P.E., and van Schmus, W.R., 1982, Rb-Sr and U-Pb ages of volcanism and granite emplacement in the Michipicoten belt – Wawa, Ontario: Canadian Journal of Earth Sciences, v. 19, p. 1608-1626.

Turek, A., Sage, R.P., and van Schmus, W.R., 1992, Advances in the U-Pb zircon geochronology of the Michipicoten greenstone belt, Superior Province, Ontario: Canadian Journal of Earth Sciences, v. 29, p. 1154-1165.

Velásquez, G., Béziat, D., Salvi, S., Siebenaller, L., Borisova, A.Y., Pokrovski, G.S., and de Parseval, P., 2014, Formation and Deformation of Pyrite and Implications for Gold Mineralization in the El Callao District, Venezuela: Economic Geology, v. 109, p. 457-486.

Voudouris, P.C., Spry, P.G., Mavrogonatos, C., Sakellaris, G.-A., Bristol, S.K., Melfos, V., and Fornadel, A.P., 2013, Bismuthinite derivatives, lillianite homologues, and bismuth

sulfotellurides as indicators of gold mineralization in the Stanos shear-zone related deposit, Chalkidiki, Northern Greece: Canadian Mineralogist, v. 51, p. 119-142.

Williams-Jones, A.E., Bowell, R.J., and Migdisov, A.A., 2009, Gold in Solution: Elements, v. 5, p. 281-287.

Witt, W.K., 1991, Regional metamorphic controls on alteration associated with gold mineralization in the Eastern Goldfields province, Western Australia: Implications for the timing and origin of Archean lode-gold deposits: Geology, v. 19, p. 982-985.

Witt, W.K., 1992, Porphyry intrusions and albitites in the Bardoc-Kalgoorlie area, Western Australia, and their role in Archean epigenetic gold mineralization: Canadian Journal of Earth Sciences, v. 29, p. 1609-1622.

Yau, Y.-C., Anovitz, L.M., Essene, E.J., and Peacor, D.R., 1984, Phlogopite-chlorite reaction mechanisms and physical conditions during retrograde reactions in the Marble Formation, Franklin, New Jersey: Contributions to Mineralogy and Petrology, v. 88, p. 299-306.

Zhang, J., Deng, J., Chen, H.-y., Yang, L.-q., Cooke, D., Danyushevsky, L., and Gong, Q.-j., 2014, LA-ICP-MS trace element analysis of pyrite from the Chang'an gold deposit, Sanjiang region, China: Implication for ore-forming process: Gondwana Research, v. 26, p. 557-575.

Zhao, C., Ni, P., Wang, G.-G., Ding, J.-Y., Chen, H., Zhao, K.-D., Cai, Y.-T., and Xu, Y.-F., 2013, Geology, fluid inclusion, and stable isotope constraints on ore genesis of the Neoproterozoic Jinshan orogenic gold deposit, South China: Geofluids, v. 13, p. 506-527.

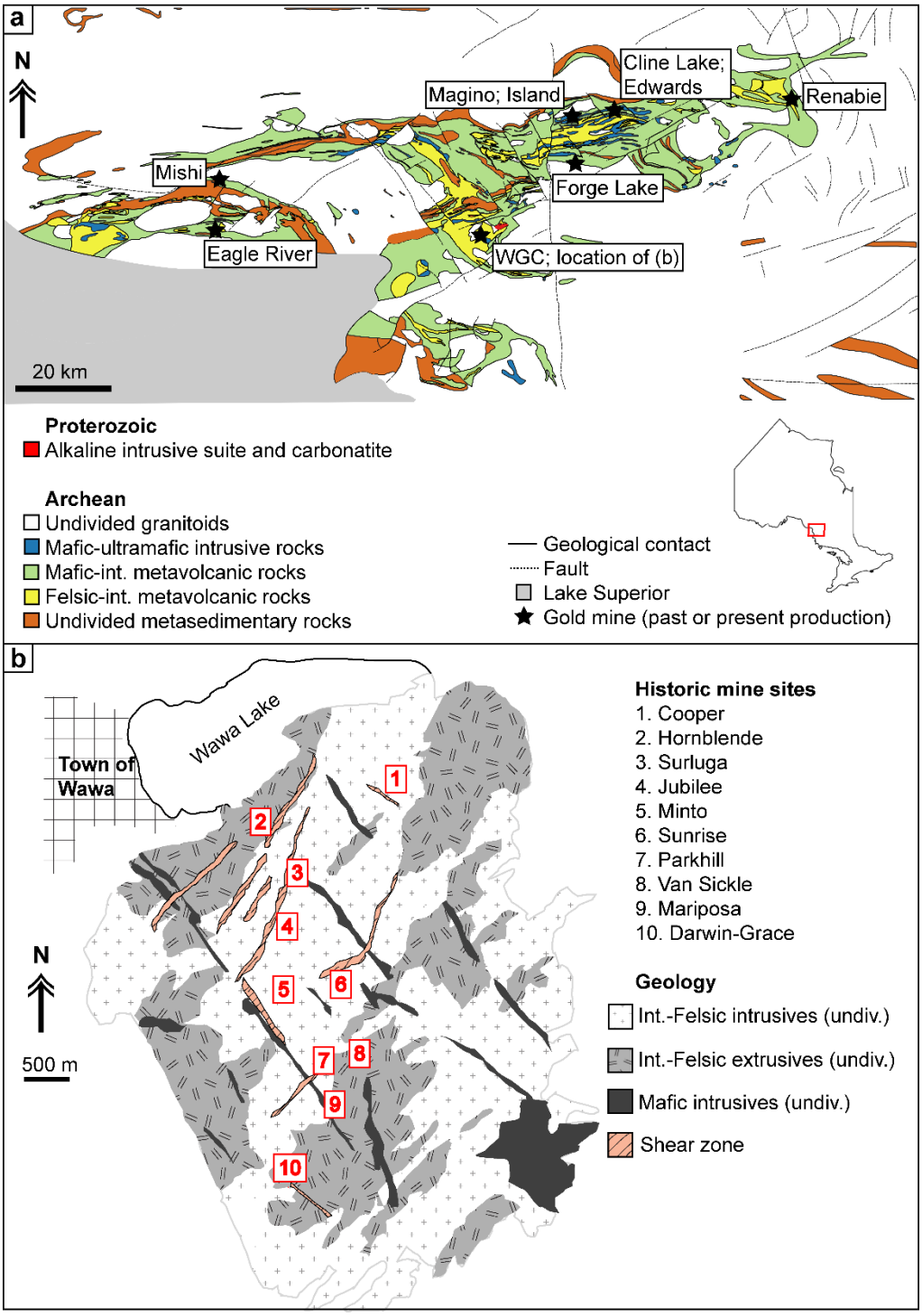

Figure 2.1 – (a) Simplified geology of the Michipicoten greenstone belt with data from Ontario Geological Survey MRD 126-1 and deposit locations from the Mineral Deposit Inventory of Ontario (https://data.ontario.ca/dataset/mineral-deposit-inventory-of-ontario). (b) Simplified geology of the Jubilee stock based on Red Pine Exploration's internal maps.

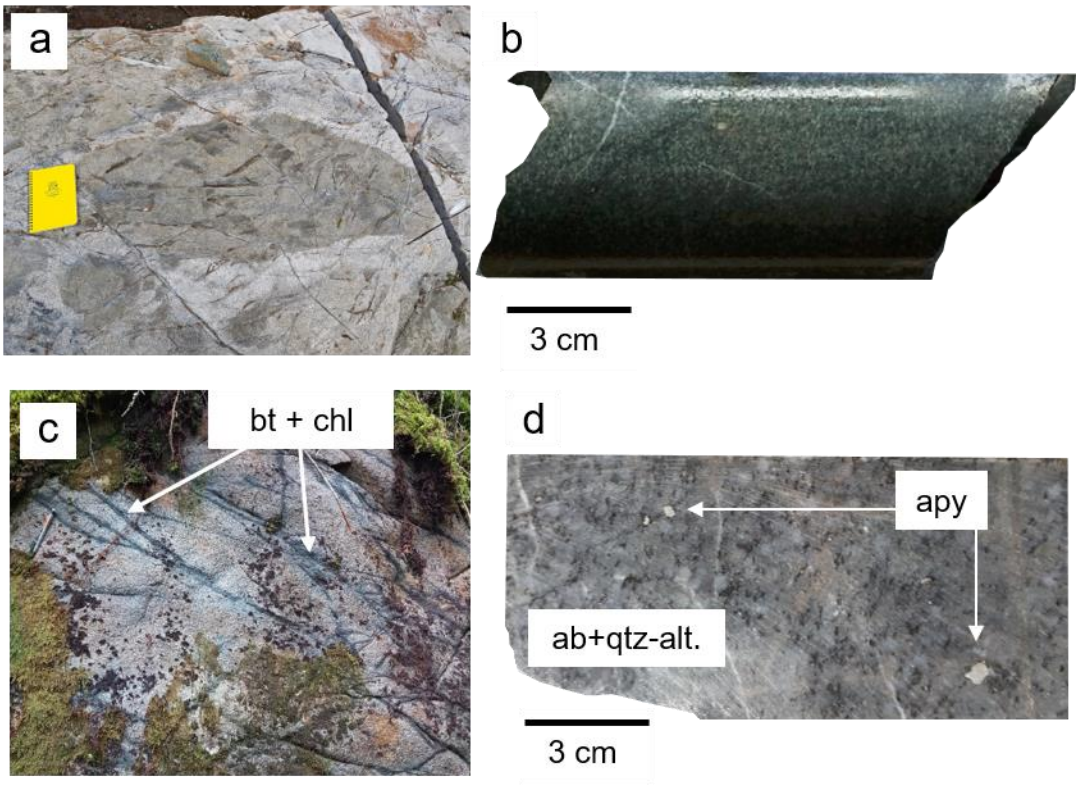

Figure 2.2 – Field and drill core photographs of rocks from the Jubilee stock. (a) Xenoliths of volcanic rock in tonalite. (b) Undeformed, chlorite-altered gabbro dyke; (c) randomly oriented biotite-chlorite veinlets cutting massive, albitized and silicified tonalite; and (d) coarse-grained arsenopyrite in massive, albitized and silicified tonalite. The book in (a) is 20 cm across; the pencil in (c) is 15 cm long.

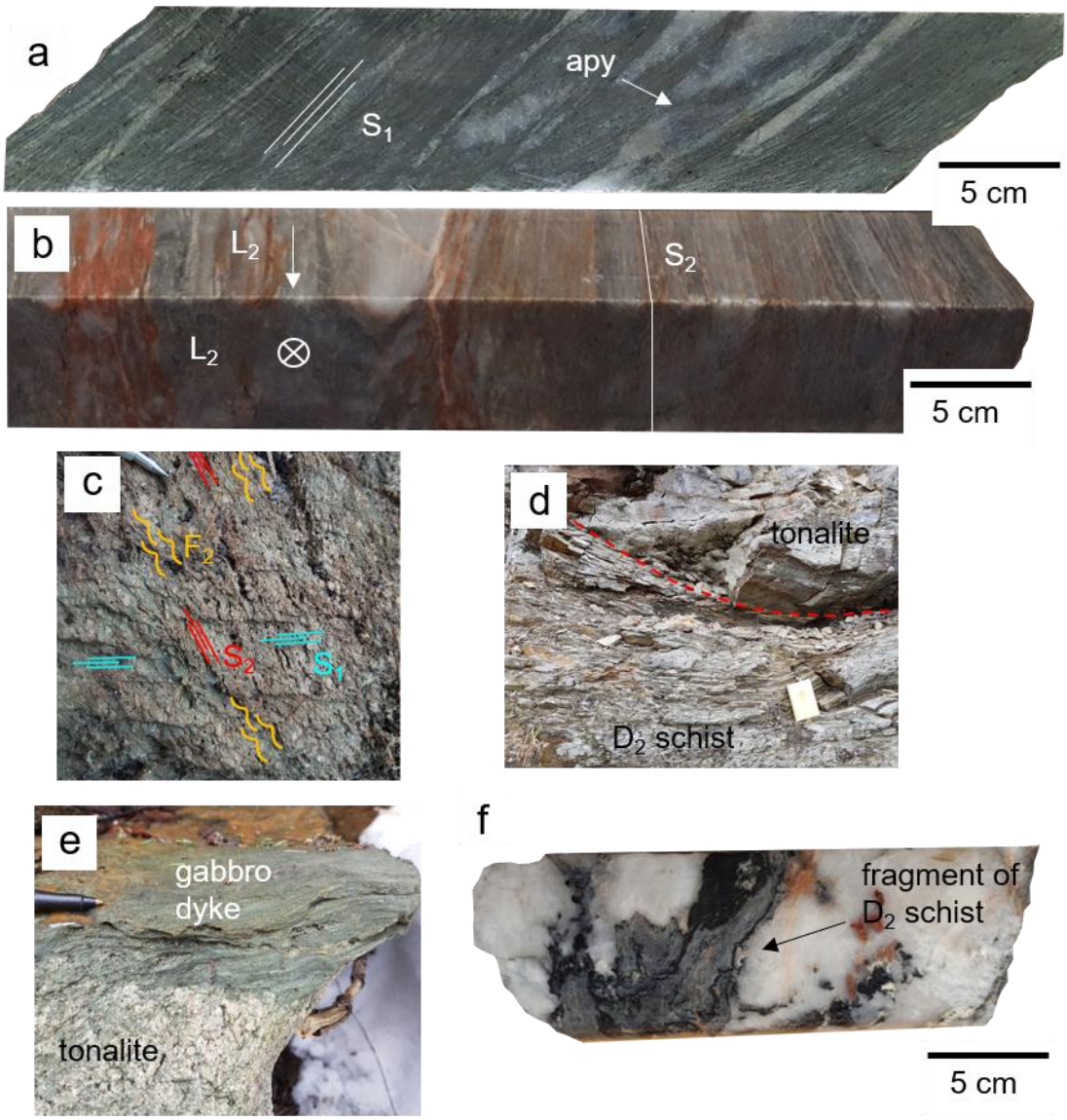

Figure 2.3 – Structural fabrics and relationships in rocks of the Jubilee stock. (a) Bands of fine-grained arsenopyrite contained in S_1. (b) Stretched rods of quartz that define L_2. (c) Overprinting of S_2 on S_1 and the formation of cm-scale F_2 folds. (d) Deflection of D_2 shear zone around massive tonalite block. (e) Strain partitioning between a gabbro dyke protolith and tonalite. (f) Inclusion of D_2 wall-rock within cross-cutting D_3 vein. The tip of the scribe in (c) is five mm long; the book in (d) is 20 cm across; and the visible portion of the pen in (e) is one cm long.

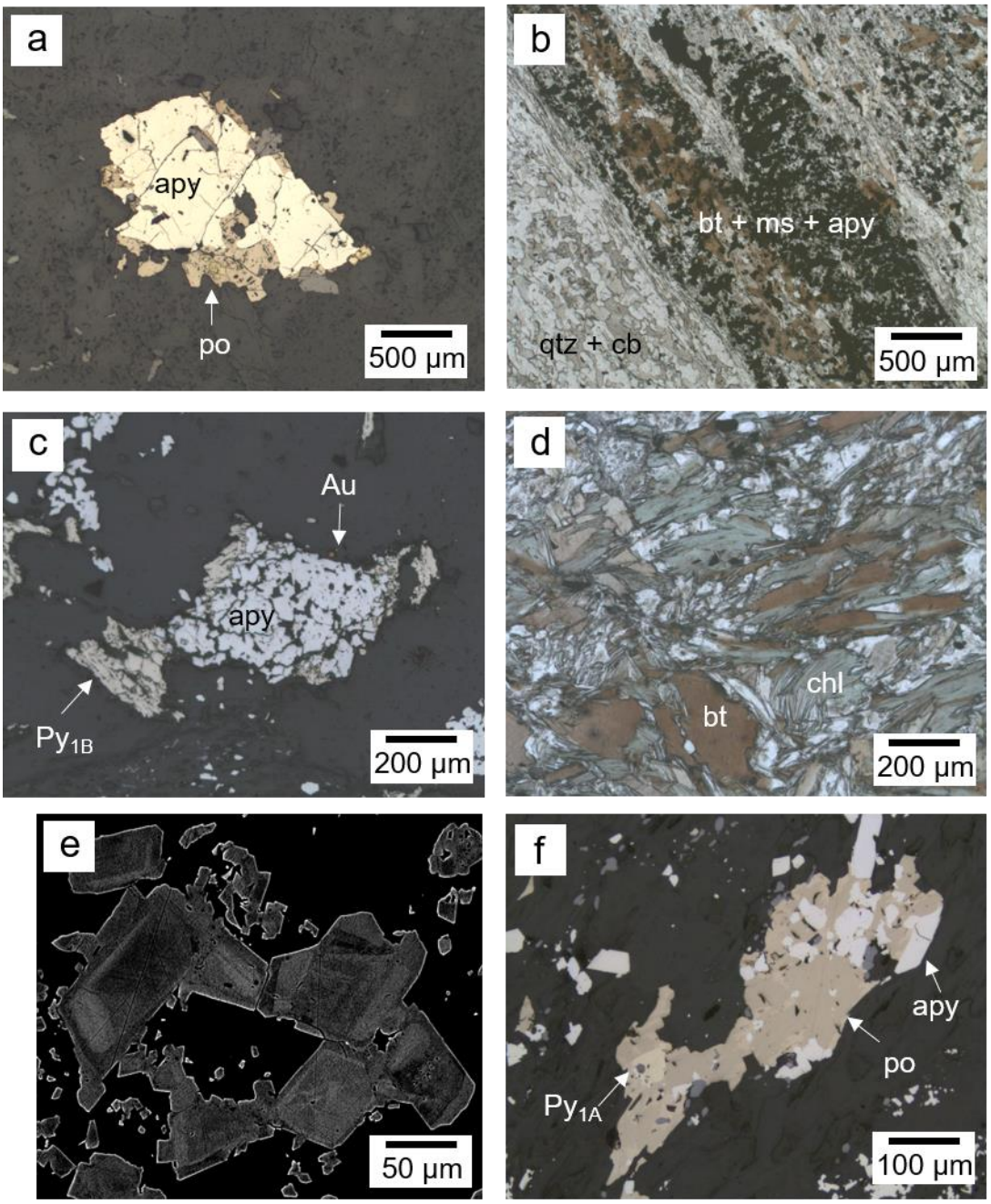

Figure 2.4 – Representative mineral assemblages and textures from D_1 schists. (a) Coarse-grained, pre-deformation arsenopyrite in undeformed tonalite (note the disequilibrium textures between earlier arsenopyrite and later pyrrhotite). (b) Bands of disseminated arsenopyrite with seams of biotite and muscovite contained in S_1. (c) Anhedral Py_{1B} on the margins of a cluster of arsenopyrite. (d) Chlorite alteration rims on biotite. (e) Compositional zoning within grains of arsenopyrite. (f) Arsenopyrite and a grain of euhedral Py_{1A} enclosed in elongated pyrrhotite. All pictures were taken with an optical microscope except for (e), which is a high-contrast BSE image.

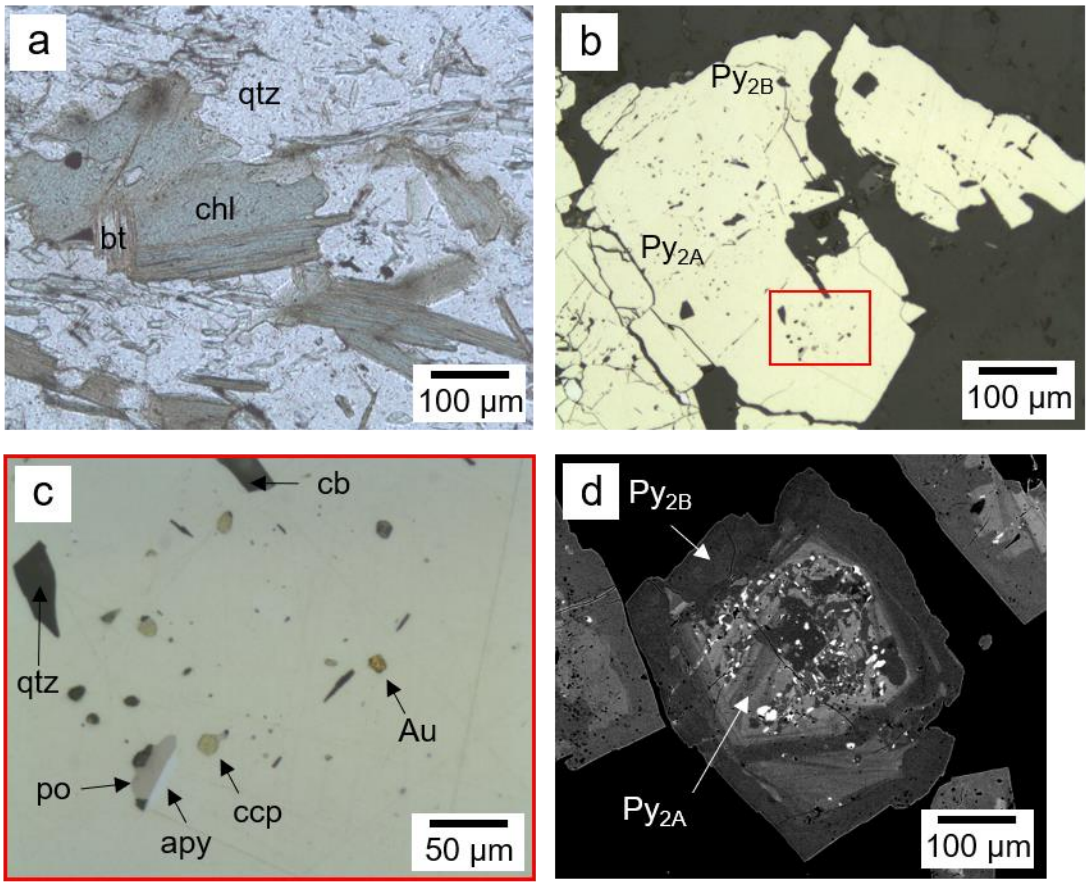

Figure 2.5 – Representative mineral assemblages and textures from D_2 schists. (a) Replacement of biotite by chlorite; (b) porphyroblastic Py_2 with inclusion-rich core (Py_{2A}) and inclusion-poor margin (Py_{2B}); (c) close-up of the grain in (b) showing inclusions of quartz, carbonate, pyrrhotite, arsenopyrite, chalcopyrite, and gold; and (d) internal textures of Py_2, showing the overgrowth and replacement of Py_{2A} by Py_{2B}. The BSE-bright inclusions in the Py_{2A} core in (d) are dominated by arsenopyrite, chalcopyrite, and pyrrhotite. All pictures were taken with an optical microscope except for (d), which is a high-contrast BSE image.

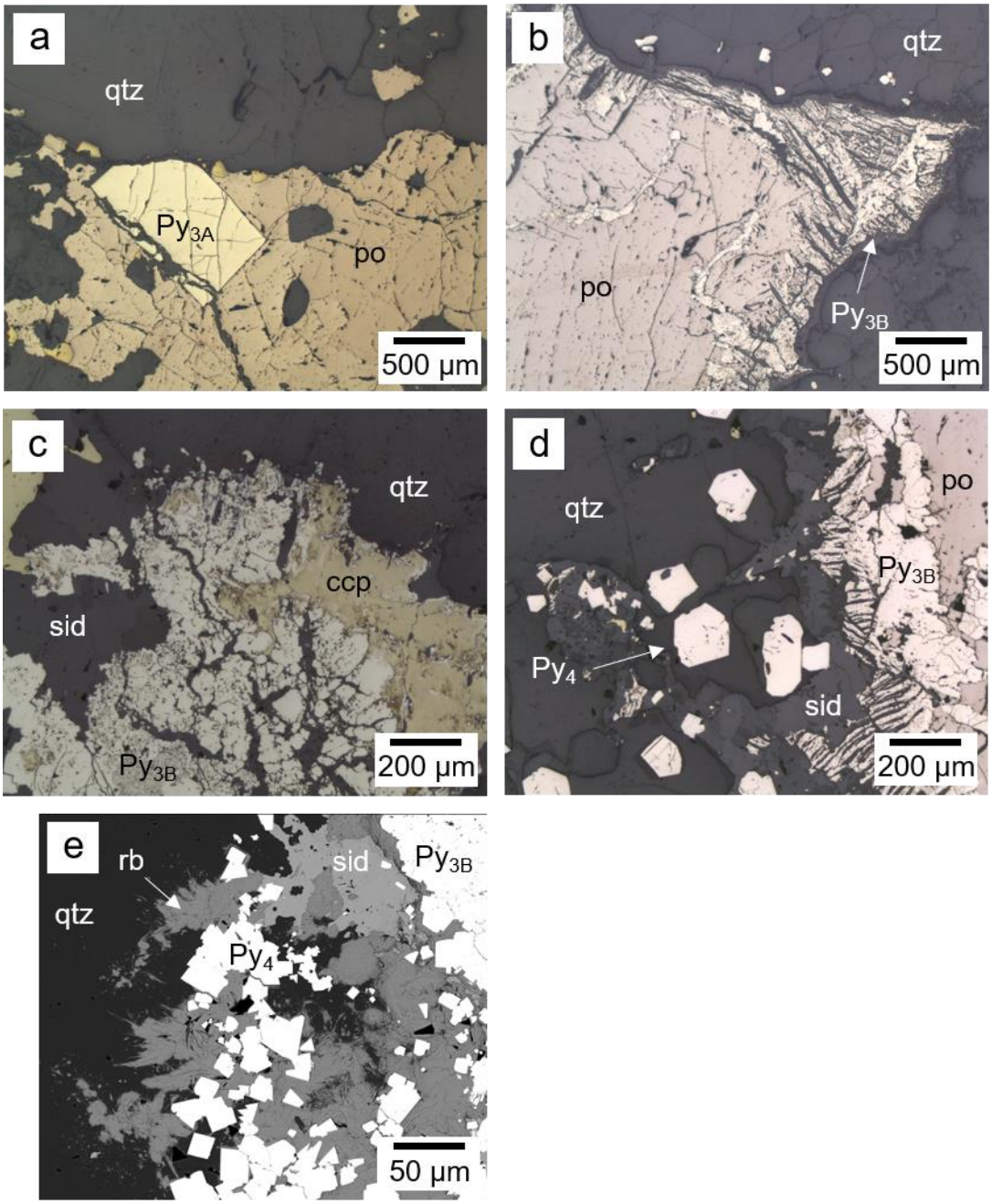

Figure 2.6 – Representative mineral assemblages and textures from D_3 shear veins. (a) Euhedral Py_{3A} enveloped by pyrrhotite. (b) Py_{3B} on the borders of pyrrhotite. (c) Replacement of Py_{3B} by chalcopyrite and siderite. (d) Replacement of Py_{3B} by siderite + Py_4 coronae. (e) Co-existence of Py_4, riebeckite, and siderite in the alteration envelope of Py_{3B}. All pictures were taken with an optical microscope except for (e), which is a BSE image.

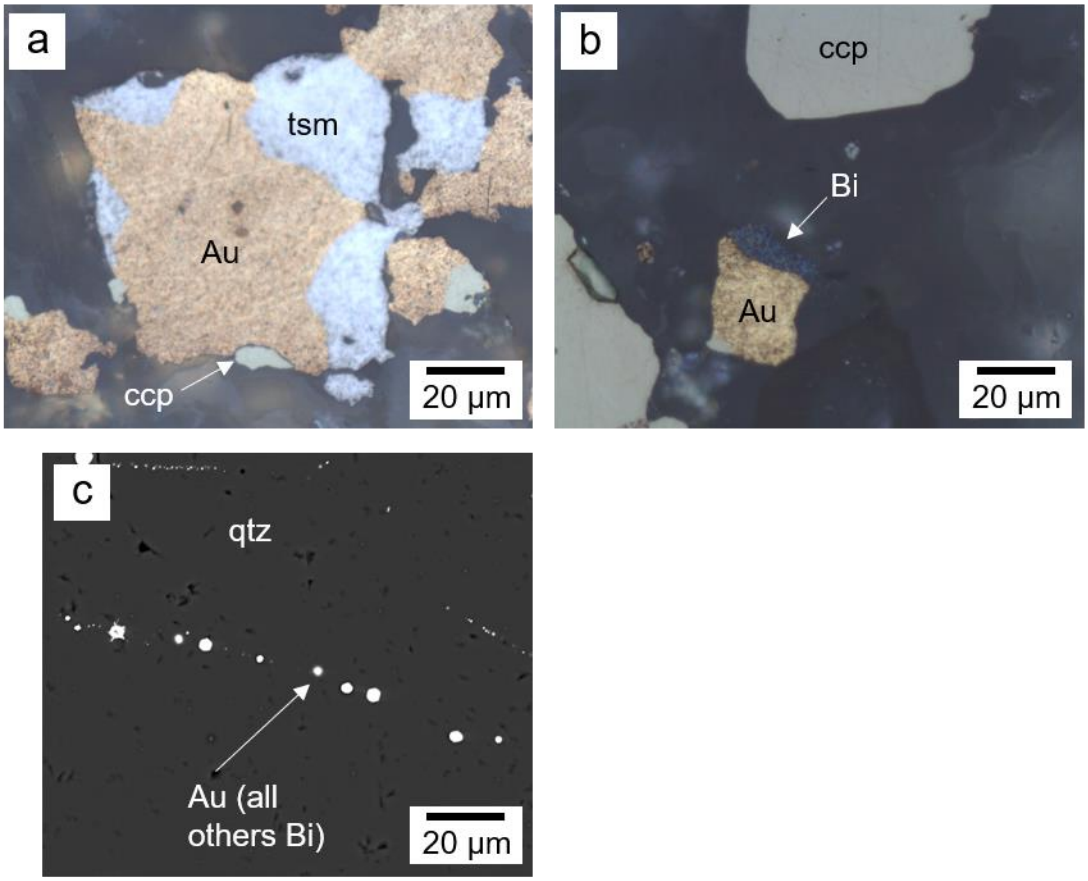

Figure 2.7 – Textural relationships in Au-Bi-Te assemblages. (a) Curvilinear boundaries between gold and tsumoite (BiTe). (b) Curvilinear boundaries between gold and bismuth. (c) A trail of globular gold and bismuth blebs along a fracture in vein quartz. (a) and (b) were taken with an optical microscope, whereas (c) is a BSE image.

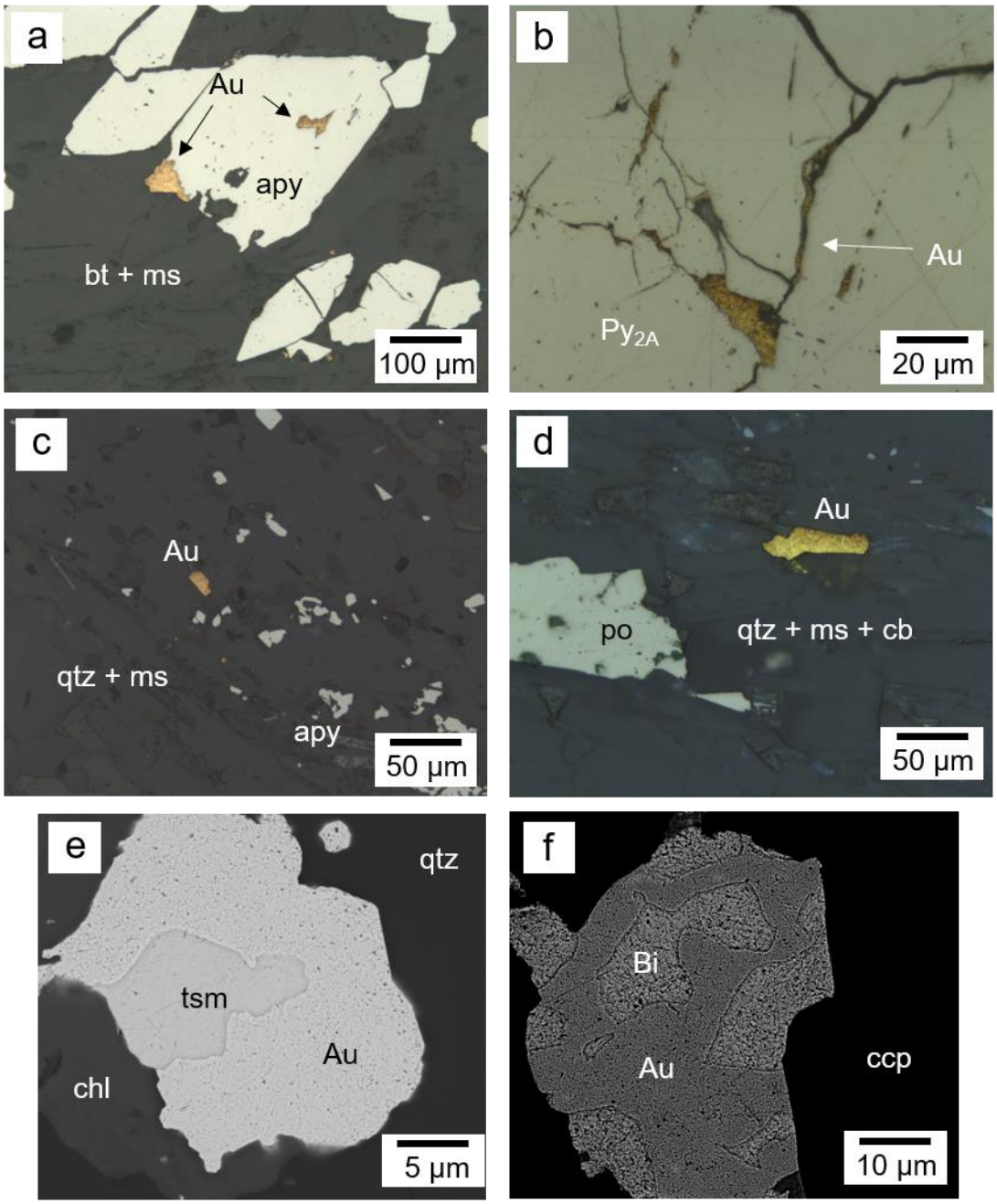

Figure 2.8 – Various textural modes of occurrence for gold in rocks from the WGC. (a, b) Gold forming along fractures and margins of arsenopyrite and Py_{2A}. (c, d) Gold isolated in the gangue minerals of D_1 and D_2 schists. (e, f) Gold associated with Bi-Te phases and chalcopyrite in veinlets cross-cutting D_3 shear veins. (a) – (d) were taken with an optical microscope, whereas (e) and (f) are BSE images.

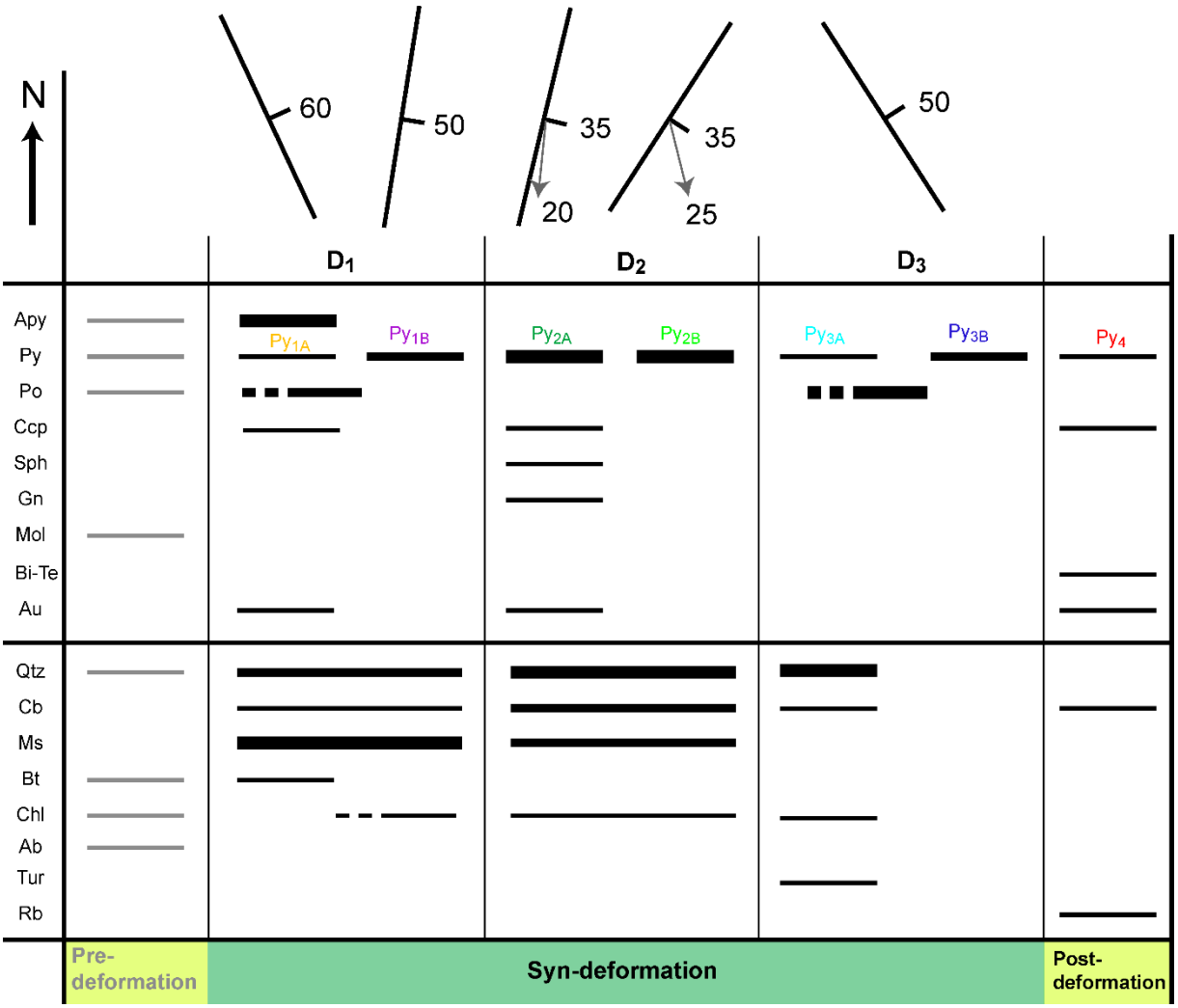

Figure 2.9 – Paragenetic diagram for the hydrothermal evolution of the WGC; note that the pre-deformation hydrothermal assemblage was not a focus of this study. The strike-dip symbols represent the dominant fabric orientation for the respective deformation event; the grey arrows represent L_2.

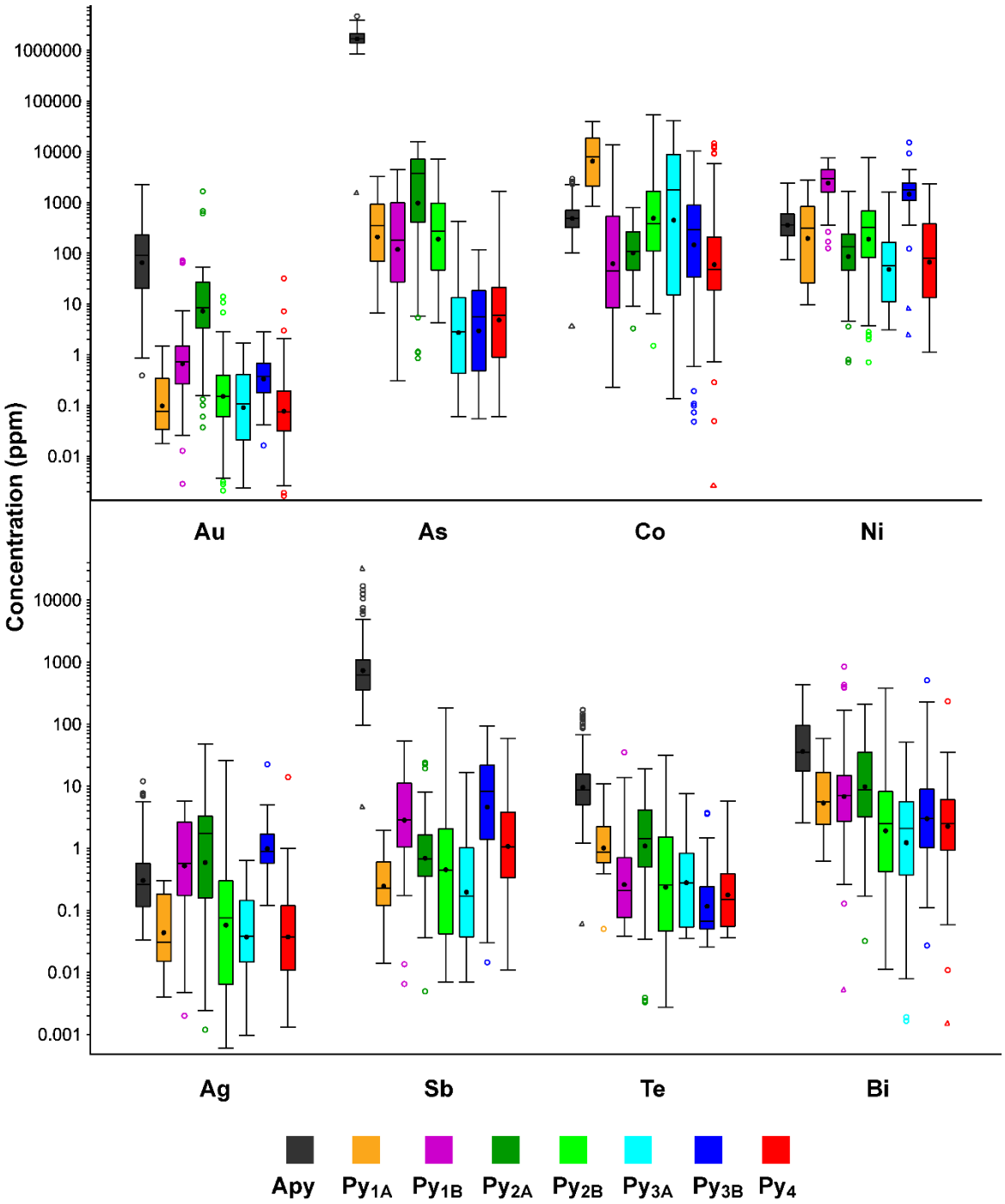

Figure 2.10 – Minor- and trace-element chemistry of arsenopyrite and pyrite in the WGC. Note the elevated Au concentrations in arsenopyrite and Py_{2A}, as well as the depleted As concentrations in Py_{3A}, Py_{3B}, and Py_4 as compared to $Py_{1A\text{-}1B}$ and $Py_{2A\text{-}2B}$.

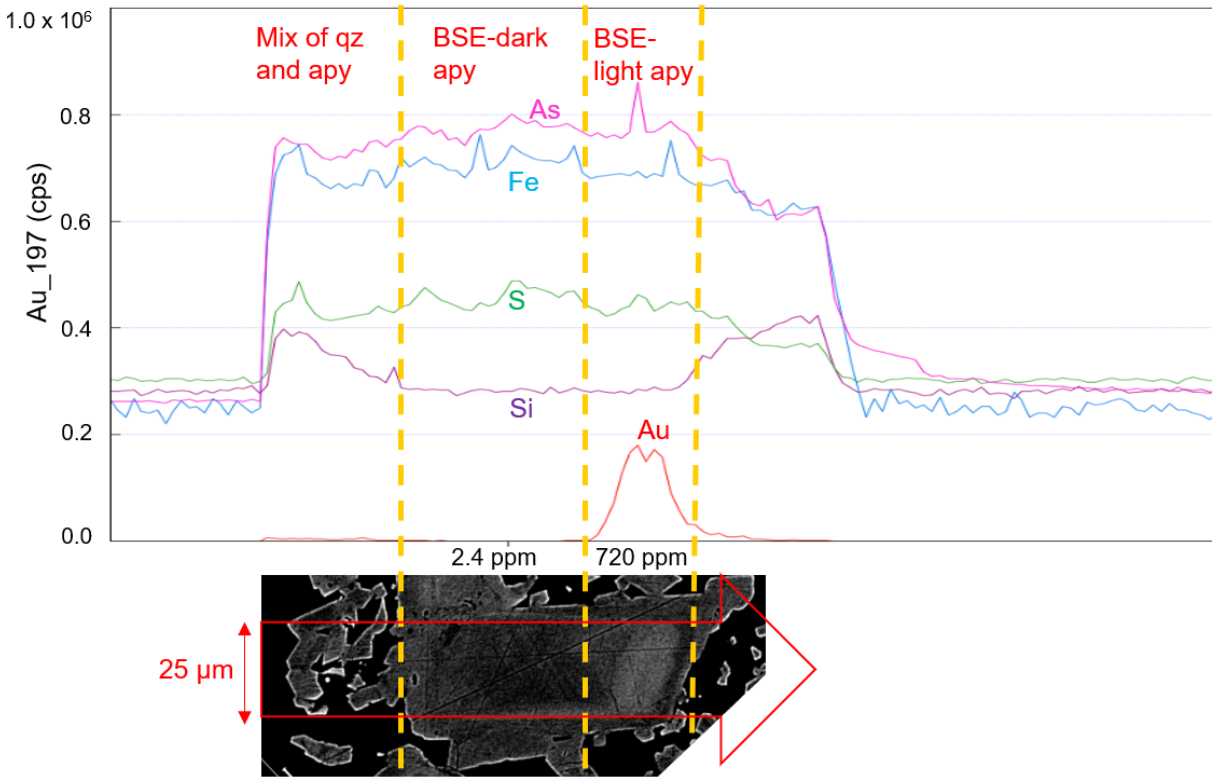

Figure 2.11 – High-contrast BSE image of arsenopyrite and associated LA transect profile (as processed using the Iolite software). The red arrow outlines the path and width of the laser, and the dashed yellow lines approximately define the zones of the grain that correlate to the different portions of the transect profile. The ppm values given above the BSE image are for Au and were derived by integrating the profile over the two regions outlined by the dashed lines. Note that the scale on the Y-axis is a linear scale for Au in counts per second and does not apply to the other elements.

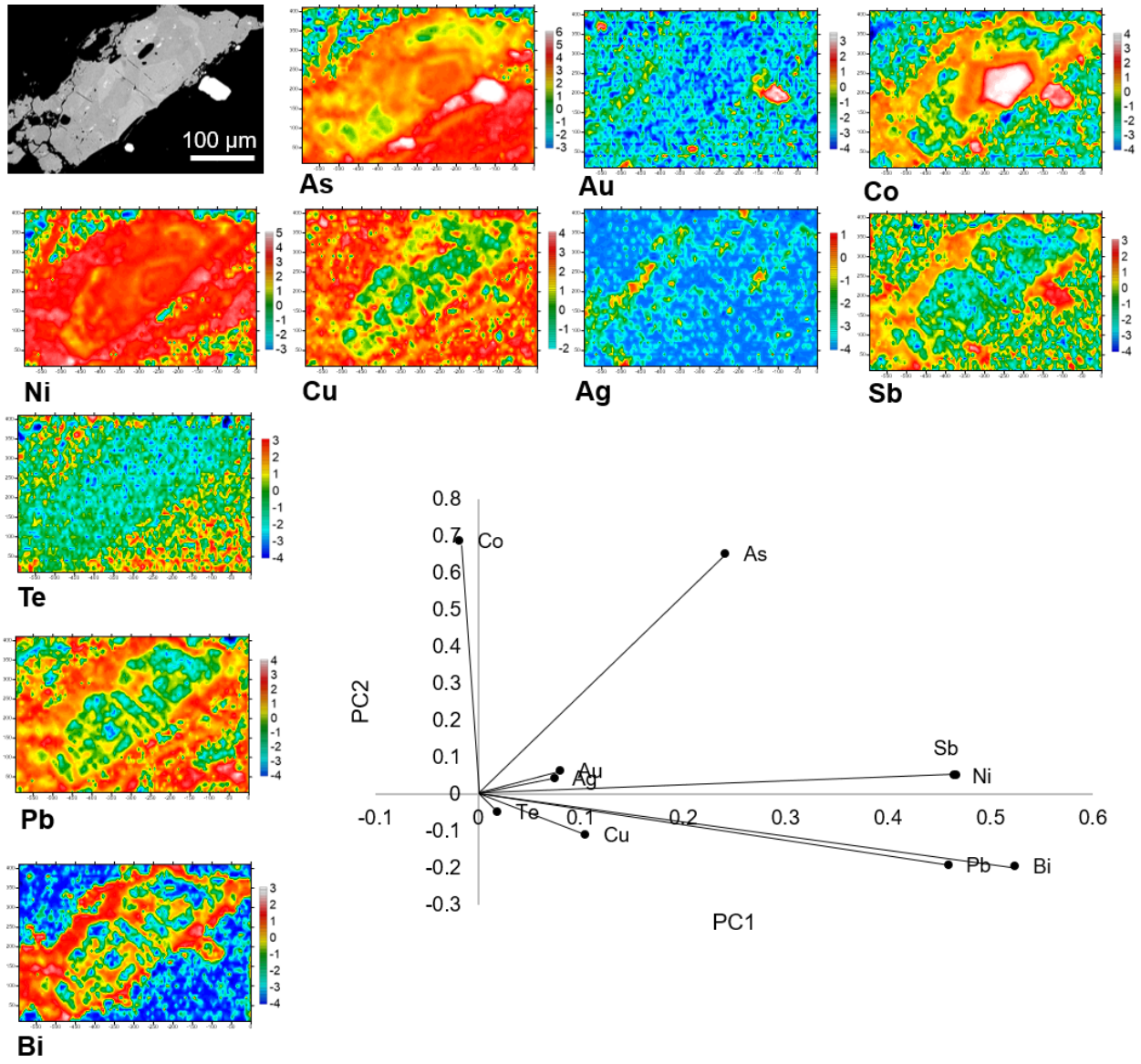

Figure 2.12 – Element distribution maps for a grain of Py_{1B} as collected by LA-ICP-MS and corresponding classical PCA analysis with log_{10} transformation. The upper left picture is a high-contrast BSE image showing the grain of Py_{1B} (grey) and two smaller grains of arsenopyrite (white). The scales show the log of concentration in ppm.

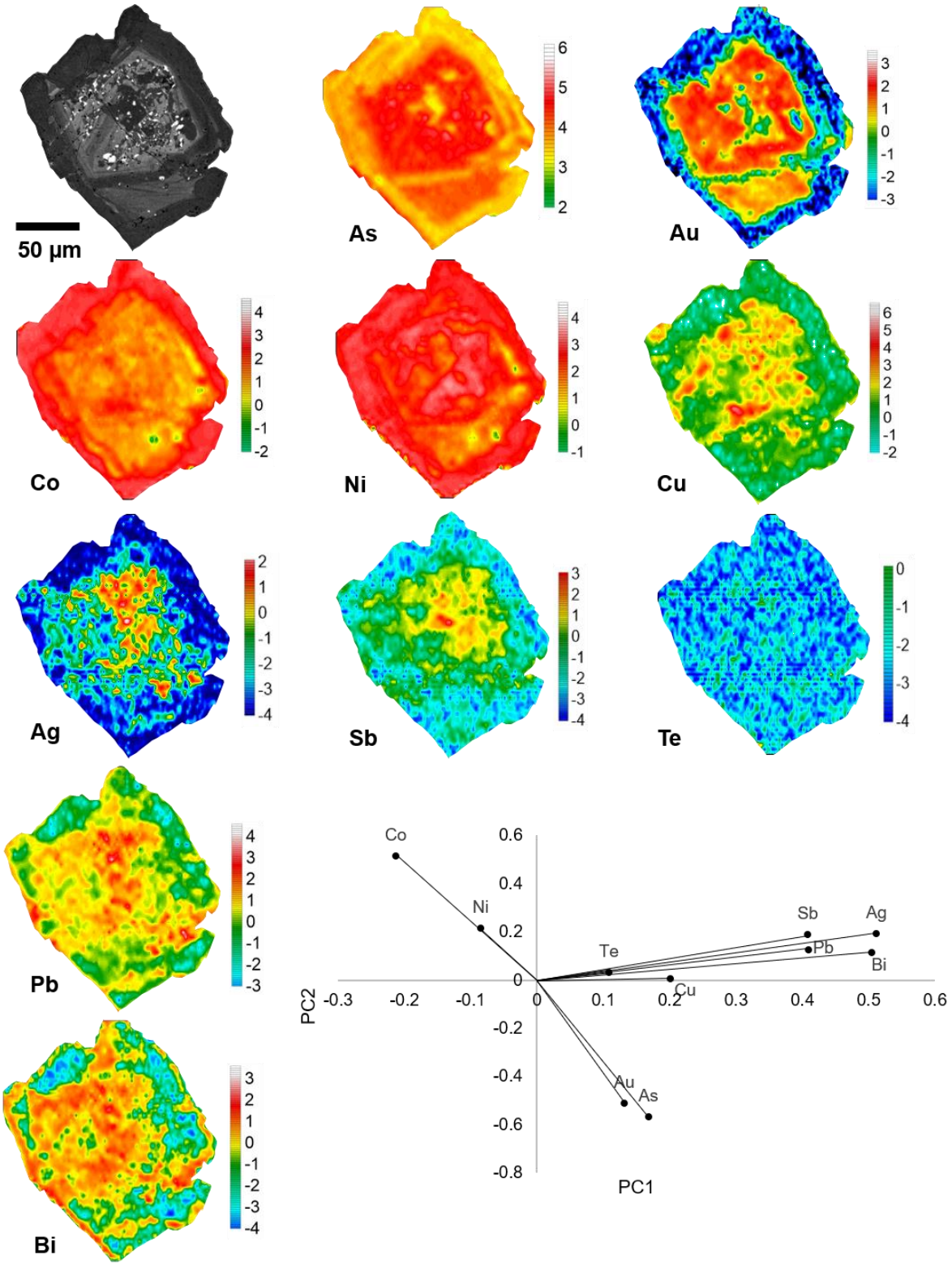

Figure 2.13 – Element distribution maps for a grain of $Py_{2A\text{-}B}$ as collected by LA-ICP-MS and corresponding classical PCA analysis with log_{10} transformation. The upper left picture is a high-contrast BSE image. The scales show the log of concentration in ppm.

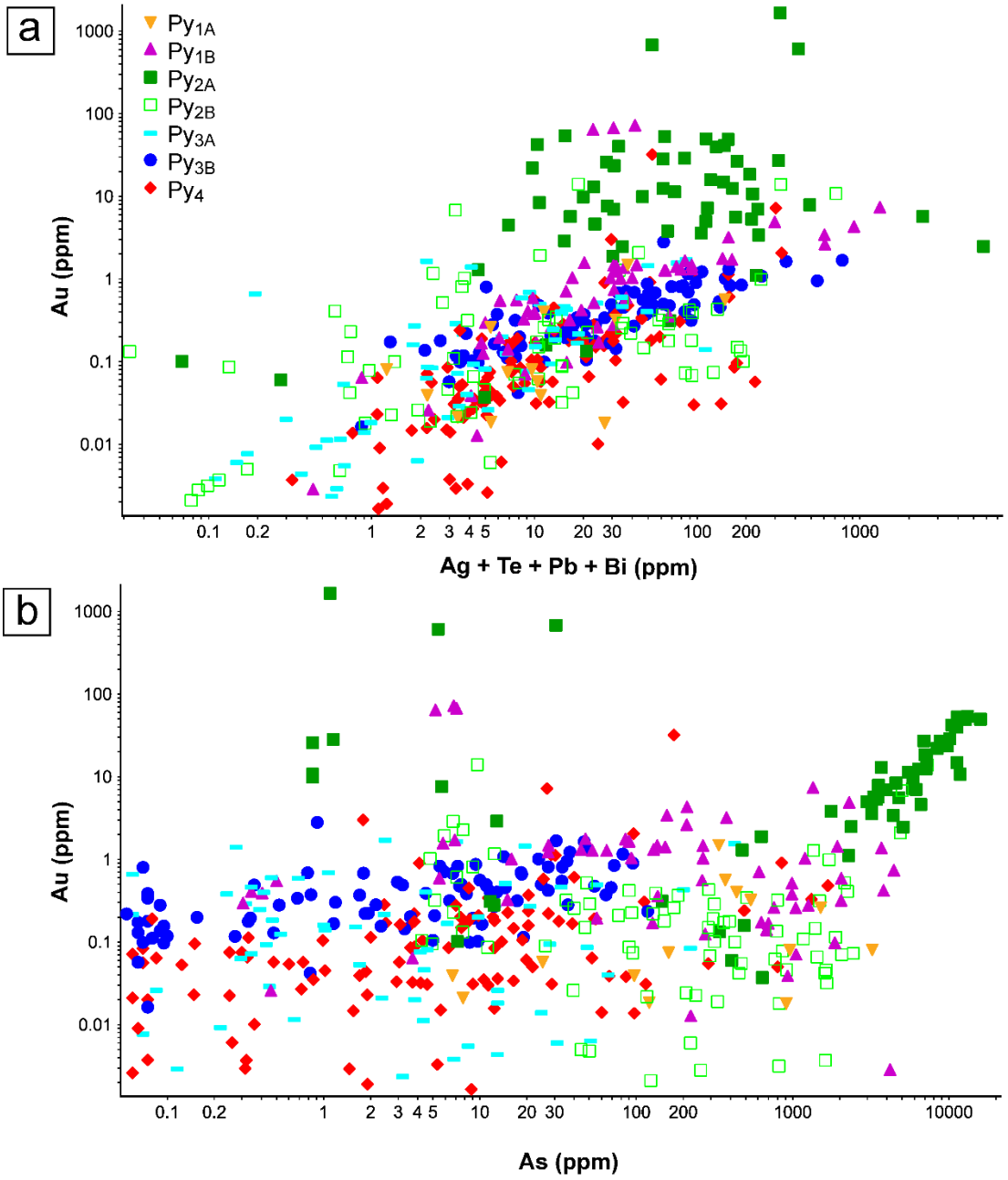

Figure 2.14 – Bivariate plot of As and the sum of LMCEs (Ag, Te, Pb, and Bi) in grains of pyrite from the WGC; warmer colours and larger grain sizes indicate greater concentrations of Au. Note that gold-enriched grains may by either enriched in As, LMCE's, or both.

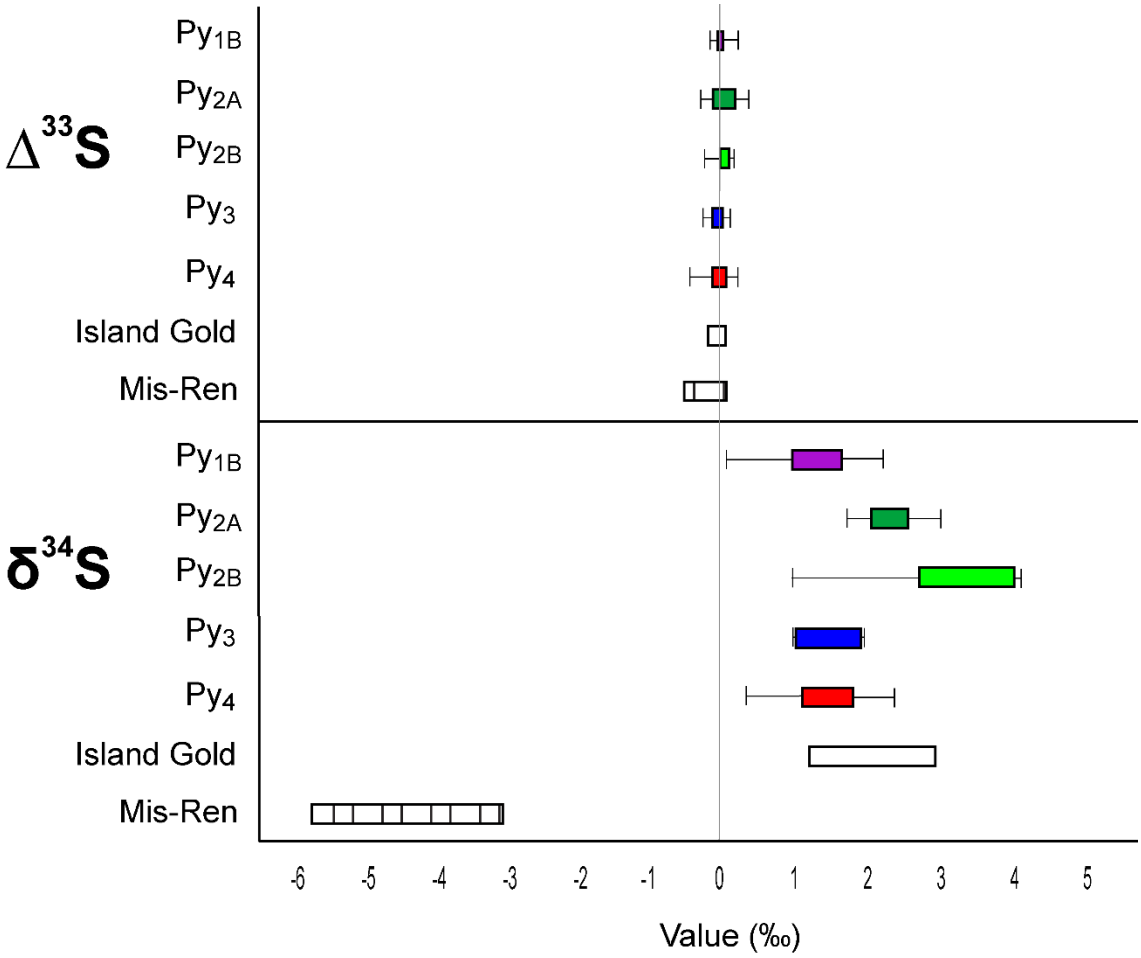

Figure 2.15 – Stable S isotope data for pyrite from the WGC. Data for the Island Gold deposit are for the ore assemblage of pyrite and pyrrhotite and are taken from Ciufo (2019) and data for the Missanabie-Renabie (Mis-Ren) deposit are for the ore assemblage of pyrite and are taken from McDivitt et al. (2020).

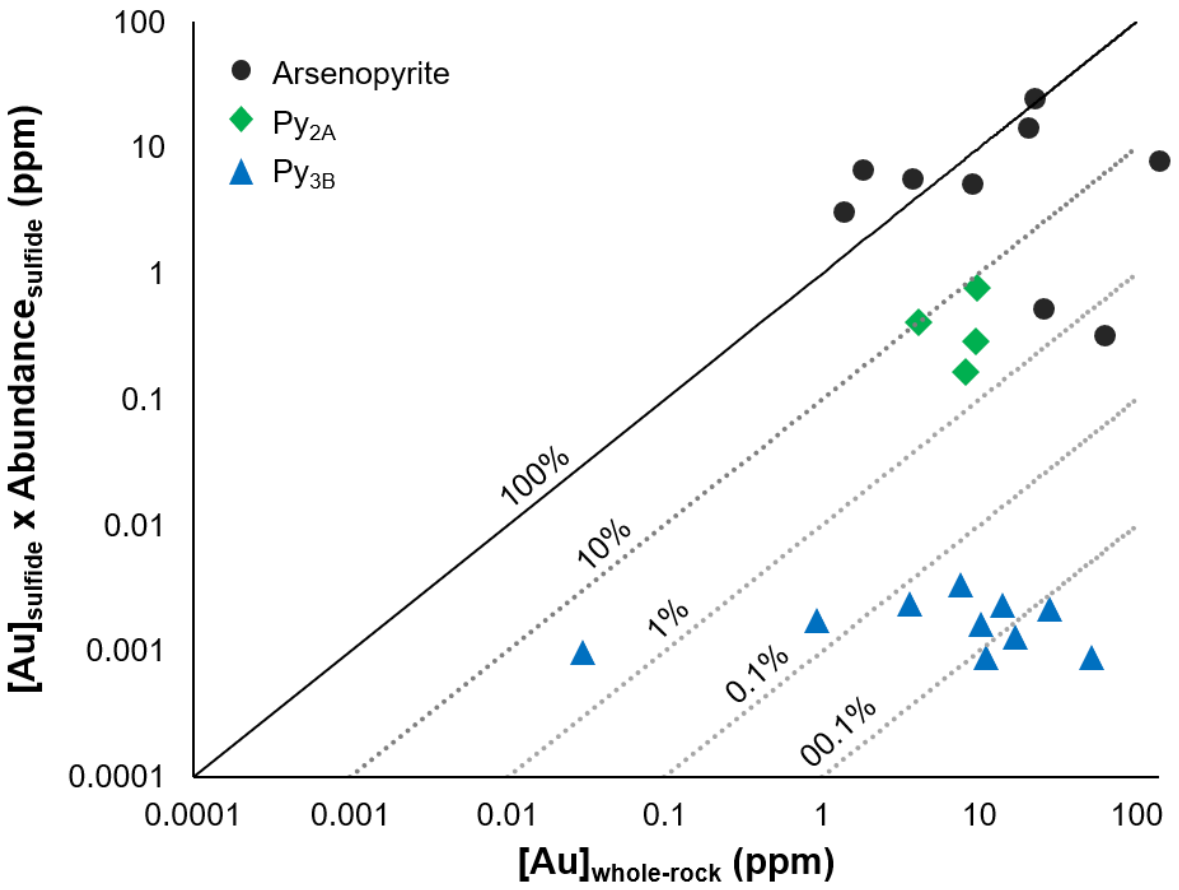

Figure 2.16 – Visualization of gold-sulfide mass-balance using a bivariate plot of the whole-rock concentration of Au and product of the concentration of Au in the dominant sulfide mineral (i.e., > 90%) and the abundance of that mineral. The lines represent the percentage of Au grade in a sample that is hosted as solid-solution Au in sulfide minerals.

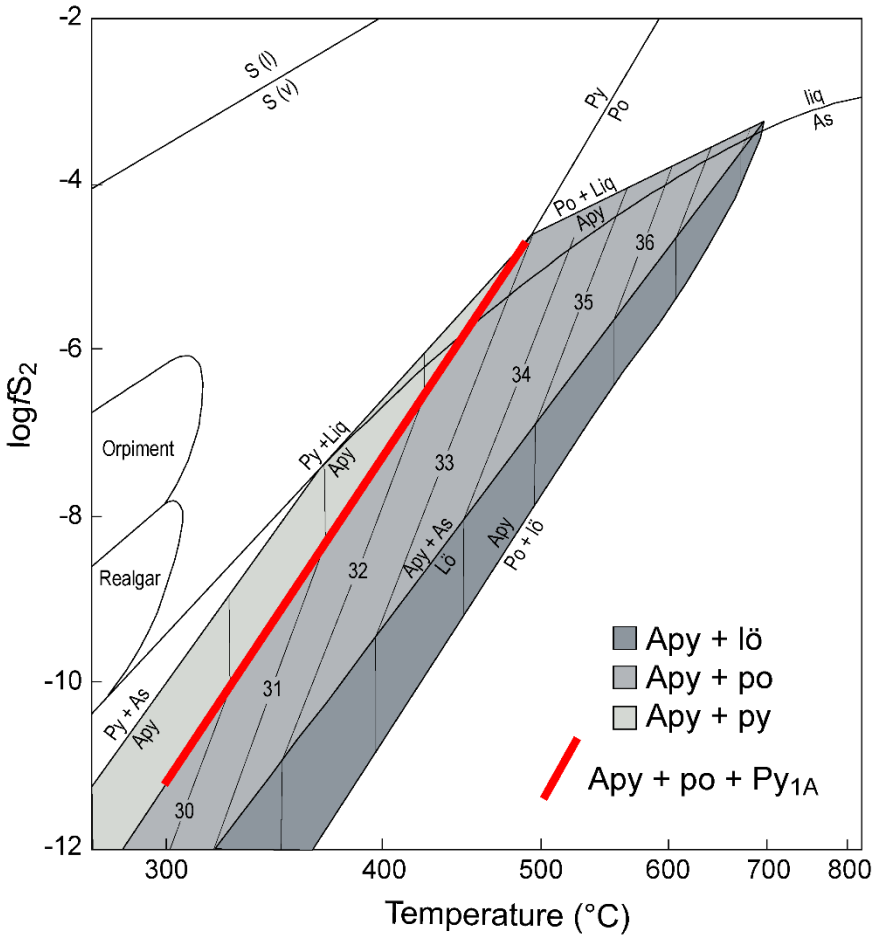

Figure 2.17 – Phase diagram of the Fe-As-S system in T-fS_2 space. The figure is modified after Morey *et al*. (2008) and based on Barton (1969) and Kretschmar and Scott (1976).

CHAPTER THREE – A CHARACTERIZATION OF AU-BI-TE(-CU) MINERALIZATION IN THE WAWA GOLD CORRIDOR AND COMMENTS ON THE ROLE OF BI-RICH POLYMETALLIC MELTS IN OROGENIC AU SYSTEMS

3.1 – Introduction

The ability of low melting point chalcophile element (LMCE; e.g., Bi, Te, Ag, Pb) polymetallic melts to partition Au from co-existing hydrothermal fluids that are Au-undersaturated (Douglas et al. 2000, Tooth et al. 2008) over ranges in temperatures similar to those of typical orogenic fluids (i.e., 200 – 400 °C) has led to the idea that polymetallic melts may play an important role in the formation of high-grade orogenic gold deposits (e.g., Ciobanu et al. 2005, Tooth et al. 2008, Tooth et al. 2011). The occurrence of Au with Bi and Te is also relevant in the context of one of the unanswered questions in the formation of orogenic gold deposits: whether the progenitor Au-bearing hydrothermal fluids were sourced from metamorphic or magmatic devolatilization (e.g., Groves et al. 2003, Tomkins 2013, Goldfarb and Groves 2015, Groves and Santosh 2016). Given the apparent similarity in the isotopic characteristics and salinities of fluids derived from these two reservoirs (Goldfarb and Groves 2015), the usefulness of the geochemical associations of gold as evidence for fluid source has been a subject of interest. In particular, mineral assemblages and mineral chemistry that reflect a Au-Bi-Te association are often taken in part as diagnostic of a magmatic-hydrothermal input of ore metals (e.g., Oberthür and Weiss 2008, Ciobanu et al. 2010, Voudouris et al. 2013, Ilmen et al. 2015, Kerr et al. 2018, Spence-Jones et al. 2018, Liu et al. 2019). Indeed, both the transport of Au in Bi-rich polymetallic melts and the association of Au with Bi and Te have been repeatedly documented in magmatic-hydrothermal environments like skarns (e.g., Cepedal et al. 2006, Cockerton and Tomkins 2012, Kolodziejczyk et al. 2015, Jiahao et al. 2016, Zhou et al. 2016), iron oxide copper-gold (IOCG) type deposits

(e.g., Kolb et al. 2010, Acosta-Góngora et al. 2015), intrusion-related gold systems (e.g., Cave et al. 2019), greisens (e.g., Guimarães et al. 2019) and porphyry-epithermal systems (e.g., Cook and Ciobanu 2004, Zhou et al. 2016, 2018). Despite the obvious relevance of polymetallic melting in orogenic deposits to discerning both the transport mechanisms for gold and potentially the source of Au-bearing fluids, an understanding of the extent to which polymetallic melting operates in these systems, and the manner in which it does so, has only recently become a subject of investigation (e.g., Oberthür and Weiss 2008, Kerr et al. 2018, Hastie et al. 2020).

The present contribution explores the above issues by evaluating Au-Bi-Te(-Cu) assemblages in the orogenic Wawa Gold Corridor (WGC) in the Archean Michipicoten greenstone belt of the Superior province, Canada. A previous study on the WGC (see Chapter Two) determined that two principal gold events occurred. The first is characterized by gold associated with arsenopyrite and pyrite, whereas the second is characterized by gold associated with Bi-Te minerals and chalcopyrite. It was suggested in Chapter Two that the second event occurred during magmatic-hydrothermal overprinting of the deposit. The WGC therefore represents an excellent environment to investigate the nature and origin of Bi-rich polymetallic melting in orogenic deposits.

3.2 – Geological context

3.2.1 – The Michipicoten greenstone belt and the Jubilee Stock

The WGC is located in the Archean Michipicoten greenstone belt (MGB), in the Wawa subprovince of the Superior province (Fig. 3.1a). It has been suggested that the MGB is a continuation of the Abitibi greenstone belt (AGB; Polat 2009), the latter being one of the best-endowed Archean gold provinces in the world (Bateman et al. 2008, Monecke et al. 2017). The

MGB is itself a growing gold district, with several active mines and exploration camps (Fig. 3.1a). A number of these have been the focus of recent research activities, including the WGC (Samson et al. 1997), the Island Gold deposit (Jellicoe 2019, Ciufo 2019), the Magino deposit (Haroldson 2014), and the Missanabie-Renabie deposit (Callan and Spooner 1998, McDivitt et al. 2017, 2018, 2020).

The MGB was formed from three periods of bimodal volcanism and intermediate to felsic plutonism, each separated by intervals of sedimentation (Turek et al. 1982), at 2890 Ma, 2750 Ma, and 2700 Ma (Turek et al. 1992). Like many of the other shear zone-hosted gold deposits in the MGB (e.g., Haroldson 2014, McDivitt et al. 2017, Jellicoe 2019, Ciufo 2019), the WGC is spatially associated with plutonic rocks, in this case the Jubilee Stock (Fig. 3.1b). This 2745 Ma intrusion (Sullivan et al. 1985) is dominated by rocks ranging from diorite to tonalite (Fig. 3.2a), with some volcaniclastic and porphyritic extrusive units (Fig. 3.2b). The Jubilee Stock was intruded by several suites of dikes, including gabbros emplaced near the end of its consolidation, Archean lamprophyres (Lefebvre et al. 2005, Stachel et al. 2006), mafic dikes belonging to the ca. 2450 Ma Matachewan dike swarm (Halls and Palmer 1990, Samson et al. 1997), and Proterozoic lamprophyres associated with the 1.0 Ga Firesand River carbonatite complex (location marked in Fig. 3.1a; Sage 1988, Symons 1989). The gabbroic dikes were of particular importance in the development of the WGC, as the contacts between these dikes and the felsic intrusive rocks of the Jubilee Stock acted as favourable planes for the development of shear zones and quartz veins (as outlined in Chapter Two; Fig. 3.2c).

In Chapter Two, it was suggested that intrusion of the Proterozoic lamprophyre dikes (Fig. 3.2d) may have been contemporaneous with the post-kinematic Au-Bi-Te event in the WGC. Identification and classification of lamprophyre dikes is often complicated by hydrothermal

alteration and metamorphism, and a rigorous documentation of these rocks was not a focus of the present study. Nevertheless, the Neoproterozoic dikes meet several of the field and mineralogical criteria for calc-alkaline lamprophyres (cf. Mathieu et al. 2018). They are small-volume intrusions, typically no more than 1-2 metres across, and contain visible phenocrysts of biotite, and possibly olivine, in a groundmass largely replaced by carbonate (Fig. 3.2e). A characteristic feature of these dikes is a blue-green alteration halo dominated by calcite and riebeckite (Fig. 3.2f).

3.2.2 – Structural evolution and metallogeny of the Wawa Gold Corridor

The following summary is based on the work described in Chapter Two, in which a more detailed history of the structural and mineralogical history of the WGC is presented. Gold mineralization in the WGC is hosted by several shear zones that formed during three principal periods of brittle-ductile deformation (D_1-D_3). The location and geometry of these zones was influenced by rheological heterogeneities within the Jubilee Stock, such as between tonalite and gabbroic dikes (e.g., Fig. 3.2c). Most of the Au mineralization formed during syn-D_1-D_2 fluid flow and occurs in NW- and NE-striking D_1-D_2 structures, where it is disseminated along with arsenopyrite and As-bearing pyrite in quartz - phyllosilicate - carbonate schists that host quartz veins (Fig. 3.3a-d). This Au originally formed as solid-solution in D_1 arsenopyrite and D_2 pyrite and was later liberated to form gold during coupled dissolution-reprecipitation reactions that affected these sulfide minerals. The Jubilee Shear Zone (JSZ), the largest Au-bearing structure on the property, is mainly characterized by D_2 deformation features (e.g., shallowly southward-plunging L_2 and NNE- and NE-striking, moderately dipping S_2) and is dominated by this style of Au mineralization. D_3 deformation formed narrow, N-NW-striking shear zones that are characterized by decimetre- to metre-scale quartz - tourmaline - carbonate shear veins (Fig. 3.3e). The D_3 shear veins are also present in earlier structures like the JSZ, where they crosscut the pre-

existing fabrics. The Minto Shear Zone (MSZ) is the principal Au-bearing D_3 structure on the property and hosts the Minto Mine South deposit (indicated + inferred resource of 100,000 oz of Au; https://redpineexp.com/projects/wawa-gold-project/). The D_3 shear veins are crosscut by post-deformation millimetre-scale carbonate ± riebeckite veinlets that host the second style of gold mineralization in the WGC, this being gold with Bi-Te phases and chalcopyrite (Fig. 3.3f).

3.3 – Methods

3.3.1 – Petrography and mineral identification

Polished thin sections were made of D_3 shear vein samples taken from the JSZ, MSZ, and adjacent host rocks. Petrographic analysis involved a combination of optical microscopy, in both transmitted and reflected light, using an Olympus BX-51 research microscope and scanning-electron microscope back-scattered electron (SEM-BSE) imaging. The identities of Bi- and Te-bearing minerals were determined with SEM energy-dispersive X-ray spectroscopy (EDS) on an FEI Quanta 200 FEG environmental SEM fitted with an EDAX EDS detector at the University of Windsor. The operating conditions included an acceleration voltage of 20.0 kV, an integration time of 30 seconds, and a spot size of 4 µm.

3.3.2 – Sulfide trace-element chemistry

The chemical composition of sulfide minerals (pyrite, arsenopyrite) was determined using laser ablation inductively coupled plasma mass-spectrometry (LA-ICP-MS). The following elements (i.e., the isotopes used) were targeted: ^{34}S, ^{57}Fe, ^{59}Co, ^{60}Ni, ^{63}Cu, ^{66}Zn, ^{75}As, ^{78}Se, ^{82}Se, ^{95}Mo, ^{98}Mo, ^{107}Ag, ^{109}Ag, ^{121}Sb, ^{130}Te, ^{184}W, ^{197}Au, ^{208}Pb, and ^{209}Bi. Several isotopes were also measured to monitor contamination from adjacent gangue minerals, these being ^{27}Al, ^{29}Si, ^{44}Ca, and ^{48}Ti. Transects across individual mineral grains were performed with a 193 nm nanosecond

Ar-F laser coupled to an Agilent 7900 quadrupole mass spectrometer, using a laser energy of 4.1 µJ and a pulse rate of 20 Hz. The beam size was 25 µm and the transect speed was 5 µm/s. Standard reference materials FeS-UQAC-1 and NIST-610 were analyzed twice each, both at the beginning of experiment and again after every 20 samples, with FeS-UQAC-1 used as the external standard. Stoichiometric Fe was used as the internal standard for both unknowns (i.e., pyrite, arsenopyrite). More detailed information about the collection and processing of LA-ICP-MS data is available in Chapter Two.

3.3.3 – Stable isotopes

The stable isotopic signature ($\delta^{13}C$ and $\delta^{18}O$) of carbonate minerals (calcite, siderite, dolomite) in the WGC were analyzed by isotope ratio mass spectrometry (IRMS). Carbonate powders prepared at the University of Windsor using a micro-drill were sent to the Jan Veizer Stable Isotope Laboratory at the University of Ottawa for analysis. Powders were reacted with phosphoric acid for 24 hours at 25.0 °C for calcite, 50 °C for dolomite, and 70 °C for siderite. Isotopic ratios were measured using a Thermo Finnigan Delta XP mass spectrometer with a Thermo Finnigan Gas Bench II system. The reference materials used were C-35-NBS-19, C-35-NBS-18, C-38-LSVEC, and an in-house standard. Analytical precision at the two-sigma level is ±0.1‰. Data for $\delta^{13}C$ are reported with respect to PDB and those for $\delta^{18}O$ are reported with respect to V-SMOW. All values are given in per mil (‰).

3.3.4 – Whole-rock geochemistry

Lithogeochemical analysis of lamprophyre dike samples was performed by ActLabs (packages Ultratrace 3, 4E ICP-MS) on submitted core samples of 10 – 30 cm length. Using a steel mill, the material was crushed to 2 mm, then pulverized to 95% less than 105 µm. Powders were

then fused with lithium metaborate and digested using a four-acid mixture. Inductively-coupled plasma spectroscopy (ICP), inductively-coupled plasma mass-spectrometry (ICP-MS) and instrumental neutron activation analysis (INAA) were used to analyze the major-, minor-, and trace-element compositions. The volatile species H_2O and CO_2 were not included in the analyses; total S was determined by ICP. The specific method used for each element, along with the detection limits, is given in Appendix E. A variety of in-house and certified reference materials were used, as well as one blank.

3.4 – Results

3.4.1 – Petrography of D_3 shear veins

As discussed in Chapter Two, a variety of types of pyrite have been recognized that are related to D_1, D_2, and D_3 veins and schists. The Bi-Te assemblages associated with Au are, however, restricted to the D_3 veins, and so it is these veins that are the focus of this chapter.

The D_3 shear veins, which host the secondary type of gold mineralization (i.e., Au-Bi-Te assemblages), are dominantly composed of granoblastic, polygonal quartz, isolated patches of coarse-grained calcite, and laminations of fine-grained tourmaline. Sulfide minerals account for less than five modal percent of veins and typically occur in contact with seams of tourmaline or inclusions of wall-rock. Pyrrhotite, the most abundant sulfide phase, is present as anhedral blebs up to a few centimetres across; rarely it envelops euhedral pyrite (Py_{3A}) and the grain boundaries between these two minerals are typically planar (Fig. 3.4a). Blebs of pyrrhotite are usually mantled and veined by anhedral pyrite (Py_{3B}; Fig. 3.4b), which is the dominant textural variety of pyrite in the veins. Siderite veinlets crosscut the shear veins and formed alteration rims around blebs of pyrrhotite + Py_{3B}, with the pyrite partially replaced by siderite and chalcopyrite (Fig. 3.4c). In some

cases, siderite in these veinlets is overprinted by interstitial calcite (Fig. 3.4d). A later stage of fine-grained, euhedral pyrite (Py_4) is hosted by the siderite that replaced Py_{3B}; notably, this pyrite generation occurs along the outer part of the siderite (Fig. 3.4e). These alteration zones are the main host for Bi-Te phases (Fig. 3.4f) and gold. Gold may occur as individual grains hosted by gangue minerals (Fig. 3.5a-d), with chalcopyrite (Fig. 3.5e-f), or with chalcopyrite and Bi-Te phases (Fig. 3.3f, Figs. 3.7, 3.8).

There are several similarities between the siderite alteration haloes that formed around sulfide blebs in the shear veins and the alteration footprint of the 1.0 Ga lamprophyre dikes that intruded the WGC, which was noted above (see Fig. 3.2d-f). Rarely, riebeckite is intergrown with siderite and Py_4 (Fig. 3.6a), an assemblage similar to the calcite + riebeckite assemblage regularly observed in the margins of the Proterozoic lamprophyre dikes (Fig. 3.6b). The carbonate veinlets that cut the shear veins (Fig. 3.6c) are also similar to veinlets adjacent to small (several to tens of cm) Proterozoic lamprophyre dikes (Fig. 3.6d).

Based on the above observations, the paragenesis of D_3 shear veins can be divided into two principal stages: (1) syn-deformation (D_3) quartz, tourmaline, calcite, Py_{3A}, pyrrhotite, and Py_{3B}; and (2) post-deformation siderite (i.e., as alteration rims on Py_{3B} and as veinlets), riebeckite, chalcopyrite, Py_4, Bi-Te minerals, gold, and calcite. During the post-deformation stage, calcite formed after the other minerals (all of which were contemporaneous).

3.4.2 – Petrography of Au-Bi-Te-bearing mineral assemblages

Assemblages of Au±Bi±Te minerals (cf. Table 3.1) are present either in the siderite-rich alteration rims around Py_{3B}, along with chalcopyrite and in some cases Py_4, or along fractures in quartz adjacent to Py_{3B}. The mineralogy of these assemblages in D_3 veins hosted in the footwall

of the JSZ ("F-JSZ assemblages") is different from those in the MSZ ("MSZ assemblages") (Table 3.1). In the footwall of the JSZ, they almost entirely comprise tsumoite (BiTe) and gold, which share curvilinear boundaries (Fig. 3.7a) and meet at ~120° triple-junctions with chalcopyrite (Fig. 3.7b, c). Tsumoite is also observed as anhedral grains that co-exist with Py_4 and siderite (Fig. 3.7d). Rarely, an unknown Bi-Te-S mineral (the empirical formula, in atomic percent, is $Bi_{36}Te_{41}S_{23}$; Table 3.1) occurs around tsumoite; the boundaries between these phases are irregular (Fig. 3.7e). The F-JSZ assemblages have bulk compositions of approximately Bi ≈ Te > Au (as inferred from the abundance of tsumoite (BiTe), relative to gold).

In contrast, the Au±Bi±Te assemblages in the MSZ are Bi-rich and mostly comprise gold, maldonite (Au_2Bi), and bismuth, with trace occurrences of jonassonite ($AuBi_5S_4$; Fig. 3.8a), tsumoite (Fig. 3.8b), ingodite ($Bi_2(S,Te)$), and bismuthinite (Bi_2S_3). Intergrowths of gold and bismuth are present (Fig. 3.8c), as are trails of globular grains of gold, maldonite, and bismuth along healed fractures in vein quartz (Fig. 3.8d). Where bismuthinite is present, it generally envelops bismuth and gold (Fig. 3.8e). In contrast to the F-JSZ assemblages, these assemblages do not share contacts with Py_4. The bulk composition of the MSZ assemblages is Bi > Au > > Te. Combining the petrographic observations made here with those in Chapter Two, a mineral paragenesis for the WGC, with emphasis on the mineral assemblages in the D_3 shear veins, is presented in Figure 3.9.

3.4.3 – Mineral chemistry

A comprehensive overview of the trace-element characteristics of various sulfide generations in the WGC was presented in Chapter Two. For the purposes of this chapter, it is important to note that: (1) the concentrations of Au, Bi, and Te in Py_{3B} and Py_4 are comparable, although Au is overall high in Py_{3B}; and (2) although Bi concentrations are similar in most

generations of pyrite and arsenopyrite, Py_{2A} and arsenopyrite in general have higher concentrations of Te than Py_{3A} and Py_{3B} (Fig. 3.10a). It is also noted that Py_{3B} has higher concentrations of Ni, and Ag than does Py_4 (cf. Chapter Two). The differences in Bi and Te concentration amongst these sulfides is also highlighted in a plot of Au versus Te/(Bi+Te) (Fig. 3.10b), which emphasizes the comparatively Te-rich nature of arsenopyrite and the Py_{1-2}. This observation is pertinent, as arsenopyrite and Py_{1-2} (in particular, Py_{2A-B}) are the most abundant sulfides in the JSZ (whereas the MSZ contains only Py_{3A-B}) and because the bulk composition of F-JSZ assemblages is different from that of MSZ assemblages.

3.4.4 – Stable isotopes of C and O

The $\delta^{18}O$ and $\delta^{13}C$ values for siderite and calcite are presented in in Appendix D. To facilitate comparison of the isotopic signatures of different carbonate minerals, the $\delta^{13}C$ and $\delta^{18}O$ values of CO_2 and H_2O, respectively, were calculated at temperatures of 250 °C and 400 °C (Fig. 3.11). The fluids associated with syn-deformation carbonate minerals, which represent most of the carbonate in the deposit, have $\delta^{13}C$ values of -0.0 to -6.0 ‰ and are characterized by two $\delta^{18}O$ populations: one between 10.0 and 16.0 ‰; and the other between -2.5 and 6.0 ‰. The fluids that correspond to post-deformation calcite in the alteration haloes of Neoproterozoic lamprophyres fall between -3.1 and -0.9 ‰ for $\delta^{13}C$ and between 2.0 and 8.3 ‰ for $\delta^{18}O$, which is different from the range of values derived from post-deformation siderite (-6.1 to -4.2 ‰ for $\delta^{13}C$, -0.6 to -5.1 ‰ for $\delta^{18}O$).

3.4.5 – Whole-rock chemistry

Lithogeochemistry for five lamprophyre dike samples is used to investigate their potential relationship to the formation of post-kinematic Au-Bi-Te assemblages in the WGC. In all cases,

concentrations of Bi and Te are below their detection limit of 0.1 ppm. The analyzed samples have similar rare-earth element (REE) profiles and display a consistent and clear enrichment in the light rare-earth elements (LREE) relative to primitive mantle (Fig. 3.12a). They are also depleted in the high field strength elements (HFSE) Nb, Ta, Zr, and Ti. Note that enrichments in LREE and depletions in HFSE are consistent with, although not diagnostic of, calc-alkaline lamprophyres (Mathieu et al. 2018). There is significant variance within the sample set with respect to Au, As, and Sb (Fig. 3.12a). In fact, a positive correlation is observed when the concentration of these elements in the lamprophyre dikes is plotted against their concentration in the host rocks adjacent to each dike (Fig. 3.12b).

3.5 – Discussion

3.5.1 – Melt assemblages vs. hydrothermal assemblages in post-deformation veinlets

The textures and identity of the gangue minerals in post-deformation veinlets (e.g., siderite, calcite, riebeckite, chlorite) and Py_4 are consistent with a hydrothermal origin. In addition, these minerals do not contain LMCE, which are the fundamental constituents of polymetallic melts. Discriminating among LMCE-bearing minerals that precipitated from a hydrothermal fluid and those that precipitated from a melt, however, requires careful textural analysis (e.g., Tomkins et al. 2004, Ciobanu et al. 2006, Cockerton and Tomkins 2012). Chalcopyrite largely formed as anhedral patches that mantle and vein Py_{3B} (Fig. 3.4c), textures consistent with the hydrothermal replacement of the latter by the former. Although textural evidence exists for the co-crystallization of chalcopyrite with other LMCE phases (e.g., 120° triple junctions with tsumoite and gold; Fig. 3.7c), this does not discount the possibility that chalcopyrite was hydrothermal. Furthermore, chalcopyrite is significantly more abundant than the associated Au-Bi-Te minerals, which would

have required melts dominated by Cu. This is considered unreasonable, given the high melting point of this element; when considering the Cu-Bi binary, for example, a melt composition of 50% Cu requires temperatures in excess of 800 °C (Chakrabarti and Laughlin 1984). As with chalcopyrite, gold occurs both in direct association with Au-Bi-Te phases and in the absence of these phases. Grains of gold belonging to the latter category have anhedral, irregular morphologies (Fig. 3.5) and, given the lack of spatial proximity to LMCE assemblages, probably did not form from melts.

Minerals belonging to F-JSZ assemblages (e.g., tsumoite, gold) display mutual curvilinear boundaries (Fig. 3.7a), a feature consistent with equilibrium crystallization from a melt (Ciobanu et al. 2006). Some MSZ assemblages contain intergrowths of bismuth and gold (Fig. 3.8b), a texture similar to those produced during Bi-Au melting experiments (Tooth et al. 2011) and observed in natural environments where melting has been invoked as the mechanism for Au-Bi transport (e.g., Ciobanu et al. 2010, Cockerton and Tomkins 2012). Globular blebs of bismuth, maldonite, and gold aligned along fractures in vein quartz (Fig. 3.8c) provide compelling evidence for transport in molten form, as their spherical morphologies are consistent with the immiscibility of the polymetallic melts in a coexisting hydrothermal fluid (e.g., Guimarães et al. 2019, Liu et al. 2019), the latter being required for precipitation of the carbonates, riebeckite, chlorite, and chalcopyrite that occur with the Au-Bi-Te assemblages. In light of these textural relationships, both the F-JSZ and MSZ LMCE assemblages are interpreted to have formed from polymetallic melts. Given the scope of this chapter, these assemblages will be the focus of the remaining discussion.

3.5.2 – Evaluating potential sources of post-deformation Au, Bi, and Te

On the basis of textural observations, the formation of Au-Bi-Te-bearing assemblages in D_3 veins could be explained as follows: (1) Py_{3B} crystallized during the formation of quartz + tourmaline + carbonate veins; (2) post-kinematic, carbonic fluids dissolved Py_{3B}, thereby liberating Au, Bi, and Te, and precipitated siderite; and (3) the aforementioned liberated elements were mobilized on a local (i.e., centimetre) scale in the form of Bi-rich polymetallic melts to form the now observed Bi-Te-Au-S bearing phases, bismuth, and gold.

The role of secondary processes in liberating Au and other metals from the paragenetically early pyrite (or arsenopyrite), as suggested here, has been proposed by previous authors, who suggested hydrothermal alteration (e.g., Morey et al. 2008, Lawley et al. 2017, Kerr et al. 2018, Hastie et al. 2020) and metamorphism (e.g., Large et al. 2009, Dubosq et al. 2018) as potential mechanisms for the reconstitution of Au-bearing sulfides or sulfarsenides and the related expulsion of trace metals. Such processes have also been interpreted to have been coupled with the generation of Bi-Te-rich polymetallic melts (e.g., Kerr et al. 2018, Hastie et al. 2020). Although the liberation of metals from pyrite may in part be identified by differences in pyrite trace-element chemistry, it is equally important to consider the volume of primary pyrite that was recrystallized or dissolved and to compare that to the volume of secondary pyrite that was formed. This consideration is crucial in the case of the WGC pyrite, given that the generations of pyrite that occur in proximity to Bi-Te-Au-bearing mineral assemblages, Py_{3B} and Py_4, have similar concentrations of Au, Bi, and Te (Fig. 3.10a). A mass-balance analysis was employed to this effect, based on a comparison of the mass of an element released during Py_{3B} dissolution and the total mass of that element in a given assay interval (approximately one metre):

$$\%E_{Py3B} = \frac{(C_{Py3B})(V_{sid})(D_{py})}{(C_{WR})(V_{WR})(D_{WR})} \times 100\% \quad \text{[Equation 3.1]}$$

where *%E* is the percent contribution from Py_{3B} of an element by mass, *C* is the concentration of an element in ppm, *V* is the modal volume of a phase as a percentage of the assay interval, *D* is the density of the material, and *WR* stands for "whole-rock". It is assumed that the replacement of Py_{3B} by siderite was a constant-volume process. The average of C_{Py3B} over a given assay interval was used with a range of values in V_{sid} to assess the amount of Py_{3B} dissolution required to account for whole-rock enrichment in each element. This calculation (Fig. 3.13) indicates that even if D_3 veins were originally 50% Py_{3B} by volume, the loss of pyrite could only account for the mass of Au, Bi, and Te present in low-grade samples. In addition, if such high initial volumes of Py_{3B} were present, it would be expected that relicts of massive sulfide would be preserved in some veins, which is not the case. In fact, petrographic observations suggest that no more than 1-2% of Py_{3B} by modal volume was lost during replacement by siderite. This means that pyrite dissolution likely accounted for no more than one percent of the present masses of Au, Bi, and Te in the D_3 veins (blue dots in Fig. 3.13). Thus, a model in which Bi-rich polymetallic melts formed adjacent to pyrite grains commensurate with liberation of trace metals during replacement of Py_{3B} is not valid for the D_3 vein systems in the WGC. The elimination of this hypothesis means that significant amounts of Au, Bi, and Te were already present in the post-deformation fluids that transgressed the D_3 veins when Py_{3B} was dissolved, such that the origin and evolution of these fluids requires examination.

Whereas carbonates and chlorite are ubiquitous in the WGC, it is noteworthy that riebeckite, which is atypical of Archean lode gold deposits, is present in the veinlets hosting the Au-Bi-Te-bearing mineral assemblages (e.g., Fig. 3.6a). As already noted, the only other

environment in the WGC in which riebeckite formed is in the alteration haloes of the 1.0 Ga lamprophyre dikes intruding the deposit (Fig. 3.2d, f, Fig. 3.6b), where it is abundant. The carbonate-rich stringers that originate from these dikes (Fig. 3.6d) crosscut the matrix of the D_3 veins in a manner similar to those that occur with the Au-Bi-Te- bearing minerals (Fig. 3.6c). Based on these mineralogical and textural similarities, the formation of gold, Bi-Te-S-bearing minerals, and chalcopyrite was likely associated with the 1.0 Ga lamprophyre event. There are two hypotheses: (1) the lamprophyre event added Au, Bi, and Te to the WGC; and (2) the lamprophyre event and associated hydrothermal system were responsible for the redistribution of these elements from earlier stages of Au + sulfide mineralization throughout the deposit.

Hypothesis 1 mimics a model promoted several decades ago wherein lamprophyric magmas were considered as plausible sources of Au in orogenic systems due to their formation in the mantle and spatial association with some orogenic gold deposits (e.g., Rock and Groves 1988, Rock et al. 1989). In light of a growing body of geochemical data, this model was largely discarded and the co-occurrence of lamprophyre dikes with orogenic deposits was related to the exploitation of similar crustal structures by both hydrothermal fluids and lamprophyric magmas (e.g., Wyman and Kerrich 1988, Kerrich and Wyman 1994, Ashley et al. 1994, Taylor et al. 1994, Muller and Groves 2019). The time discordance between shear zone formation (ca. 2,700 – 2,600 Ma; Jellicoe 2019) and lamprophyre emplacement in the WGC means that the lamprophyre magmas did not exploit active structures, but instead relate to later crustal failure (i.e., to the formation of the 1.0 Ga Firesand River carbonatite complex; Sage 1988, Symons 1989). In addition, Au, Bi and Te have very low concentrations in the analyzed whole-rock samples; Au does not exceed eight ppb and neither Bi nor Te are above the detection limit of 0.1 ppm, which is consistent with the general character of lamprophyres (e.g., Kerrich and Wyman 1994). Furthermore, Neoproterozoic

lamprophyre dikes are found throughout the Jubilee Stock, but Au-Bi-Te assemblages are only present where these dikes crosscut previously mineralized zones. Thus, it is unlikely that the lamprophyric magmas introduced substantial amounts of Au, Bi, and Te to the system. This leaves a model in which the dike event was responsible for the redistribution of pre-existing metal enrichments. Although the analyzed lamprophyres all have similar REE patterns, significant variance is observed amongst the samples with respect to Au, As, and Sb (Fig. 3.12a), which are often enriched in orogenic systems (Goldfarb and Groves 2015). The positive correlation between Au, As, and Sb concentrations in the lamprophyres and their adjacent host rocks (Fig. 3.12b) is consistent with some degree of assimilation of schist during the emplacement of lamprophyre magmas. Had Bi and Te been detected, it is reasonable to assume they would also have displayed this correlation. Ashley et al. (1994) proposed a similar explanation for Au, As, Sb, and Bi enrichment in lamprophyre dikes cutting mesothermal gold mineralization in Hillgrove, Australia. The dikes themselves are pervasively carbonatized (Fig. 3.2e), which is consistent with the migration of fluids associated with the 1.0 Ga event along the same structures that the dikes exploited. The isotopic characteristics of the post-deformation fluids, as derived from siderite, overlap with the signature of syn-deformation carbonate minerals, whereas they are different from the fluid signature derived from the calcite associated with the lamprophyres (Fig. 3.11). Thus, it is possible that the heat associated with dike emplacement may have driven the circulation of pre-existing fluids in the deposit, or that the fluids from the lamprophyre event inherited the signature of carbonate in the deposit prior to the precipitation of siderite in D_3 veins. Regardless of their source, the fluids may have dissolved some arsenopyrite and Py_{2A}, both of which contain more Au and Te and similar concentrations of Bi than Py_{3B}. Although the relative contributions of fluids

from the 1.0 event vs. intra-deposit circulation remains equivocal, the 1.0 Ga lamprophyre event is considered to have driven the mobilization of Au, Bi, and Te as Bi-rich polymetallic melts.

3.5.3 – Physicochemical conditions of melt formation and evolution

3.5.3.1 – Comparison of F-JSZ and MSZ assemblages

The Au-Bi-Te-bearing assemblages in the WGC are divided into two categories based on their mineralogy: F-JSZ assemblages dominated by tsumoite and gold with rare occurrence of an unknown Bi-Te-S mineral; and MSZ assemblages dominated by bismuth, gold, and maldonite with minor jonassonite, tsumoite, ingodite, and bismuthinite. In both groups, the latest phase is a relatively S-rich mineral that post-dates relatively S-poor minerals (e.g., the unknown Bi-Te-S mineral after tsumoite and bismuthinite after bismuth; Fig. 3.7f and Fig. 3.8d, respectively). Although both groups are interpreted to have precipitated from polymetallic melts, their distinct mineralogical character indicates different bulk compositions, with F-JSZ assemblages having Bi ≈ Te > Au and MSZ assemblages having Bi > Au >> Te.

Despite the variance in mineralogy and melt compositions, there is no obvious discrepancy in timing of formation of the two groups of assemblages with respect to the deposit paragenesis; both occur with chalcopyrite on the margins of pyrite + pyrrhotite blebs in post-deformation carbonate ± riebeckite ± chlorite veinlets that crosscut D_3 veins. Assuming that prior to melt mobilization most of the Bi and Te was hosted in sulfides (e.g., pyrite, arsenopyrite), the composition of these minerals provides a reasonable proxy for the availability of Bi and Te in each environment. The dominant sulfides in the JSZ (arsenopyrite, $Py_{2A\text{-}B}$) are comparatively richer in Te (Fig. 3.10b) than those in the MSZ. Given that the F-JSZ assemblages occur outside of the JSZ itself, it is also possible that pre-deformation sulfide mineralization in the footwall of the JSZ (see

Chapter Two) was an important reservoir of Bi and Te. The hydrothermal fluids that co-existed with the polymetallic melts were likely responsible for the redistribution of Au, Bi, and Te within the deposit, rather than the introduction of these elements to the deposit, and so it is probable that the differences in composition between F-JSZ and MSZ assemblages largely reflect the bulk chemistry of the local environment in which they formed.

The relative proportions of Bi to Te, S, and Se in minerals composed of these elements have been used to interpret the redox state of the system at the time of their crystallization (e.g., Ciobanu and Cook 2002, Cook and Ciobanu 2004, Ciobanu et al. 2005, Ciobanu et al. 2010). Minerals with Bi ≤ (Te+Se+S) form under relatively oxidizing conditions (pyrite-stable), whereas those with Bi ≥ (Te+Se+S) form under relatively reducing conditions (pyrrhotite-stable). Tsumoite (BiTe) may form under both relatively oxidizing and relatively reducing conditions (Ciobanu et al. 2005). In the WGC, F-JSZ assemblages (e.g., tsumoite and the Bi-Te-S mineral; BiTe and Bi_2Te_2S, respectively) have stoichiometries with Bi ≤ (Te+Se+S), whereas MSZ assemblages (e.g., bismuth, maldonite, jonassonite, ingodite; Bi, Au_2Bi, $AuBi_5S_4$, and Bi_2TeS, respectively) have stoichiometries with Bi ≥ (Te+Se+S). Potential intra-deposit variations in parameters that affect oxidizing-reducing conditions (e.g., fO_2, fS_2, fTe_2) must therefore be considered for a model that accounts for the genesis, evolution, and distribution of the Au-Bi-Te-bearing assemblages.

3.5.3.2 – Evolution of the system during the replacement of pyrite by siderite

Whether they occur in the footwall of the JSZ or the MSZ, Au-Bi-Te minerals consistently have a spatial proximity (i.e., within a few centimetres) to blebs of Py_{3B} and pyrrhotite in D_3 veins with siderite and, in some cases, Py_4. The grain boundaries between siderite and Py_{3B} are irregular (Fig. 3.4c, e, f) and are interpreted to represent the replacement of Py_{3B} by siderite. Mass-balance calculations preclude sourcing of Au, Bi, and Te exclusively from the dissolution of Py_{3B} via its

replacement by siderite and so another mechanism is required to explain the generation of these melts. Both experimental studies (e.g., Tooth et al. 2011) and those of natural samples (e.g., Cockerton and Tomkins 2012, Wang et al. 2019) highlight the importance of chemical reactions at mineral-fluid interfaces in mediating physiochemical conditions that can affect the stability of polymetallic melts. Based on this, and given the intimate association between Au-Bi-Te assemblages and siderite that replaced Py_{3B}, an evaluation of the pyrite-siderite reaction is warranted.

The architecture of the siderite + Py_4 coronae after Py_{3B} is typified by the presence of Py_4 in the exterior part of the siderite rim and its absence in the interior part of the siderite rim, as is displayed in Figure 4e. In assessing this reaction, the following assumptions are made: (1) the siderite + Py_4 coronae represent the original extent of Py_{3B}; and (2) the fluids that precipitated siderite and Py_4 first encountered Py_{3B} at its exterior and progressed towards its interior. In this context, the relative distributions of Py_{3B}, Py_4, and siderite and their textural relationships can be used as a temporal proxy for the progression of the replacement reaction. The following stages, as shown in Figure 3.14, are used to illustrate this evolution (note that "system" is defined as the interface between the fluid and bleb of Py_{3B}): T_0, when Py_{3B} exists with quartz prior to fluid infiltration (Fig. 3.14a); T_1, when fluid influx begins and the reaction commences at the edge of Py_{3B} to form euhedra of Py_4 with siderite (Fig. 3.14b); T_2, during which fluid flux increases, the reaction interface progresses towards the interior of Py_{3B} and siderite is formed without Py_4 (Fig. 3.14c); and T_3, during which fluid influx decreases and replacement eventually ceases (Fig. 3.14d).

These stages can be further described in the context of chemical reactions that represent the replacement of Py_{3B} by siderite. The following theoretical reaction is used to describe T_1:

$$2FeS_2\ (Py_{3B}) + HCO_3^- + H^+ \rightarrow FeS_2\ (Py_4) + FeCO_3 + 2HS^-\quad \text{[Reaction 3.1]}$$

Reaction 3.1 is not balanced with respect to the valences of the elements involved, as one of the S atoms in pyrite requires two electrons to form aqueous bisulfide. There are several candidates for reducing agents (e.g., CH_4, Fe^{2+}), but these were not incorporated given the absence of direct constraints on fluid chemistry. Note that HCO_3^- and H^+ are aqueous species introduced to the system by the hydrothermal fluid derived from or having interacted with the lamprophyric dikes. During T_1 (Fig. 3.14b), the fluid flux was relatively low and euhedral grains of Py_4 crystallized with siderite, suggesting chemical equilibrium. Py_{3B}, however, was not stable during this time. This may have related to differences in the trace-element compositions of Py_{3B} and Py_4, which are known to affect the relative stabilities of minerals of the same species (cf. Putnis and Austrheim 2013). As fluid influx continued (T_2; Fig. 3.14c), allowing an increased availability of HCO_3^-, neither type of pyrite was stable. Siderite therefore precipitated without Py_4, as can be illustrated by the following theoretical reaction:

$$FeS_2\ (Py_{3B}) + HCO_3^- + H^+ \rightarrow FeCO_3 + 2HS^- \text{ [Reaction 3.2]}$$

As with Reaction 3.1, Reaction 3.2 is unbalanced with respect to reduction-oxidation. As fluid flux diminished, the availability of HCO_3^- would have decreased and the reaction would have eventually ceased.

3.5.3.3 – The precipitation and mediation of melts at pyrite-siderite reaction interfaces

A model for polymetallic melt formation can be established by combining petrographic observations of the F-JSZ and MSZ assemblages with the geochemical data for these shear zones, the influence of redox conditions on Bi-Te mineral stability, and paragenesis of mineral replacement reactions and melt crystallization.

During T_1, pyrite was stable as Py_4. F-JSZ assemblages coexist with Py_4 and siderite (Fig. 3.7c) and these minerals have Bi ≤ (Te+Se+S). In contrast, minerals of the MSZ assemblages, with Bi ≥ (Te+Se+S), should not stably coexist with pyrite (Ciobanu et al. 2005) and indeed these minerals are not seen with Py_4. It is likely therefore that the relatively Te-rich character of the fluids that migrated through the JSZ or the footwall of the JSZ stabilized melts with a bulk composition of Bi ≈ Te > Au, which precipitated during T_1. In contrast, the relatively Te-poor character of fluids in the MSZ prevented precipitation of polymetallic melts during T_1. During T_2, an increased fluid flux may have removed S from the system, consistent with neither Py_{3B} nor Py_4 being stable, which relates to the lack of Py_4 in the interior part of the siderite domain. Under conditions of lower fS_2, melts with a bulk composition of Bi > Au >> Te would have been stabilized and able to form the MSZ assemblages. The transition of Reaction 3.1 from pyrite-stable to pyrite-unstable was not necessarily coincident with the destabilization of polymetallic melts in the footwall of the JSZ, as melts with an equal proportion of Bi and Te (i.e., tsumoite) can exist under both relatively oxidizing and relatively reducing conditions (Ciobanu et al. 2005). During T_3, the waning influx of hydrothermal fluids may have reduced the amount of S that was transported out of the system during pyrite dissolution. Although pyrite did not precipitate during T_3, the occurrence of bismuthinite after bismuth in the MSZ (Fig. 3.8d) and of the Bi-Te-S mineral after tsumoite in the footwall of the JSZ (Fig. 3.7f) point to progressive elevation in fS_2. The transition from bismuth to bismuthinite could also have been the product of a decrease in temperature (Fig. 3.15), which would be consistent with lower input of hydrothermal fluids (these being the source of heat in the system).

An elusive piece of the puzzle is the direct effect, if any, of the pyrite-siderite replacement reaction on the conversion of aqueous Bi^{3+}, which is the most likely oxidation state for aqueous Bi

(Tooth et al. 2013), to molten Bi^0. The potential conversion of aqueous Te^{2-}, which is the most likely oxidation state for Te in mesothermal systems (Zhang and Spry 1994), to molten Te^0 must also be considered. There is, however, no evidence of changes in the oxidation states of any of the other species in the system. It is quite possible that relatively reduced aqueous species participated in the reaction (were oxidized) without precipitating a phase that directly records their presence. An obvious contender is methane, which has been documented in several populations of fluid inclusions in the WGC (Samson et al. 1997) and contains reduced C that could have been oxidized to form siderite. A hypothetical reaction based on this is proposed below:

$$2Bi(OH)_{3(aq)} + CH_{4(aq)} + FeS_2\ (Py_{3B}) \rightarrow 2Bi_{(l)} + FeCO_3 + 2H_2S_{(aq)} + 3H_2O \quad \text{[Reaction 3.3]}$$

It is also possible that some Fe^{2+} from pyrite was oxidized to form Fe^{3+}, which was not incorporated into a solid phase. The $\delta^{34}S$ signatures of Py_{3B} and Py_4 are similar (cf. Chapter Two), suggesting that there was insignificant, if any, oxidation of the S in pyrite to form SO_4^{2-} during this reaction. If the chemical reaction involving the reduction of aqueous Bi^{3+} comprised exclusively aqueous species, it can be posited that the pyrite-siderite reaction front simply facilitated conditions favourable to the formation of melts. This concept has been demonstrated by the experimental work of Tooth et al. (2011), who noted that mineral-fluid and mineral-mineral reactions can provide catalytic surfaces, porosity, and relatively reducing conditions (e.g., lower fS_2), all of which promote the precipitation of Bi-rich polymetallic melts. Once formed, the polymetallic melts, regardless of whether Bi ≈ Te > Au or Bi > Au >> Te, would have effectively scavenged Au from the co-existing hydrothermal fluids and subsequently precipitated gold.

3.5.4 – Implications for the role of the "liquid Bi collector model" in orogenic gold systems

An apparent consistency in orogenic or shear zone-hosted lode gold deposits where gold has in part been attributed to crystallization from Bi-rich melts is the formation of these melt assemblages after the crystallization of Fe or Fe-As sulfides (e.g., Oberthür and Weiser 2008, Ciobanu et al. 2010, Voudouris et al. 2013, Ilmen et al. 2015, Brando Soares et al. 2018, Kerr et al. 2018, Hastie et al. 2020). In some deposits, paragenetically earlier sulfides were the source of Au for later Bi-rich melts (e.g., Oberthür and Weiser 2008, Kerr et al. 2018, Hastie et al. 2020), whereas in other settings no direct link is made between early sulfide mineralization and later precipitation of gold and LMCE minerals from a melt phase. In the latter case, input of new metals is typically attributed to a magmatic source (e.g., Ciobanu et al. 2010, Voudouris et al. 2013, Ilmen et al. 2015). Regardless of the model, there is a decoupling of primary gold mineralization from polymetallic melt formation. Furthermore, for the second model, the melt event is separated from the primary hydrothermal Fe-sulfide mineralization that typifies orogenic systems (Groves et al. 1998). The commonality of such a paragenesis (i.e., the formation of polymetallic melts after primary Au + sulfide mineralization) points towards one or more basic controls of the formation and stability (or lack thereof) of Bi-rich melts in orogenic environments.

Exsolution of molten Bi from a hydrothermal fluid and partitioning of Au into the melt requires: (1) temperatures above the melting point of Bi (271 °C; Douglas et al. 2000); and (2) relatively reducing conditions (i.e., low fS_2, fTe_2, fO_2; Tooth et al. 2008, Tooth et al. 2011). The first criterion typifies orogenic fluids, the temperatures of which often exceed 300 °C (Ridley and Diamond 2000, Goldfarb et al. 2005, Shao et al. 2018). When evaluating the second criterion, the dominance of pyrite in most orogenic deposits is noted (Groves et al. 1998, Goldfarb et al. 2005), which reflects relatively oxidizing conditions (e.g., fS_2; Fig. 3.15) above the stability for molten

Bi (Ciobanu et al. 2005). The transport of Au in polymetallic melts under pyrite-stable conditions is possible if the melts are Te-rich, which is consistent with the character of the JSZ assemblages in the WGC and with observations of melt-generated minerals with Bi ≤ (Te+Se+S) in other deposits (e.g., Cook and Ciobanu 2004, Oberthür and Weiser 2008). For Te-poor, Bi-rich melts, the relatively oxidizing nature of orogenic hydrothermal fluids (in comparison to the stability of native Bi; Ciobanu et al. 2005, Cockerton and Tomkins 2012) precludes the formation of Bi melts and is probably an important part of the explanation for why Au-Bi-Te assemblages typically post-date sulfide (i.e., pyrite) mineralization in these systems.

A second line of reasoning to explain why the transport of Au in Bi-rich melts post-dates formation of Fe(-As) sulfide assemblages in orogenic settings relates to how pre-existing sulfide minerals can promote melt formation. Consider for example the "sponge" model proposed by Lawley et al. (2017) whereby hydrothermal Au partitions into arsenian pyrite or arsenopyrite during their crystallization. These authors considered this as a necessary first step in the generation of native gold via dissolution of Au-bearing Fe-sulfarsenides and reprecipitation of Au-poor equivalent phases, a concept supported in other studies (e.g., Morey et al. 2008, Large et al. 2009, Cook et al. 2013, Velásquez et al. 2014, Kouhestani et al. 2017, Neyedley et al. 2017, Gourcerol et al. 2018, 2020**,** Kerr et al. 2018, Shao et al. 2018, Hastie et al. 2020), including this work on the WGC (see Chapter Two). In fact, both of these sulfide minerals can also accommodate Bi and Te as trace metals (e.g., Morey et al. 2008, Cook et al. 2009b, Keith et al. 2018, Mathieu 2019), which could contribute to the formation of polymetallic melts during sulfide dissolution and the subsequent migration of melts containing Au and LMCEs (e.g., Kerr et al. 2018, Hastie et al. 2020). The formation of Bi-Te-bearing sulfide minerals may therefore be an important precursor to Bi-rich melt formation in a manner that is similar to that proposed for the generation of gold

during sulfide CDR reactions (cf. Lawley et al. 2017). In the WGC, mass-balance calculations discount the possibility that Bi-rich melts resulted solely from the liberation of Au, Bi, and Te from adjacent pyrite; nevertheless, a consistent spatial association between pyrite and Au-Bi-Te assemblages exists. As described previously, this relates to the potential role of the sulfide blebs in providing a locally reducing environment or catalytic surface (e.g., Tooth et al. 2011, Zhou et al. 2017, Wang et al. 2019). The proximity of sulfide minerals and crystallized melt assemblages has also been related to the role of the former in providing dilational micro-environments, such as pores or fractures, in which melt migration and crystallization was facilitated (e.g., Ciobanu et al. 2006, Wang et al. 2019).

Whether due to the instability of native Bi in most orogenic fluids (due to elevated fO_2 as reflected by the ubiquity of pyrite in these systems) or the necessity of pre-existing sulfides to act as a source of elements or of favourable physiochemical sites for melt precipitation, the liquid Bi collector model appears to have operated as a mechanism for gold upgrading and redistribution in orogenic deposits (e.g., Oberthür and Weiser 2008, Kerr et al. 2018, Hastie et al. 2020), rather than as a model for primary Au mineralization. Interestingly, Au-Bi-Te melt assemblages are often described as having formed after Fe-sulfides (e.g., pyrite, arsenopyrite, pyrrhotite, chalcopyrite) and Fe-oxides (e.g., magnetite) in gold deposits that have not been classified as orogenic (e.g., Ciobanu et al. 2006, Zheng et al. 2015, Liu et al. 2019, Wang et al. 2019), including magmatic-hydrothermal environments such as IOCG-like deposits (Kolb et al. 2010, Acosta-Gongora et al. 2015), skarns (Cepedal et al. 2006), VMS deposits (Törmänen and Koski 2005, Belogub et al. 2011), RIRG deposits (Cave et al. 2019) and porphyry-epithermal systems (Cook and Ciobanu et al. 2004, Mikulski 2005). It is therefore possible that the arguments presented here to explain this relationship in orogenic systems are applicable to other Au-mineralized environments as well.

3.5.5 – Using element associations to identify magmatic-hydrothermal contributions of Au

The two Au events that formed the WGC are distinguishable in terms of their geochemistry, mineralogy, and structural and paragenetic relationships. The first comprises disseminated and solid-solution Au in syn-deformation arsenopyrite and As-bearing pyrite in quartz + phyllosilicate + carbonate schists, whereas the second comprises post-deformation gold hosted in carbonate ± riebeckite ± chlorite veinlets along with Bi-Te-Au minerals and chalcopyrite. The Au-Bi-Te(-Cu) association that defines the latter event is one that is often taken as evidence for a magmatic-hydrothermal source of Au-mineralizing fluids (e.g., Ciobanu et al. 2010, Voudouris et al. 2013, Ilmen et al. 2015, Brando Soares et al. 2018, Zhou et al. 2018, Spence-Jones et al. 2018, Kerr et al. 2018, Mathieu 2019, Wang et al. 2019, Liu et al. 2019). As demonstrated above, the hydrothermal fluids associated with the second, post-kinematic Au event are related to the emplacement of 1.0 Ga lamprophyric magmas (Sage 1988, Symons 1989) and occurred >1.5 Ga after the first gold event. Whole-rock geochemical data, however, preclude the possibility that the lamprophyres added significant quantities of Au, Bi, and Te to the deposit, and are instead compatible with a model in which the lamprophyres were responsible for fluid circulation and mobilization of pre-existing Au, Bi, and Te. Such a model is consistent with the findings of previous workers who documented a lack of elevated concentrations of Au, Bi, and Te in lamprophyric magmas (e.g., Kerrich and Wyman 1994, Muller and Groves 2019) and the observation that, despite the ubiquity of these lamprophyric dikes throughout the Jubilee stock, Au-Bi-Te mineralization occurs only where these lamprophyres crosscut zones of previous metal endowment.

The fact that magmatic-hydrothermal fluids transgress orogenic deposits, either prior to, during, or after deformation, is not contentious; instead, the relevant question is whether they

introduce nontrivial quantities of Au to such systems. To this end, it is important to establish that even if magmatic-hydrothermal fluids introduced Bi and Te (the two pathfinder elements typically used to invoke a magmatic source) to an orogenic deposit, this does not necessarily indicate that such fluids were Au-bearing. The WGC is an example of how magmatic-hydrothermal fluids can overprint an orogenic deposit and form Au-Bi-Te mineral assemblages without contributing these elements, in particular Au, to the system. The distinction between mobilization of existing gold and introduction of new gold is paramount, particularly when considering the aforementioned point that when Au-Bi-Te assemblages are observed in orogenic deposits, they typically post-date Au-As mineralization (e.g., Oberthür and Weiser 2008, Ciobanu et al. 2010, Voudouris et al. 2013, Ilmen et al. 2015, Brando Soares et al. 2018, Kerr et al. 2018, Hastie et al. 2020). An understanding of the timing of magmatic-hydrothermal fluid input with respect to existing Au mineralization, of the source of the magmatic-hydrothermal fluids and its potential to produce Au-enriched fluids, and of the nature and magnitude of existing Au mineralization is necessary in order to discriminate between these two scenarios (i.e., mobilization vs. introduction). Identification of a magmatic-hydrothermal contribution of Au based solely on a Au-Bi-Te(-Cu) association is strongly cautioned.

3.6 – Conclusions

1. The formation of Bi-Te-Au polymetallic melts in the WGC was the product of deposit-scale mobilization of these elements out of earlier sulfides related to fluid circulation driven by intrusion of Neoproterozoic (1.0 Ga) lamprophyre dikes. Melt composition was fundamentally controlled by the geochemical environment in which they formed (i.e., the footwall of the relatively Te-rich JSZ vs. the relatively Te-poor MSZ) and their

precipitation and evolution was mediated by chemical reactions at fluid-mineral interfaces (i.e., the pyrite-siderite reaction front).

2. The paragenetic relationship of the two Au mineralizing events in the WGC, these being an early syn-kinematic Au-As event and a later post-kinematic Au-Bi-Te event, seems to be shared by many orogenic gold deposits in which polymetallic melt generation is documented. The apparent consistency with which Bi-rich melting postdates primary Fe-sulfide + Au-As mineralization probably relates to the relatively oxidized nature of the hydrothermal fluids that form these deposits (above the stability field of Bi) and the role of pre-existing sulfide mineralization in acting both as a potential source of Au and LMCEs and as favourable micro-environments for melt formation. The liquid-Bi collector model is evidently important in the upgrading of pre-existing gold mineralization but is probably not a feasible mechanism for the initial precipitation of gold in orogenic systems.

3. The association of Au with LMCEs, such as Bi and Te, is used as evidence for a magmatic-hydrothermal source of these metals. Despite the importance of post-kinematic fluids in the formation of Au-Bi-Te assemblages in the WGC, it is unlikely that these fluids introduced significant amounts of Au, Bi, and Te to the deposit. The WGC is an important example therefore of how barren fluids may result in a Au-LMCE association, thus highlighting the importance of discriminating between the mobilization of existing gold and the addition of new gold. This intricacy is fundamental to resolving the sources of Au-bearing fluids that form orogenic deposits.

3.7 – References

Acosta-Góngora, P., Gleeson, S.A., Samson, I.M., Ootes, L., and Corriveau, L., 2015, Gold Refining by Bismuth Melts in the Iron Oxide-Dominated NICO Au-Co-Bi (±Cu±W) Deposit, NWT, Canada: Economic Geology, v. 110, p. 291-314.

Ashley, P.M., Cook, N.D.J., Hill, R.L., and Kent, A.J.R., 1994, Shoshonitic lamprophyre dykes and their relation to mesothermal Au-Sb veins at Hillgrove, New South Wales, Australia: Lithos, v. 32, 249-272.

Barton, P.B.J., and Skinner, B.J., 1979, Sulfide mineral stabilities, *in* Barnes, H.L., ed., Geochemistry of hydrothermal ore deposits, 2nd edition: Pennsylvania, Wiley-Interscience, p. 278–403.

Bateman, R., Ayer, J.A., and Dubé, B., 2008, The Timmins-Porcupine Gold Camp, Ontario: Anatomy of an Archean Greestone Belt and Ontogeny of Gold Mineralization: Economic Geology, v. 103, p. 1285-1308.

Belogub, E.V., Moloshag, V.P., Novoselov, K.A., and Kotlyarov, V.A., 2011, Native Bismuth, Tsumoite, and Pb-Bearing Tsumoite from the Tarn'er Copper-Zinc Massive Sulfide Deposit, Northern Urals: Geology of Ore Deposits, v. 53(8), 798-805.

Brando Soares, M., Neto, A.V.C., Bertolino, L.C., Alves, F.E.A., de Almeida, A.M., da Silva, P.H.M., de Araújo Mabub, R.O., Manduca, L.G., de Pamplona Araújo, I.M.C., 2018, Multistage mineralization at the hypozonal São Sebastião gold deposit, Pitangui greenstone belt, Minas Gerais, Brazil: Ore Geology Reviews, v. 102, p. 618-638.

Callan, N.J., and Spooner, E.T.C., Repetitive hydraulic fracturing and shear zone inflation in an Archean granitoid-hosted, ribbon banded, Au-quartz vein system, Renabie area, Ontario, Canada: Ore Geology Reviews, v. 12, p. 237-266.

Cave, B.J., Barnes, S.-J., Pitcairn, I.K., Sack, P.J., Kuikka, H., Johnson, S.C., and Duran, C.J., 2019, Multi-stage precipitation and redistribution of gold, and its collection by lead-bismuth and lead immiscible liquids in a reduced-intrusion related gold system (RIRGS); Dublin Gulch, western Canada: Ore Geology Reviews, v. 106, 28-55.

Cepedal, A., Fuertes-Fuente, M., Martín-Izard, A., González-Nistal, S., and Rodríguez-Pevida, L., 2006, Tellurides, selenides and Bi-mineral assemblages from the Río Narcea Gold Belt, Asturias, Spain: genetic implications in Cu-Au and Au skarns: Mineralogy and Petrology, v. 87, p. 277-304.

Chakrabarti, D.J., and Laughlin, D.E., 1984, The Bi-Cu (Bismuth-Copper) System: Bulletin of Alloy Phase Diagrams, v. 5(2), p. 148-155.

Ciobanu, C.L., and Cook, N.J., 2002, Tellurides, selenides (and Bi-sulphosalts) in gold deposits. 11th IAGOD Symp-Geocongress, CD vol, Geological Survey of Namibia.

Ciobanu, C.L., Cook, N.J., and Pring, A., 2005, Bismuth tellurides as gold scavengers, *in* Mao, J.W., Bierlein, F.P. (*eds*), Mineral Deposit Research: Meeting the Global Challenge. Springer, Berlin, p. 1383-1386.

Ciobanu, C.L., Cook, N.J., Damian, F., and Damina, G., 2006, Gold scavenged by bismuth melts: An example from Alpine shear-remobilizates in the Highiş Massif, Romania: Mineralogy and Petrology, v. 87, p. 351-384.

Ciobanu, C.L., Birch, W.D., Cook, N.J., Pring, A., and Grundler, P.V., 2010, Petrogenetic significance and Au-Bi-Te-S associations: The example of Maldon, Central Victorian gold province, Australia: Lithos, v. 116, p. 1-17.

Cockerton, A.B.D, and Tomkins, A.G., 2012, Insights into the Liquid Bismuth Collector Model Through Analysis of the Bi-Au Stormont Skarn Prospect, Northwest Tasmania: Economic Geology, v. 107, 667-682.

Cook, N.J., and Ciobanu, C.L., 2004, Bismuth tellurides and sulphosalts from the Larga hydrothermal system, Metaliferi Mts., Romania: Paragenesis and genetic significance: Mineralogical Magazine, v. 68(2), p. 301-321.

Cook, N. J., Ciobanu, C.L., and Mao, J., 2009b, Textural control on gold distribution in As-free pyrite from the Dongping, Huangtuliang and Hougou gold deposits, North China Craton (Hebei Province, China): Chemical Geology, v. 204, p. 101-121.

Cook, N.J., Ciobanu, C.L., Meria, D., Silcock, D., and Wade, B., 2013, Arsenopyrite-Pyrite Association in an Orogenic Gold Ore: Tracing Mineralization History from Textures and Trace Elements: Economic Geology, v. 108, p. 1273-1283.

Ciufo, T.J., 2019, Hydrothermal Alteration and Exploration Vectors at the Island Gold Deposit, Michipicoten Greenstone Belt, Wawa, Ontario: Unpublished M.Sc. thesis, Waterloo, University of Waterloo, 523 p.

Douglas, N., Mavrogenes, J., Hack, A., and England, R., 2000, The liquid bismuth collector model: An alternative gold deposition mechanism, *in* Skilbeck, C.G., and Hubble, T.C.T., eds., Understanding planet Earth; searching for a sustainable future; on the starting blocks of the third millennium: Australian Geological Convention, 15th, Sydney, Abstracts: Sydney, Geological Society of Australia, 135 p.

Dubosq, R., Lawley, C.J.M., Rogowitz, A., Schneider, D.A., and Jackson, S., 2018, Pyrite deformation and connections to gold mobility: Insight from micro-structural analysis and trace element mapping: Lithos, v. 310-311, p. 86-104.

Goldfarb, R.J., Baker, T., Dubé, B., Groves, D.I., Hart, C.J.R., and Gosselin, P., 2005, Distribution, character, and genesis of gold deposits in metamorphic terranes: Economic Geology 100th Anniversary Volume, p. 407–450.

Goldfarb, R.J., and Groves, D.I., 2015, Orogenic gold: Common or evolving fluid and metal sources through time: Lithos, v. 233, 2-26.

Golyshev, S.I, Padalko, N.L., and Penchenkin, S.A., 1981, Fractionation of stable oxygen and carbon isotopes in carbonate systems: Geochemistry International, v. 18, p. 85-99.

Gourcerol, B., Kontak, D.J., Thurston, P.C., and Petrus, J.A., 2018, Results of LA-ICP-MS sulfide mapping from Algoma-type BIF gold systems with implications for the nature of mineralizing fluids, metal sources, and deposit models: Mineralium Deposita, v. 53, p. 871-894.

Gourcerol, B., Kontak, D.J., Petrus, J.A., and Thurston, P.C., 2020, Application of LA ICP-MS analysis of arsenopyrite to gold metallogeny of the Meguma Terrane, Nova Scotia, Canada: Gondwana Research, v. 81, p. 265-290.

Groves, D.I., Goldfarb, R.J., Gebre-Mariam, M., Hagemann, S.G., and Robert, F., 1998, Orogenic gold deposits: A proposed classification in the context of their crustal distribution and relationship to other gold deposit types: Ore Geology Reviews, v. 13, p. 7-27.

Groves, D.I., and Santosh, M., 2016, The giant Jiaodong gold province: The key to a unified model for orogenic gold deposits?: Geoscience Frontiers, v. 7(3), p. 409-417.

Guimarães, F.S., Cabral, A.R., Lehmann, B., Rios, F.J., Ávila, M.A.B., de Castro, M.P., and Queiroga, G.N., 2019, Bismuth-melt trails trapped in cassiterite-quartz veins: Terra Nova, v. 31, p. 358-365.

Halls, H.C., and Palmer, H.C., 1990, The tectonic relationship of two Early Proterozoic dyke swarms to the Kapuskasing Structural Zone: a paleomagnetic and petrographic study: Canadian Journal of Earth Sciences, v. 27, p. 87-103.

Haroldson, E.L., 2014, Fluid inclusions and stable isotope study of magino; a magmatic related Archean gold deposit: Unpublished M.Sc. thesis, Madison, University of Wisconsin-Madison, 81 p.

Hastie, E.C.G., Kontak, D.J., and Lafrance, B., 2020, Gold Remobilization: Insights from Gold Deposits in the Archean Swayze Greenstone Belt, Abitibi Subprovince, Canada: Economic Geology, v. 115(2), p. 241-277.

Ilmen, S., Alansari, A., Bajddi, A., and Maacha, L., 2015, Cu-Au vein mineralization related to the Talat n'Imjjad shear zone (western High Atlas, Morocco): geological setting, ore mineralogy, and geochemical evolution: Arabian Journal of Geosciences, v. 8, p. 5039-5056.

Jellicoe, K., 2019, Structural Controls and Deformation History of the Orogenic Island Gold Deposit, Michipicoten Greenstone Belt, Ontario: Unpublished M.Sc. thesis, Waterloo, University of Waterloo, 84 p.

Jiahao, Z., Jingwen, M., Fuquan, Y., Fengmei, C., and Feng, L., 2016, Newly Discovered Native Gold and Bismuth in the Cihai Iron-Cobalt Deposit, Eastern Tianshan, Northwest China: Acta Geologica Sinica, v. 90(3), p. 928-938.

Jochum, K.P., and Hofmann, A.W., 1997, Constraints on earth evolution from antimony in mantle-derived rocks: Chemical Geology, v. 139, 39-49.

Keith, M., Smith, D.J., Jenkin, G.R.T., Holwell, D.A., and Dye, M.D., 2018, A review of Te and Se systematics in hydrothermal pyrite from precious metal deposits: Insights into ore-forming processes: Ore Geology Reviews, v. 96, 269-282.

Kerr, M.J., Hanley, J.J., Kontak, D.J., Morrison, G.G., Petrus, J., Fayek, M., and Zajacz, Z., 2018, Evidence of upgrading gold tenor in an orogenic quartz-carbonate vein system by late magmatic-hydrothermal fluids at the Madrid Deposit, Hope Bay Greenstone Belt, Nunavut, Canada: Geochimica et Cosmochimica Acta, v. 241, p. 180-218.

Kerrich, R., and Wyman, D.A., 1994, The mesothermal gold-lamprophyre association: significance for an accretionary geodynamic setting, supercontinent cycles, and metallogenic processes: Mineralogy and Petrology, v. 51, p. 147-172.

Kolb, J., Meyer, F.M., Vennemann, T., Sindern, S., Prantl, S., Böttcher, M.E. and Sakellaris, G.A., 2010, Characterisation of the Hydrothermal Fluids of the Guelb Moghrein Iron Oxide-Cu-Au-Co Deposit, Mauritania: Ore Mineral Chemistry, Fluid Inclusions and Isotope Geochemistry; *in* Porter, T.M., (ed.), Hydrothermal Iron Oxide Copper-Gold and Related Deposits: A Global Perspective, v. 4 - Advances in the Understanding of IOCG Deposits; *PGC Publishing*, *Adelaide*, pp. 553-572.

Kołodziejczyk, J., Pršek, J., Melfos, V., Voudouris, P.C., Maliqi, F., and Kozub-Budzyń, G., 2015, Bismuth minerals from the Stan Terg deposit (Trepça, Kosovo): Journal of Mineralogy and Geochemistry, v. 192(3), p. 317-333.

Kouhestani, H., Ghaderi, M., Large, R.R., and Zaw, K., 2017, Texture and chemistry of pyrite at Chah Zard epithermal gold-silver deposit, Iran: Ore Geology Reviews, v. 84, p. 80-101.

Large, R.R., Danyushevsky, L., Hollit, C., Maslennikov, V., Meffre, S., Gilbert, S., Bull, S., Scott, R., Emsbo, P., Thomas, H., Singh, B., and Foster, J., 2009, Gold and Trace

Element Zonation in Pyrite Using a Laser Imaging Technique: Implications for the Timing of Gold in Orogenic and Carlin-Style Sediment-Hosted Deposits: Economic Geology, v. 104, p. 635-668.

Lawley, C.J.M., Jackson, S., Yang, Z., Davis, W., and Eglington, B., 2017, Tracing the Transition of Gold from Source to Sponge to Sink: Economic Geology, v. 112, p. 169-183.

Lefebvre, N., Kopylova, M., and Kivi, K., 2005, Archean calc-alkaline lamprophyres of Wawa, Ontario, Canada: Unconventional diamondiferous volcaniclastic rocks: Precambrian Research, v. 138, p. 57-87.

Liu, J., Wang, Y., Huang, S., Wei, R., Sun, Z., Hu, Q., and Hao, J., 2019, The gold occurrence in pyrite and Te-Bi mineralogy of the Fancha gold deposit, Xiaoqinling gold field, southern margin of the North China Craton: Implication for ore genesis: Geological Journal, p. 1-21, doi: 10.1002/gj.3637

Mathieu, L., 2019, Detecting magmatic-derived fluids using pyrite chemistry: Example of the Chibougamau area, Abitibi Subprovince, Québec: Ore Geology Reviews, v. 144, 103127.

McDivitt, J.A., Lafrance, B., Kontak, D.J., and Robichaud, L., 2017, The Structural Evolution of the Missanabie-Renabie Gold District: Pre-orogenic Veins in and Orogenic Gold Setting and Their Influence on the Formation of Hybrid Deposits: Economic Geology, v. 112, p. 1959-1975.

McDivitt, J.A., Kontak, D.J., Lafrance, B., and Robichaud, L., 2018, Contrasting Fluid Chemistries, Alteration Characteristics, and Metamorphic Timing Relationships Recorded in Hybridized Orebodies of the Missanabie-Renabie Gold District, Archean Wawa Subprovince, Ontario, Canada: Economic Geology, v. 113(2), p. 397-420.

McDivitt, J.A., Kontak, D.J., Lafrance, B., Petrus, J.A., and Fayek, M., 2020, A trace metal, stable isotope (H, O, S), and geochronological (U-Pb titanite) characterization of hybridized fold orebodies in the Missanabie-Renabie district, Wawa subprovince (Canada): Mineralium Deposita, doi.10.1007/s00126-020-00983-9

Mikulski, S.Z., 2005, Geological, mineralogical and geochemical characteristics of the Radzimowice Au-As-Cu deposit from the Kaczawa Mountains (Western Sudetes, Poland): and example of the transition of porphyry and epithermal style: Mineralium Deposita, v. 39, p. 904-920.

Monecke, M., Mercier-Langevin, P., Dubé, B., and Frieman, B.M., 2017, Geology of the Abitibi Greenstone Belt *in* Monecke, T., Mercier-Langevin, P., and Dubé, B., (*eds*), Archean Base and Precious Metal Deposits, Southern Abitibi Greenstone Belt, Canada: Reviews in Economic Geology, v. 19, p. 7-50.

Morey, A.A., Tomkins, A.G., Bierlein, F.P., Weinberg, R.F., and Davidson, G.J., 2008, Bimodal Distribution of Gold in Pyrite and Arsenopyrite: Examples from the Archean Boorara and Bardoc Shear Systems, Yilgarn Craton, Western Australia: Economic Geology, v. 103, p. 599-614.

Müller, D., and Groves, D.I., 2019, Indirect Associations Between Lamprophyres and Gold-Copper Deposits, *in* Potassic Igneous Rocks and Associated Gold-Copper Mineralization, Mineral Resource Reviews, Springer, Cham, p. 279-306.

Neyedley, K., Hanley, J.J., Fayek, M., and Kontak, D.J., 2017, Textural, Fluid Inclusion, and Stable Oxygen Isotope Constraints on Vein Formation and Gold Precipitation at the 007 Deposit, Rice Lake Greenstone Belt, Bissett, Manitoba, Canada: Economic Geology, v. 112, p. 629-660.

Oberthür, T., and Weiser, T.W., 2008, Gold-bismuth-telluride-sulphide assemblages at the Viceroy Mine, Harare-Bindura-Shamva greenstone belt, Zimbabwe: Mineralogical Magazine, v. 72(4), p. 953-970.

Pitcairn, I.K., 2011, Background concentrations of gold in different rock types: Applied Earth Science, v. 120(1), p. 31-38.

Polat, A., 2009, The geochemistry of Neoarchean (ca. 2700) tholeiitic basalts, transitional to alkaline basalts, and gabbros, Wawa Subprovince, Canada: Implications for petrogenetic and geodynamic processes: Precambrian Research, v. 168, p. 83-105.

Putnis, A., and Austrheim, H., 2013, Mechanisms of Metasomatism and Metamorphism on the Local Mineral Scale: The Role of Dissolution-Reprecipitation During Mineral Re-equilibration *in* Harlov, D.E., and Austrheim, H., *eds*, Metasomatism and the Chemical Transformation of Rock: Lecture Notes in Earth System Sciences, Springer, Berlin, p. 141-170.

Ridley, J.R., and Diamond, L.W., 2000, Fluid chemistry of orogenic lode gold deposits and implications for genetic models: Reviews in Economic Geology, v. 13, p. 141-162.

Rock, N.M.S., and Groves, D.I., 1988, Do lamprophyres carry gold as well as diamonds?: Nature, v. 332, 253-255.

Rock, N.M.S., Groves, D.I., Perring, C.S., and Golding, S.D., 1989, Gold, Lamprophyres, and Porphyries: What Does Their Association Mean?: Economic Geology Monographs, v. 6, p. 609-625.

Sage, R.P., 1988, Geology of carbonatite-alkalic rock complexes of Ontario: Firesand River Carbonatite Complex, District of Algoma: Ontario Geological Survey Study 47, 81 p.

Samson, I.M., Bas, B., and Holm, P.E., 1997, Hydrothermal Evolution of Auriferous Shear Zones, Wawa, Ontario: Economic Geology, v. 92, p. 325-342.

Shao, Y.-J., Wang, W.-S., Liu, Q.Q., and Zhang, Y., 2018, Trace Element Analysis of Pyrite from the Zhengchong Gold Deposit, Northeast Hunan Province, China: Implications for the Ore-Forming Process: Minerals, v. 8, 262.

Spence-Jones, C.P., Jenkin, G.R.T., Boyce, A.J., Hill, N.J., and Sangster, C.J.S, 2018, Tellurium, magmatic fluids, and orogenic gold: An early magmatic fluid pulse at Cononish gold deposit, Scotland: Ore Geology Reviews, v. 102, p. 894-905.

Stachel, T., Banas, Anetta, Muehlenbachs, K., Kurszlaukis, S., and Walker, E.C., 2006, Archean diamonds from Wawa (Canada): samples from deep cratonic roots predating cratonization of the Superior Province: Contributions to Mineralogy and Petrology, v. 151, p. 737-750.

Sullivan, R.W., Sage R.P., and Card, K.D., 1985, U-Pb zircon age of the Jubilee stock in the Michipicoten greenstone belt near Wawa, Ontario: Geological Survey of Canada paper, n. 85-1B, p. 361-365.

Sun, S.S., and McDonough, W.F., 1989, Chemical and isotopic systematics of oceanic basalts: implications for mantle composition and processes: Geological Society of London Special Publications, v. 42, p. 313-345.

Symons, D.T.A., 1989, Age of the Firesand River carbonatite complex from paleomagnetism: Canadian Journal of Earth Sciences, v. 26, p. 2401-2405.

Taylor, W.R., Rock, N.M.S., Groves, D.I., Perring, C.S., and Golding, S.D., 1994, Geochemistry of Archean shoshonitic lamprophyres from the Yilgarn Block, Western Australia: Au

abundance and associations with gold mineralization: Applied Geochemistry, v. 9, p. 197-222.

Tomkins. A.G., Pattison, D.R.M., and Zaleski, E., 2004, The Hemlo Gold Deposit, Ontario: An Example of Melting and Mobilization of a Previous Metal-Sulfosalt Assemblage during Amphibolite Facies Metamorphism and Deformation: Economic Geology, v. 99, p. 1063-1084.

Tomkins, A.G., 2013, On the source of orogenic gold: Geology, v. 41(12), p. 1255-1256.

Tooth, B., Brugger, J., Ciobanu, C.L., and Liu, W., 2008, Modeling of gold scavenging by bismuth melts coexisting with hydrothermal fluids: Geology, v. 36(10), p. 815-818.

Tooth, B., Ciobanu, C.L., Green, L., O'Neill, B., and Brugger, J., 2011, Bi-melt formation and gold scavenging from hydrothermal fluids: An experimental study: Geochimica et Cosmochimica Acta, v. 75, p. 5423-5443.

Törmänen, T.O., and Koski, R.A., 2005, Gold Enrichment and the Bi-Au Association in Pyrrhotite-Rich Massive Sulfide Deposits, Escanaba Trough, Southern Gorda Ridge: Economic Geology, v. 100, p. 1135-1150.

Turek, A., Smith, P.E., and van Schmus, W.R., 1982, Rb-Sr and U-Pb ages of volcanism and granite emplacement in the Michipicoten belt – Wawa, Ontario: Canadian Journal of Earth Sciences, v. 19, p. 1608-1626.

Turek, A., Sage, R.P., and van Schmus, W.R., 1992, Advances in the U-Pb zircon geochronology of the Michipicoten greenstone belt, Superior Province, Ontario: Canadian Journal of Earth Sciences, v. 29, p. 1154-1165.

Velásquez, G., Béziat, D., Salvi, S., Siebenaller, L., Borisova, A.Y., Pokrovski, G.S., and de Parseval, P., 2014, Formation and Deformation of Pyrite and Implications for Gold

Mineralization in the El Callao District, Venezuela: Economic Geology, v. 109, p. 457-486.

Voudouris, P.C., Spry, P.G., Mavrogonatos, C., Sakellaris, G.-A., Bristol, S.K., Melfos, V., and Fornadel, A.P., 2013, Bismuthinite derivatives, lillianite homologues, and bismuth sulfotellurides as indicators of gold mineralization in the Stanos shear-zone related deposit, Chalkidiki, Northern Greece: Canadian Mineralogist, v. 51, p. 119-142.

Wang, C., Huang, Y., Ma, Y., and Zhang, Z., 2019, Geochemistry, mineralogy and mineral chemistry of the Welatam Cu-Mo-Bi-Au prospect, Northeast Myanmar: Ore Geology Reviews, v. 111, 102973.

Witt-Eickschen, G., Palme, H., O'Neill, H.St.C., and Allen, C.M., 2009, The geochemistry of the volatile trace elements As, Cd, Ga, In and Sn in the Earth's mantle: New evidence from in situ analyses of mantle xenoliths: Geochimica et Cosmochimica Acta, v. 73, 1755-1778.

Wyman, D., and Kerrich, R., 1988, Alkaline Magmatism, Major structures, and Gold Deposits: Implications for Greenstone Belt Gold Metallogeny: Economic Geology, v. 83, 454-461.

Zhang, X., and Spry, P.G., 1994, Calculated Stability of Aqueous Tellurium Species, Calaverite, and Hessite at Elevated Temperatures: Economic Geology, v. 89, p. 1152-1166.

Zheng, Y.-F., 1999, Oxygen isotope fractionation in carbonate and sulfate minerals: Geochemical Journal, v. 33, p. 109-126.

Zheng, B., Zhu, Y., An, F., Huang, Q., and Qiu, T., 2015, As-Sb-Bi-Au mineralization in the Baogutu gold deposit, Xinjiang, NW China: Ore Geology Reviews, v. 69, p. 17-32.

Zhou, H., Sun, X., Fu, Y., Lin, H., and Jiang, L., 2016, Mineralogy and mineral chemistry of Bi-minerals: Constraints on ore genesis of the Beiya giant porphyry-skarn gold deposit, southwestern China: Ore Geology Reviews, v. 79, p. 408-424.

Zhou, H., Sun, X., Cook, N.J., Lin, H., Fu, Y., Zhong, R., and Brugger, J., 2017, Nano- to Micron-Scale Particulate Gold Hosted by Magnetite: A Product of Gold Scavenging by Bismuth Melts: Economic Geology, v. 112, p. 993-1010.

Zhou, H., Sun, X., Wu, Z., Yang, T., Li, D., Ren, Y., Liu, Q., Zhu, K., and Yu, H., 2018, Mineralogy of Bi-sulfosalts and tellurides from the Yaoan gold deposit, southwest China: Metallogenic implications: Ore Geology Reviews, v. 98, p. 126-140.

F-JSZ Assemblages			MSZ Assemblages		
Mineral	Formula	Abbreviation	Mineral	Formula	Abbreviation
Gold	Au	Au	Gold	Au	Au
Tsumoite	BiTe	Tsm	Maldonite	Au_2Bi	Mld
?	$*Bi_{36}Te_{41}S_{23}$	Bi-Te-S	Bismuth	Bi	Bi
			Tsumoite	BiTe	Tsm
			Jonassonite	$AuBi_5S_4$	Jon
			Ingodite	$Bi_2(S,Te)$	Ing
			Bismuthinite	Bi_2S_3	Bsm

Table 3.1 – Names, formulae, and abbreviations for the Au-Bi-Te-S minerals documented in the WGC. Note that for the unknown Bi-Te-S mineral, the empirical formula is given in atomic percent (normalized to 100 %).

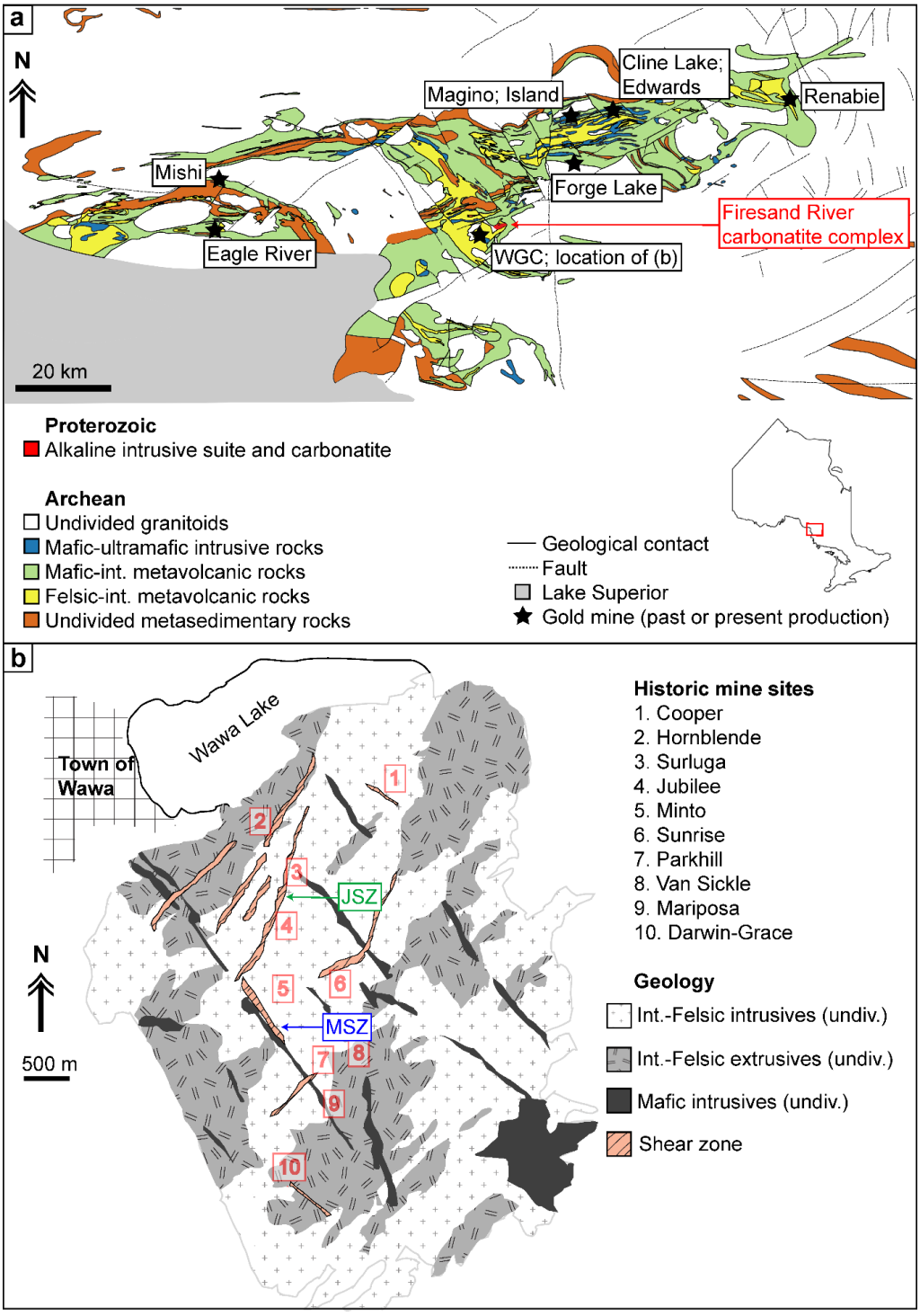

Figure 3.1 – (a) Regional geology of the Michipicoten greenstone belt, modified after data from the Ontario Geological Survey MRD 126-1 with deposit locations are from the Mineral Deposit Inventory of Ontario (https://data.ontario.ca/dataset/mineral-deposit-inventory-of-ontario). (b) Simplified geology of the Jubilee Stock, modified after Red Pine Exploration's internal maps (samples in this study are from the shear zones labelled MSZ and JSZ).

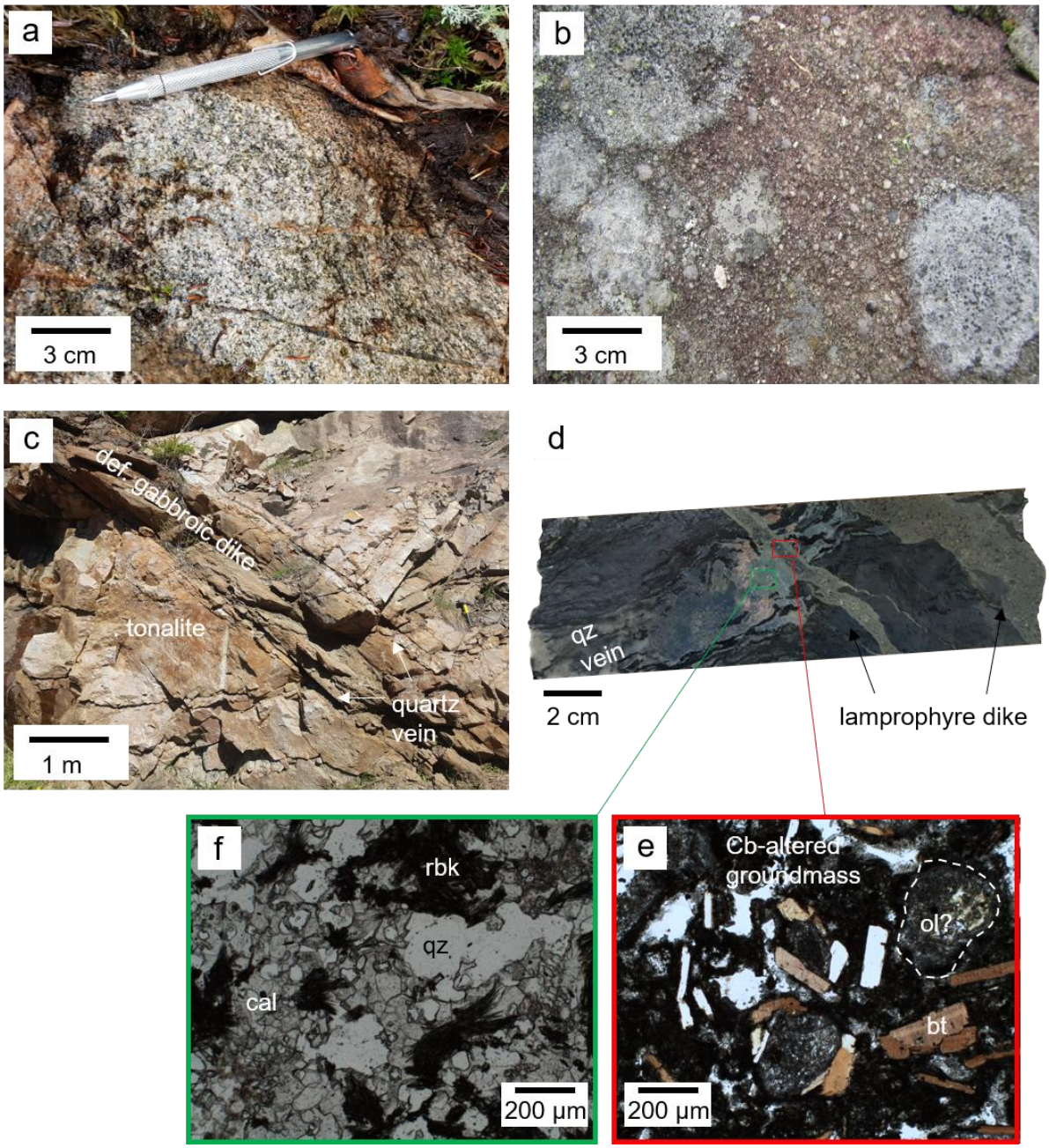

Figure 3.2 – Representative litholologies of the Jubilee Stock. (a) Coarse-grained, undeformed diorite. (b) Quartz + feldspar porpyhyritic unit. (c) Deformed gabbroic dike with marginal quartz veins cutting undeformed tonalite. (d) Neoproterozoic lamprophyre dikes with blue-green riebeckite + calcite alteration haloes. (e) Phenocrystic biotite in a carbonate-altered groundmass; the dashed white lines outline a grain with a stubby prismatic morphology and irregular fracture pattern, which may have been olivine prior to replacement by carbonate. (f) Riebeckite and calcite in the alteration halo of a lamprophyre. Note that the locations of (e) and (f) are shown by the red and green boxes, respectively, in (d). Abbreviations: qz = quartz; rbk = riebeckite; cal = calcite; mag = magnetite; bt = biotite; ol = olivine; cb = carbonate. (e) and (f) are plane-polarized photomicrographs.

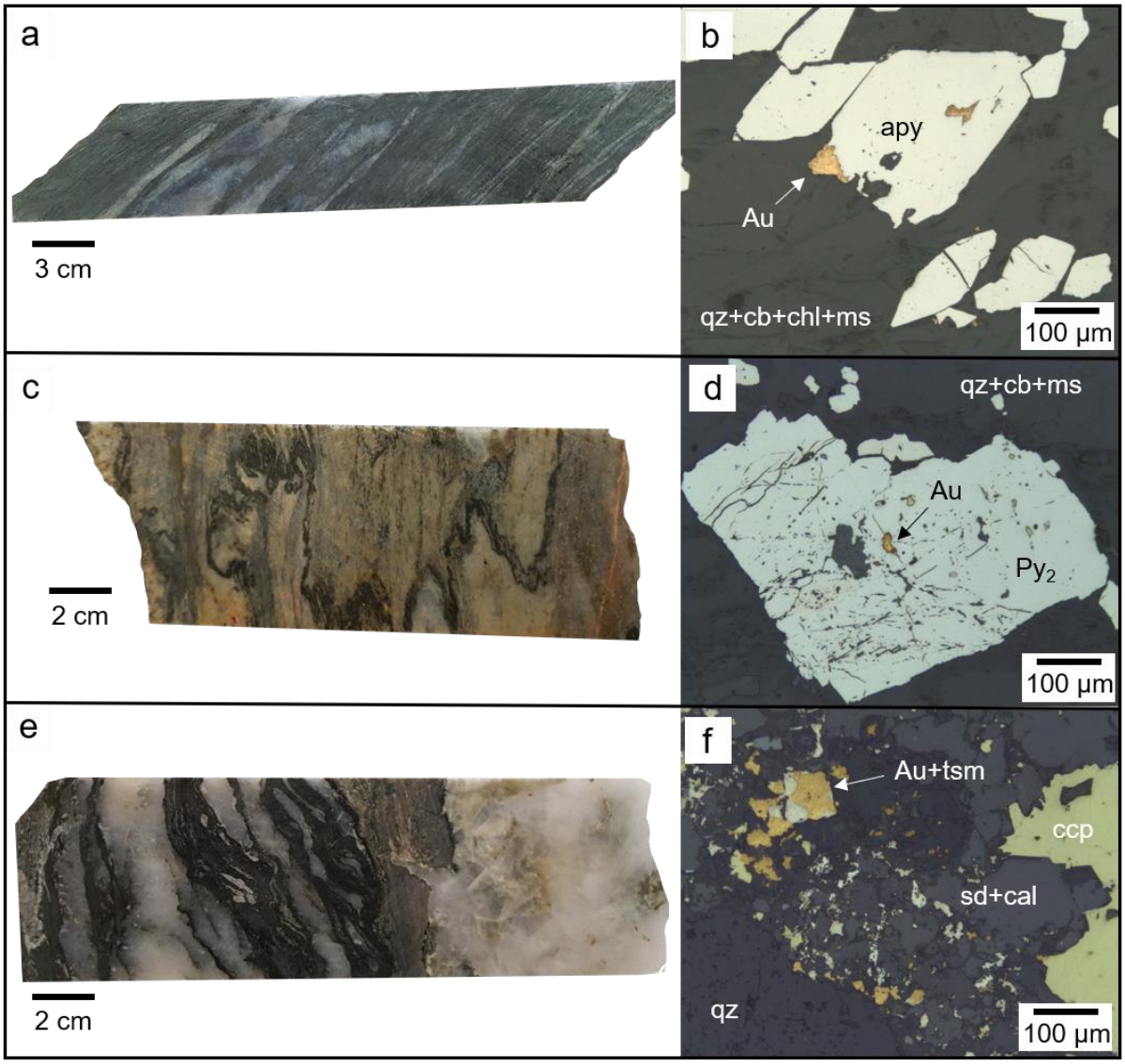

Figure 3.3 – Representative structural features and styles of gold mineralization belonging to the three principal periods of deformation that formed the WGC. (a, b) D_1 chlorite + muscovite + quartz + carbonate schist with bands of fine-grained disseminated arsenopyrite and gold. (c, d) D_2 quartz + muscovite + carbonate schist hosting porphyroblastic Py_2 with inclusions of gold. (e, f) D_3 quartz + tourmaline + carbonate shear vein crosscut by carbonate veinlets that host gold with chalcopyrite and Bi-Te minerals (in this case, tsumoite). Note that (b), (d), and (f) are reflected-light photomicrographs that correspond to (a), (c), and (e), respectively. Additional abbreviations: Au = gold; apy = arsenopyrite; py = pyrite; chl = chlorite; ms = muscovite; sd = siderite; ccp = chalcopyrite; tsm = tsumoite (BiTe)

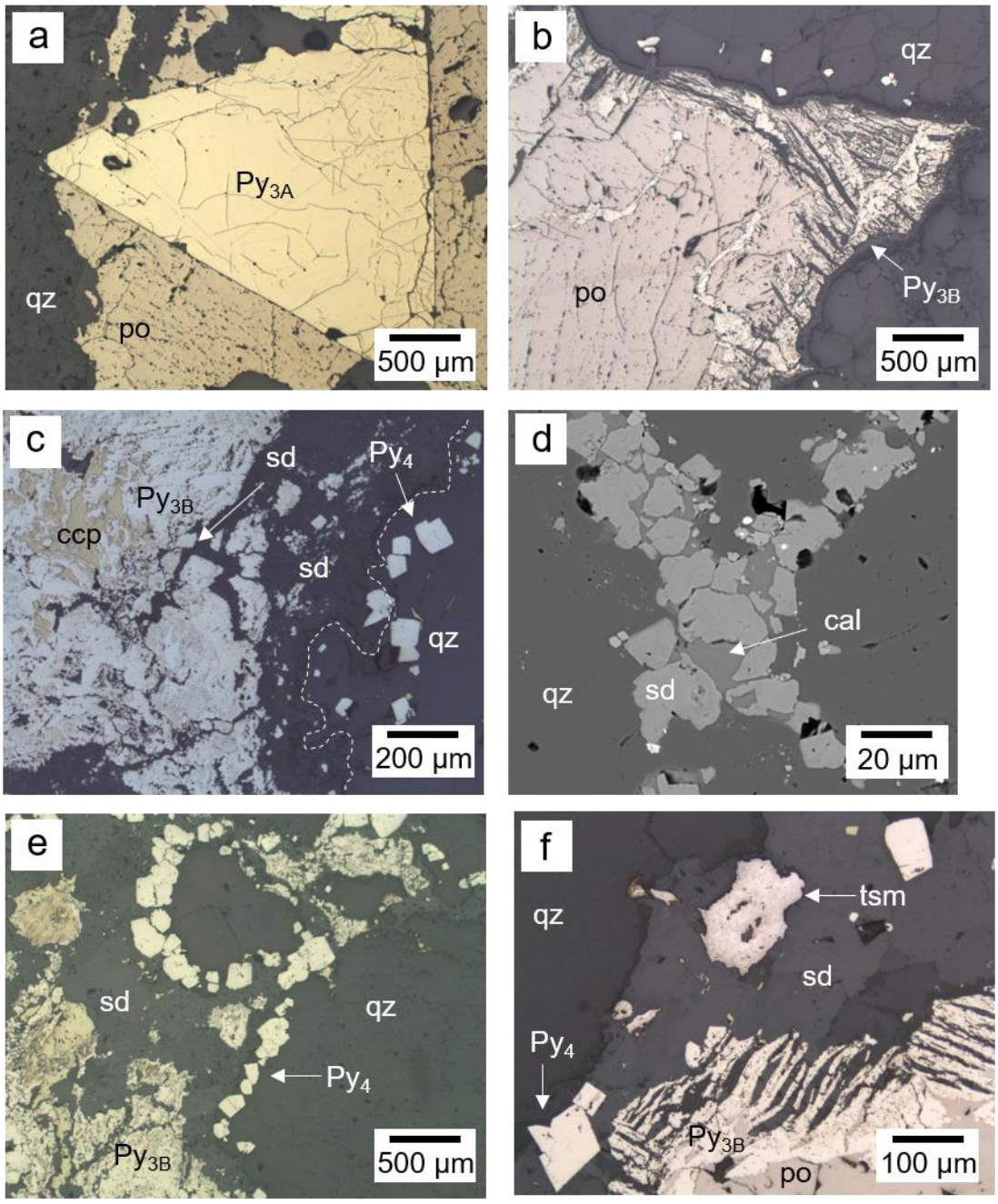

Figure 3.4 – Texturally-representative mineral assemblages in D_3 shear veins. (a) Sharp contacts between euhedral Py_{3A} and surrounding anhedral pyrrhotite. (b) Infiltration and replacement of pyrrhotite by anhedral Py_{3B}. (c) Replacement of Py_{3B} by chalcopyrite and siderite. (d) Calcite cross-cutting siderite in a veinlet that intruded the quartz matrix of D_3 shear vein. (e) Localization of euhedral Py_4 in the exterior margins of the siderite alteration envelope around Py_{3B} (note the planar contacts between Py_4 and siderite). (f) Tsumoite in the siderite alteration halo around a bleb of pyrrhotite and Py_{3B}. All images are reflected-light photomicrographs, with the exception of (d), which is a BSE image. The dashed white line in (c) approximates the boundary between the siderite alteration rim and shear vein quartz.

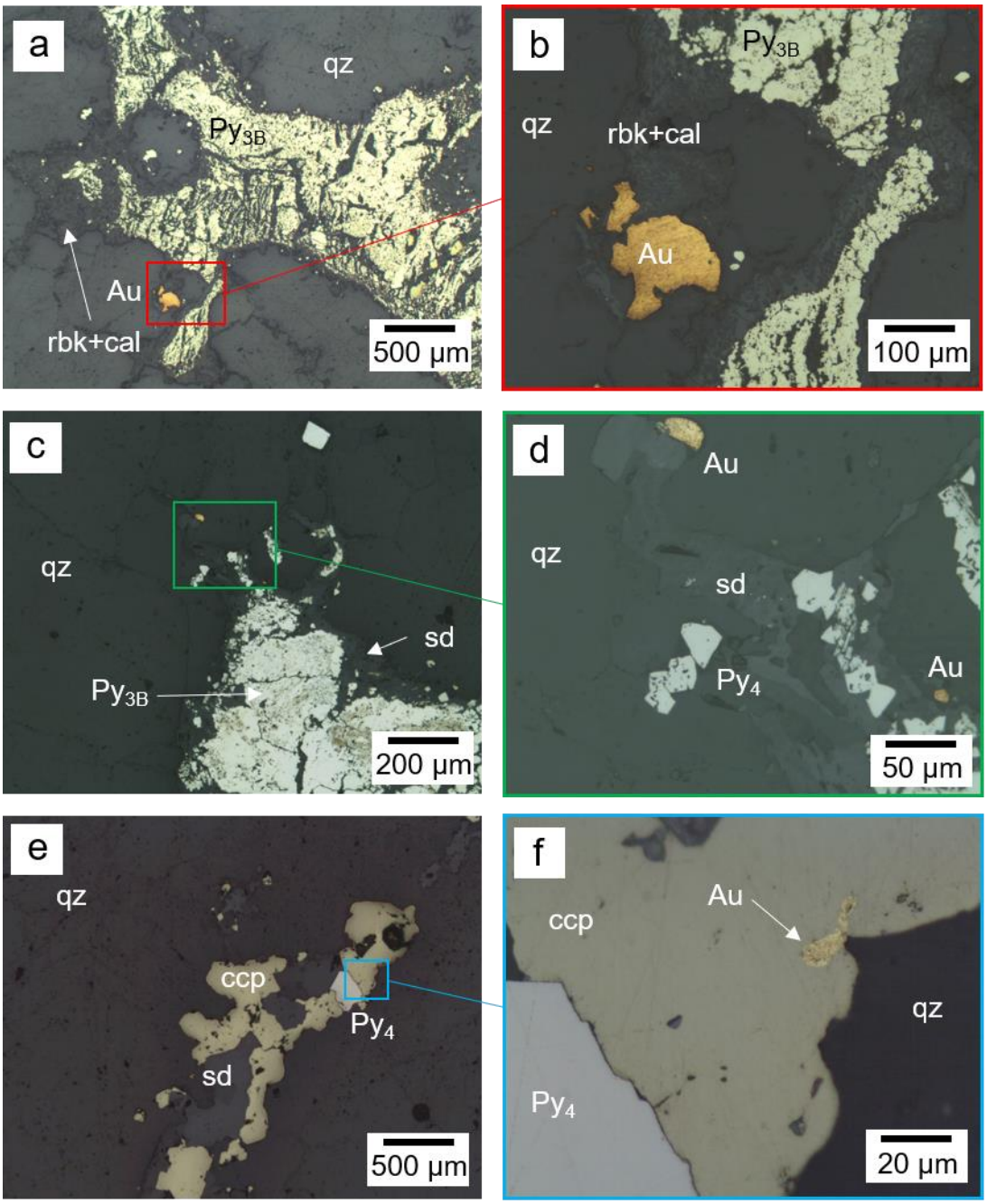

Figure 3.5 – Occurrence of gold in the absence of Bi-Te minerals. (a, b) Gold hosted by a riebeckite + calcite alteration zone around Py_{3B}. (c, d) Gold hosted by a siderite + Py_4 alteration zone around Py_{3B}. (e, f) Gold associated with chalcopyrite and Py_4 in a siderite veinlet cutting D_3 shear vein quartz. All images are reflected-light photomicrographs. The coloured boxes in (a), (c), and (e) outline the locations of (b), (d), and (f), respectively.

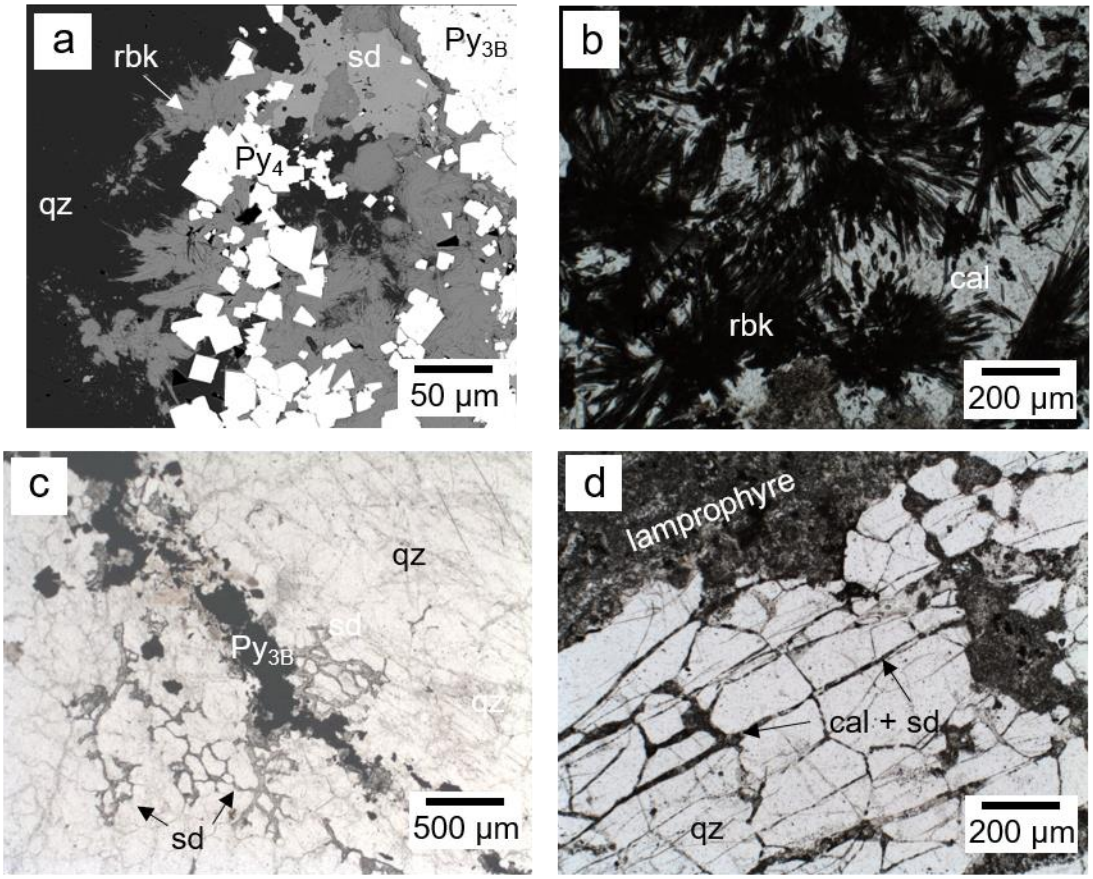

Figure 3.6 – Mineralogical and textural similarities between the siderite alteration haloes that occur around blebs of pyrrhotite and Py_{3B} (a,c) and the alteration footprint of Proterozoic lamprophyres (b,d) include the rare presence of riebeckite (a,b) and the occurrence of carbonate veinlets that exploit gran boundaries and fractures in shear vein quartz (c,d). All images are transmitted-light photomicrographs, except for (a), which is a BSE image.

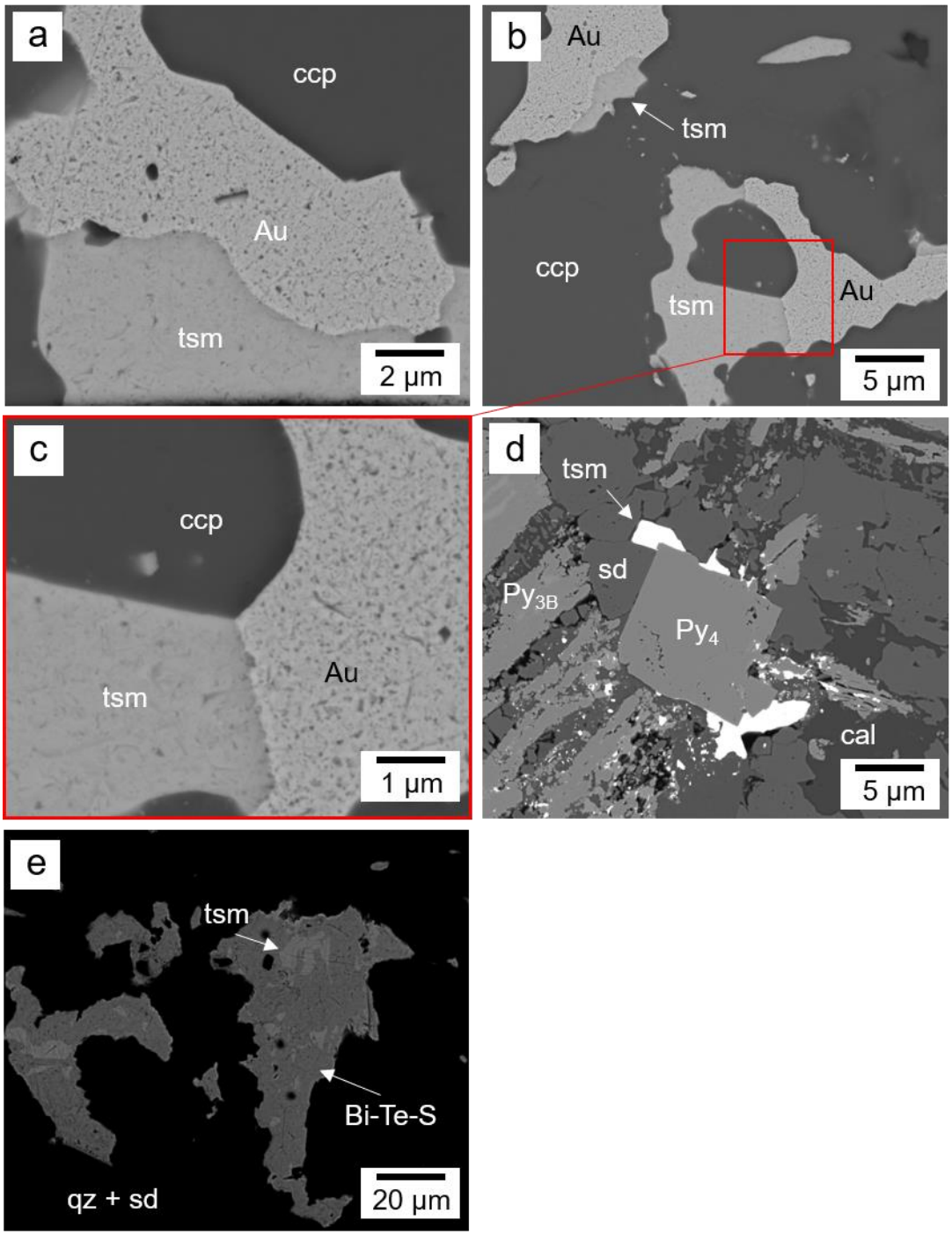

Figure 3.7 – Textural relationships amongst JSZ assemblages. (a) Curvilinear boundaries between gold and tsumoite, hosted by chalcopyrite. (b, c) The intersection gold, tsumoite, and chalcopyrite at a 120° triple-junction. (d) Planar grain boundaries between tsumoite, siderite, and Py_4. (e) The envelopment of tsumoite by an unknown Bi-Te-S mineral (the empirical formula of this mineral in atomic percent, as collected by SEM-EDS, is approximately $Bi_{36}Te_{41}S_{23}$). Note that the red box in (b) outlines the location of the image in (c). All are BSE images.

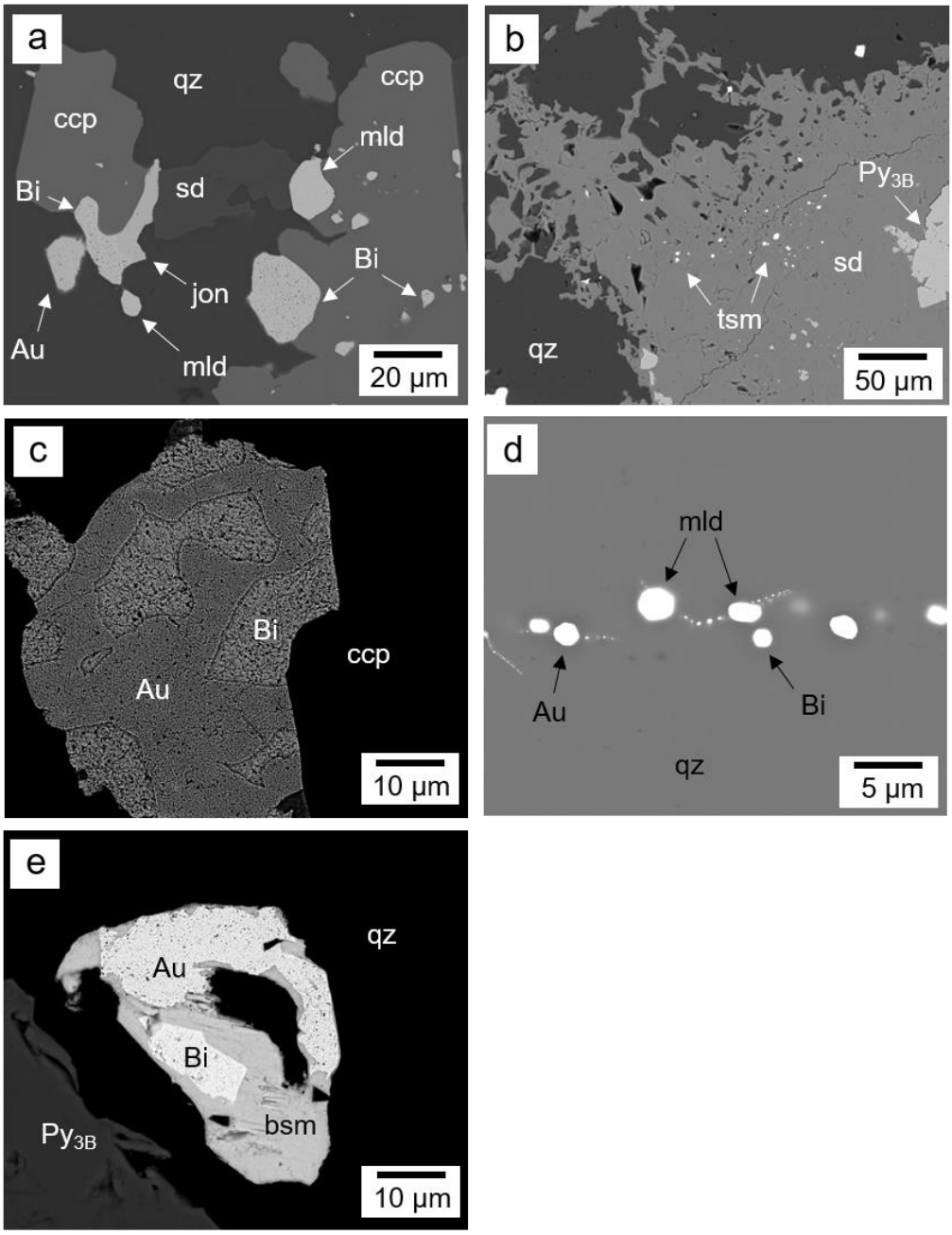

Figure 3.8 - Textural relationships amongst MSZ assemblages. (a) Curvilinear boundaries between bismuth and jonassonite, as well as the occurrence of blebs of bismuth and maldonite within chalcopyrite (note the planar contacts between siderite and jonassonite and siderite and maldonite). (b) Blebs of tsumoite disseminated throughout siderite without Py_4. (c) Intergrowths of gold and bismuth adjacent to chalcopyrite. (d) Trails of spherical grains of gold, maldonite, and bismuth along fractures in shear vein quartz. (e) Bismuthinite forming around gold and bismuth. All are BSE images. Additional abbreviations: Bi = bismuth; mld = maldonite; jon = jonassonite; bsm = bismuthinite.

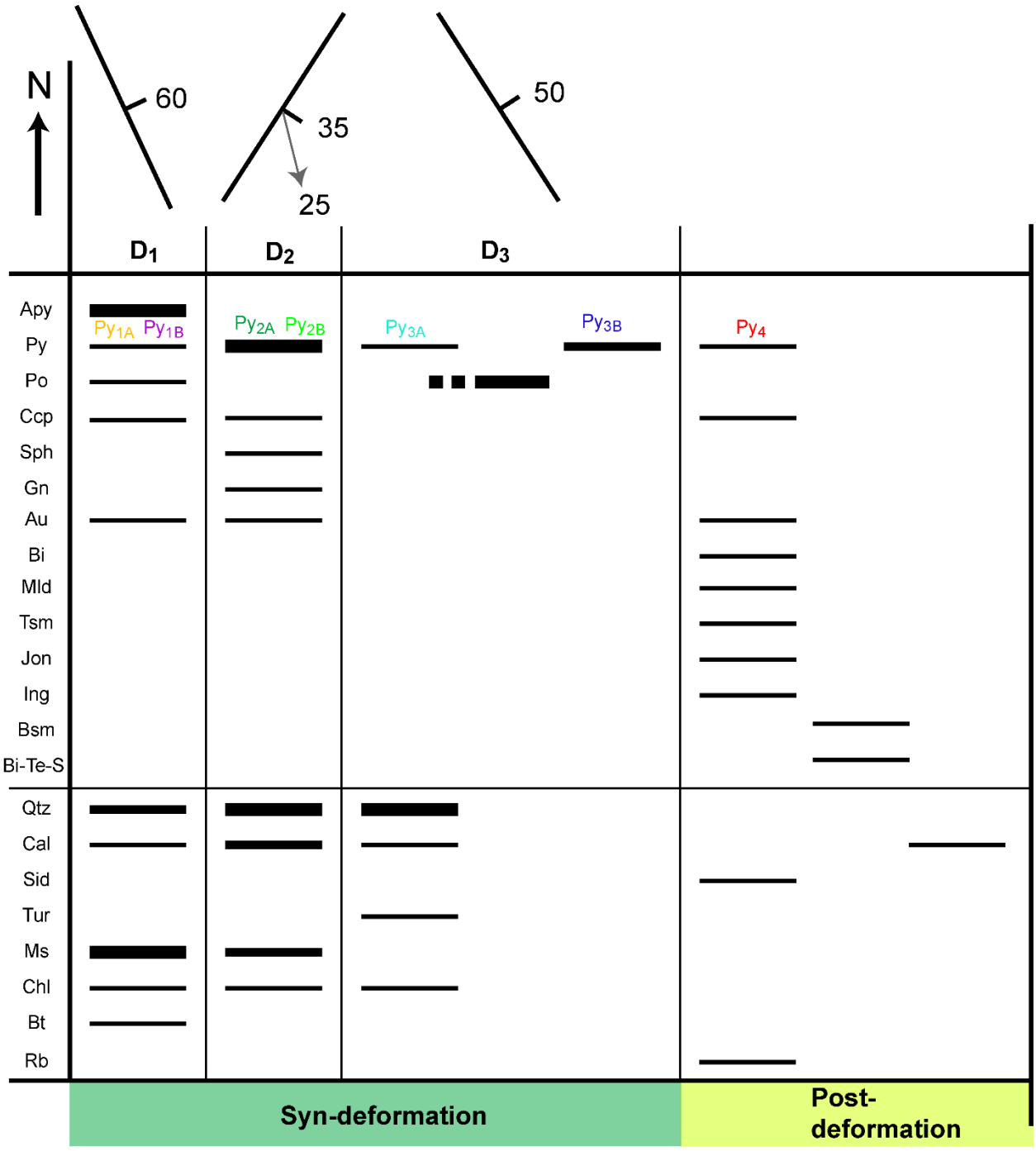

Figure 3.9 – Hydrothermal mineral paragenesis for the WGC. The strike-dip symbols represent the dominant orientation of the foliations in the shear zones formed during each deformation event, and the grey arrow denotes a stretching lineation. Greater detail on the hydrothermal evolution of the WGC during D_1 and D_2 is presented in Chapter Two.

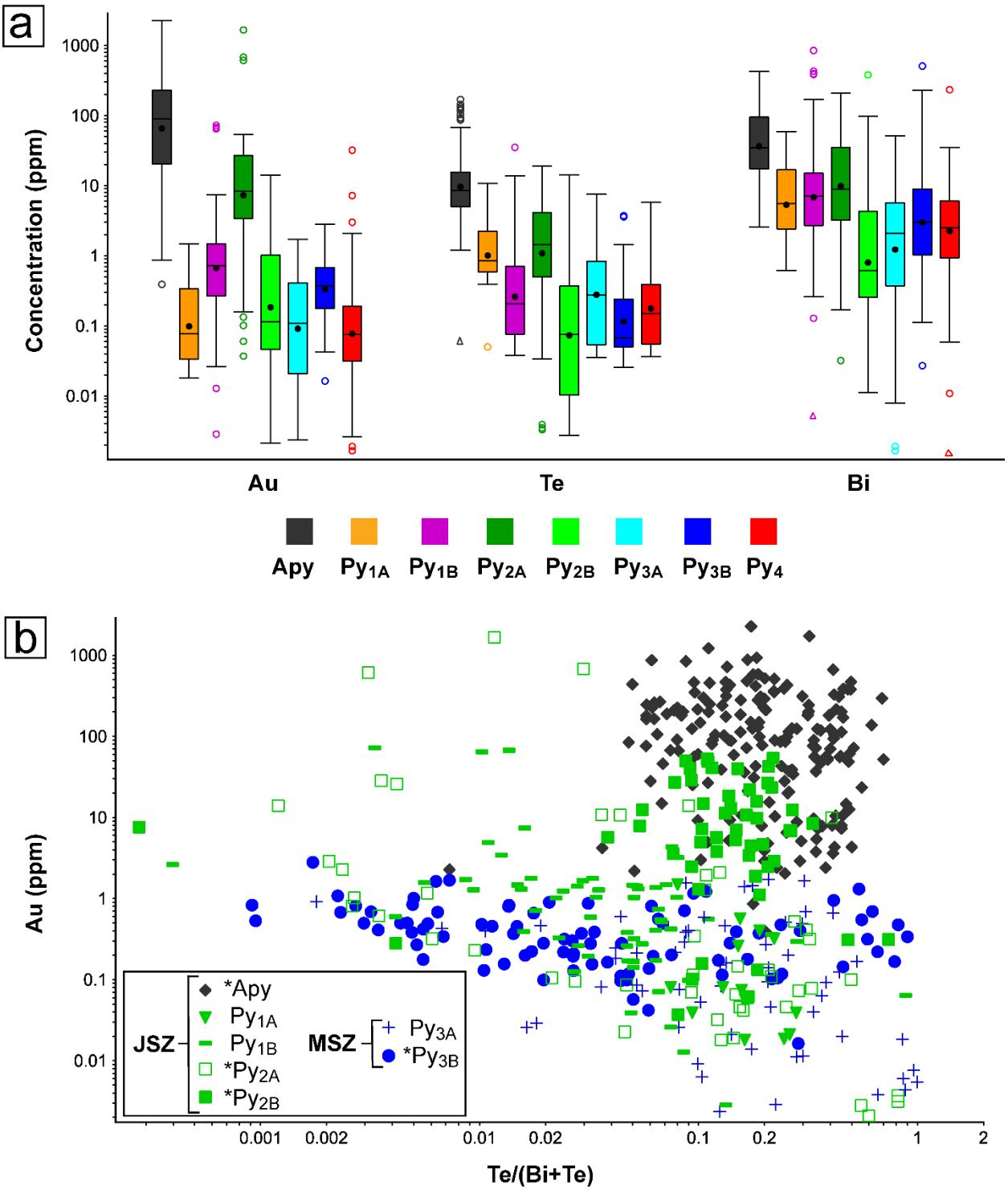

Figure 3.10 – Trace-element characteristics of the dominant sulfide generations in the WGC. Note the relatively higher concentrations of Te in arsenopyrite and Py_{2A-B} (the most abundant sulfides in the JSZ) as compared to Py_{3A} and Py_{3B}, as well as the comparable concentrations of Au, Bi, and Te between Py_{3B} and Py_4 (a). The bivariate plot in (b) demonstrates that the sulfides in the JSZ tend to have greater proportions of Te (as compared to Bi) than those in the MSZ.

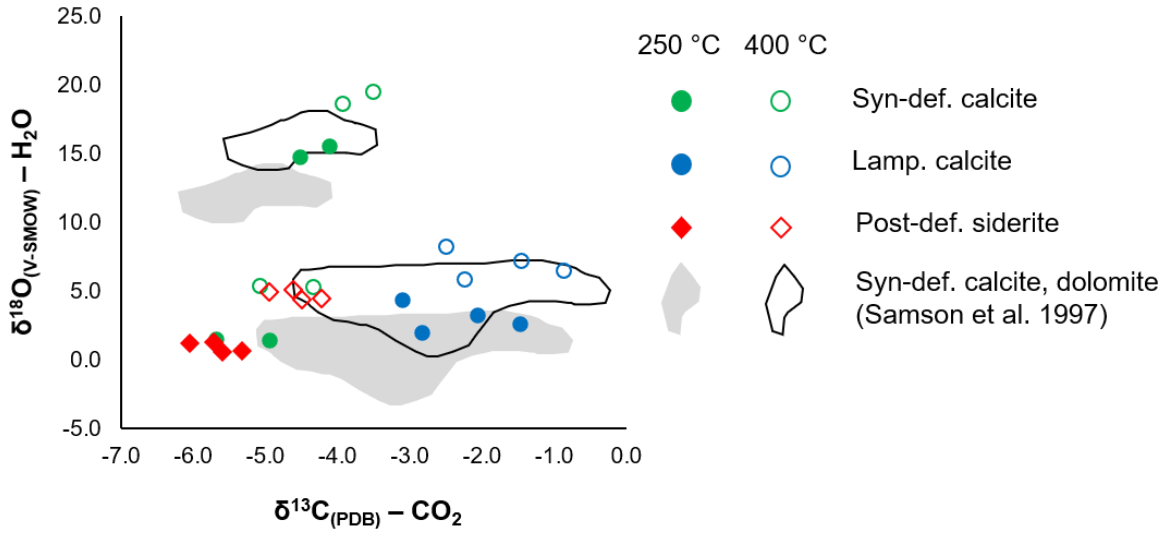

Figure 3.11 – Bivariate plot of $\delta^{13}C$ and $\delta^{18}O$ values of CO_2 and H_2O, respectively, as derived from the isotopic analysis of carbonate minerals in the WGC. These values were calculated at 250 °C and at 400 °C using the fractionation factors of Zheng (1999) (for $\delta^{18}O$) and of Golyshev et al. (1981) (for $\delta^{13}C$). "Syn-def. calcite" (green dots) refers to coarse patches of calcite in D_3 shear veins. "Lamp. calcite" refers to calcite that occurs in the alteration haloes of Neoproterozoic lamprophyres. "Post-def. siderite" refers to the siderite in the alteration zones around Py_{3B} that host Au-Bi-Te assemblages. The grey zones and black-outlined areas delineate the spread of the data collected by Samson et al. (1997), which comprise D_1-D_3 calcite and dolomite.

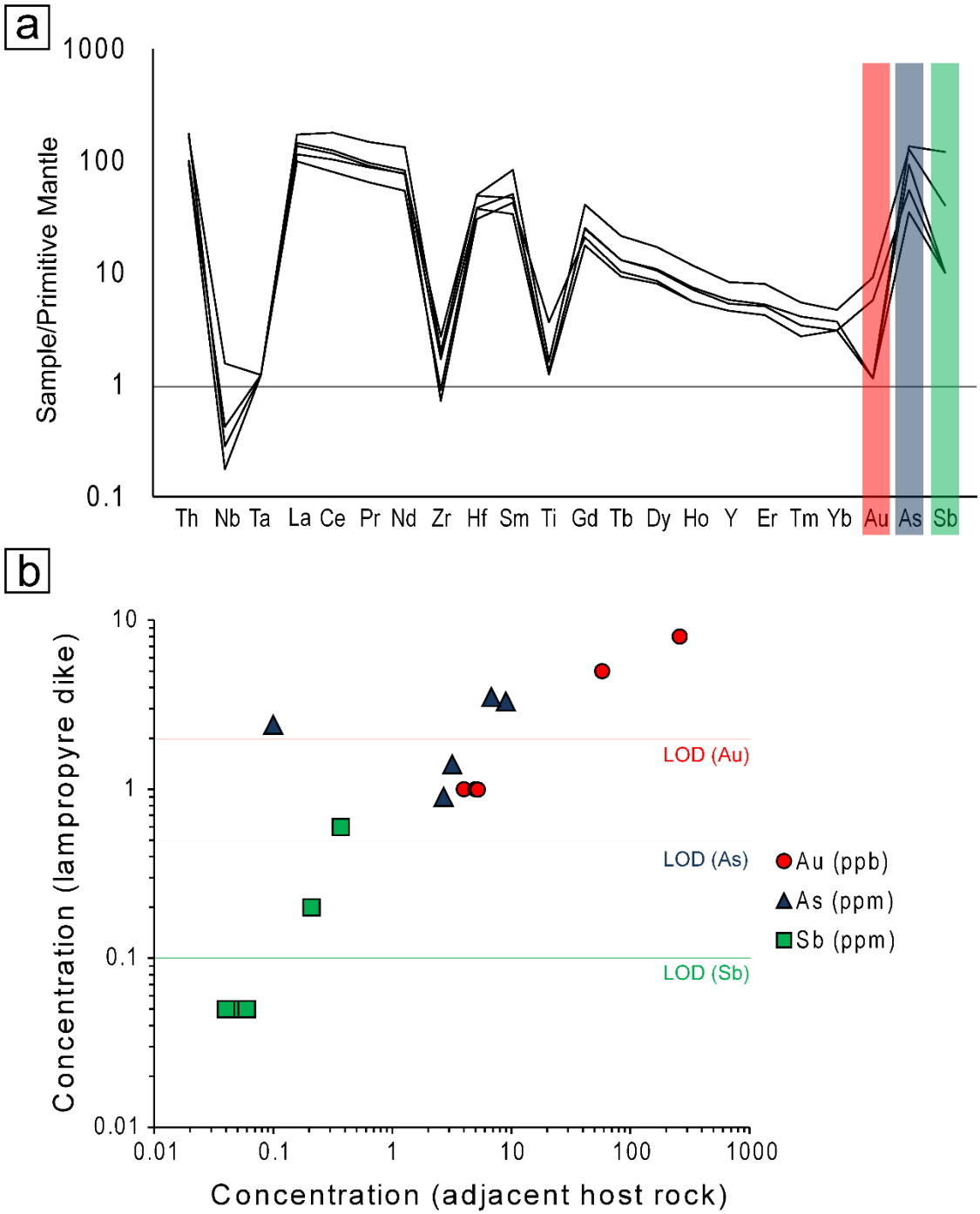

Figure 3.12 – Whole-rock geochemical characteristics of Neoproterozoic lamprophyres. (a) Spidergram showing LREE enrichment and HFSE element depletion, normalized to primitive mantle (Sun and McDonough 1989). Note the spread in the data for Au, As, and Sb. The primitive mantle normalization factors for these three elements are from Pitcairn (2011), Witt-Eickschen et al. (2009), and Jochum and Hofmann (1997), respectively. (b) Concentrations of Au, As, and Sb in lamprophyre dike samples plotted against the concentrations of those elements in the host rocks adjacent to each dike (taken from assay data). LOD = limit of detection.

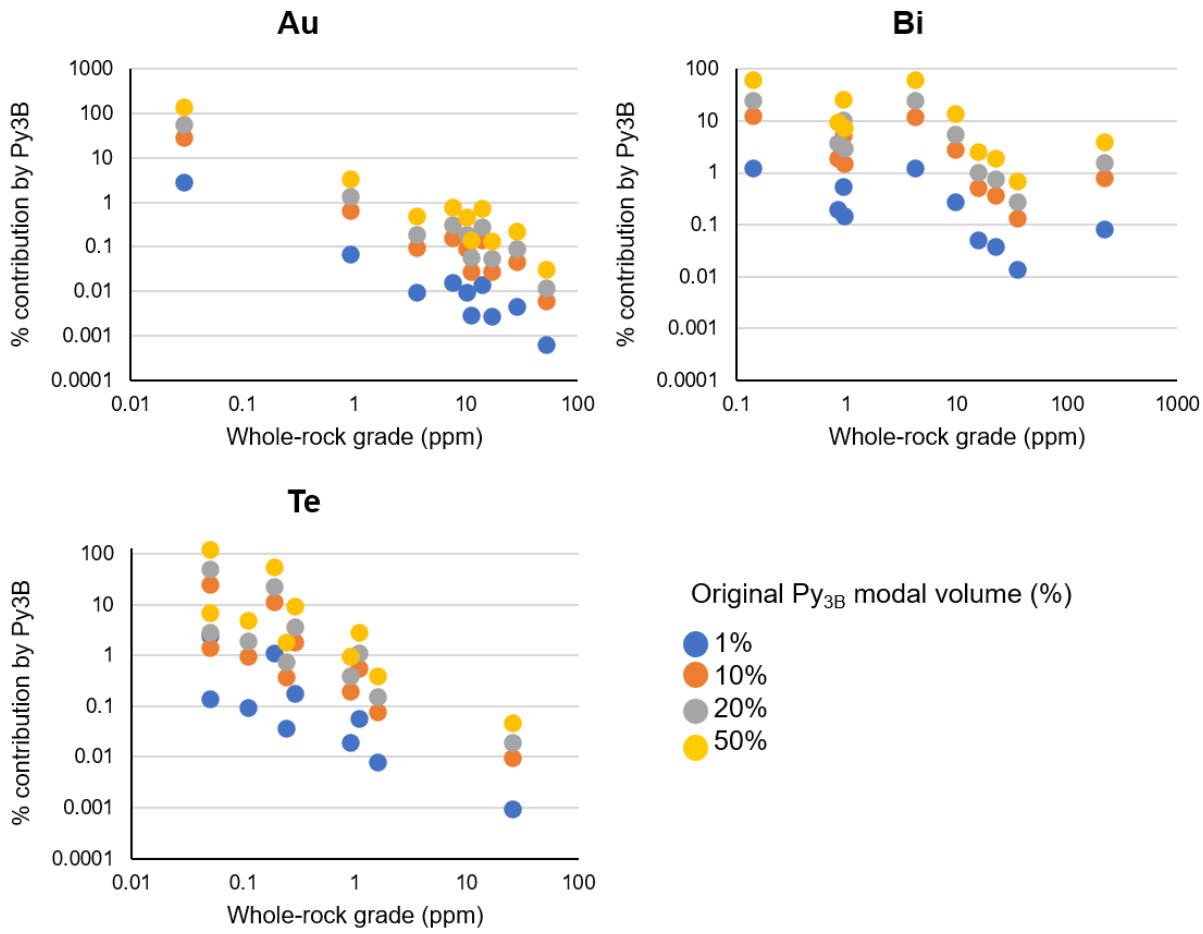

Figure 3.13 – Results of mass-balance calculations performed to assess the potential of Py_{3B} to have been the source of the Au, Bi, and Te found in the D_3 shear veins. The percentage is that of the contribution of each element by mass from Py_{3B} (as outlined in Equation 3.1 in the text) against the whole-rock concentration of the element. Each point represents an individual sample from which multiple grains of Py_{3B} (n = 5 – 10) were analyzed by LA-ICP-MS to determine an average concentration of Au, Bi, and Te in the pyrite. The coloured series represent the percentage of each element by mass that could have been generated assuming theoretical starting modal volumes of Py_{3B} (and if all of this pyrite was dissolved). Note that based on drill core and petrographic observations, the 1% series (blue points) is the most accurate.

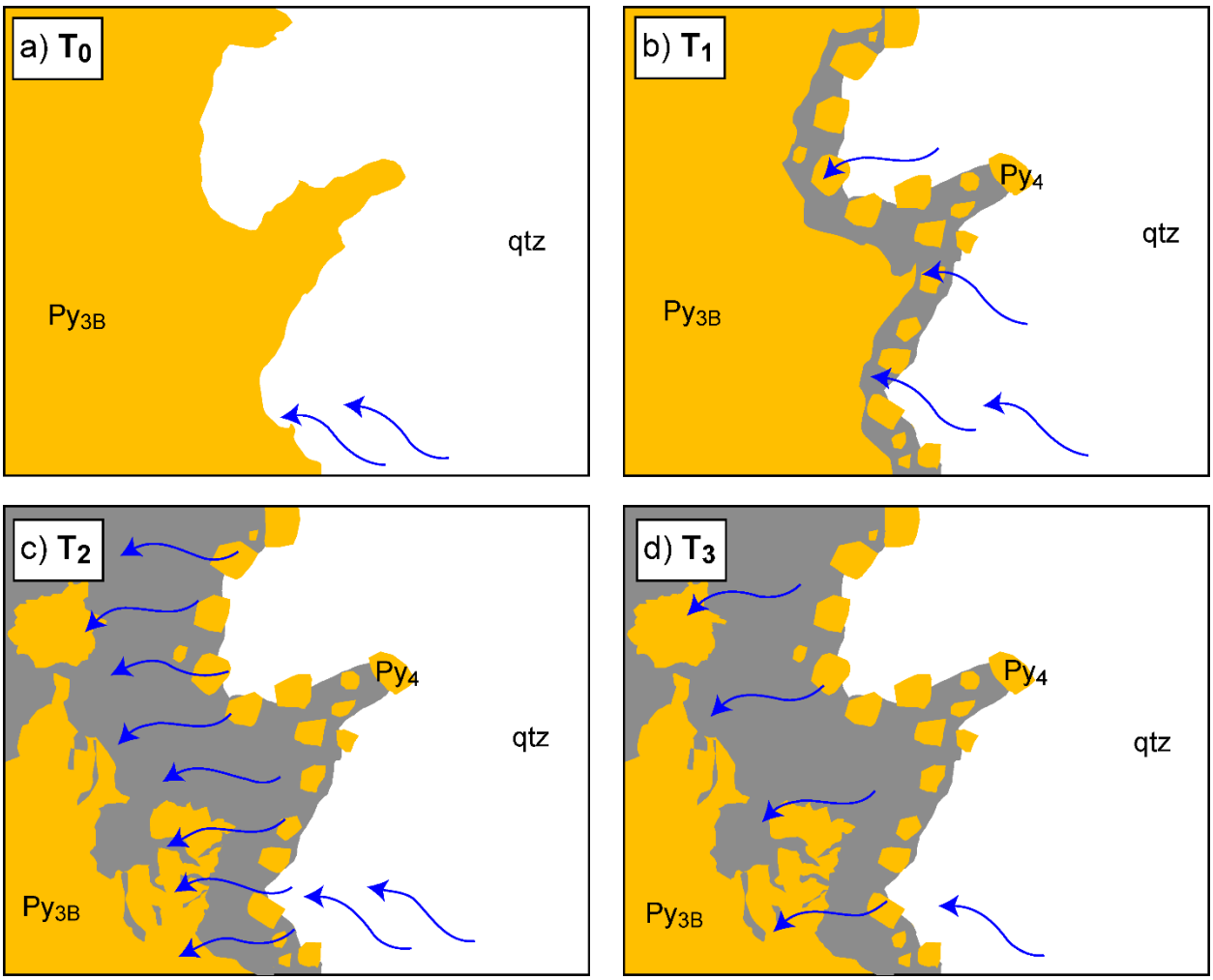

Figure 3.14 – schematic cartoon illustrating the interpreted evolution of the pyrite-siderite replacement reaction with time. The blue arrows denote the direction of the progression of the hydrothermal fluid (starting from the outer rim of the Py_{3B} bleb and moving inwards). The number of blue arrows corresponds to the relative amount of hydrothermal fluid in the system (and thus fluid : rock ratio, as outlined in the text).

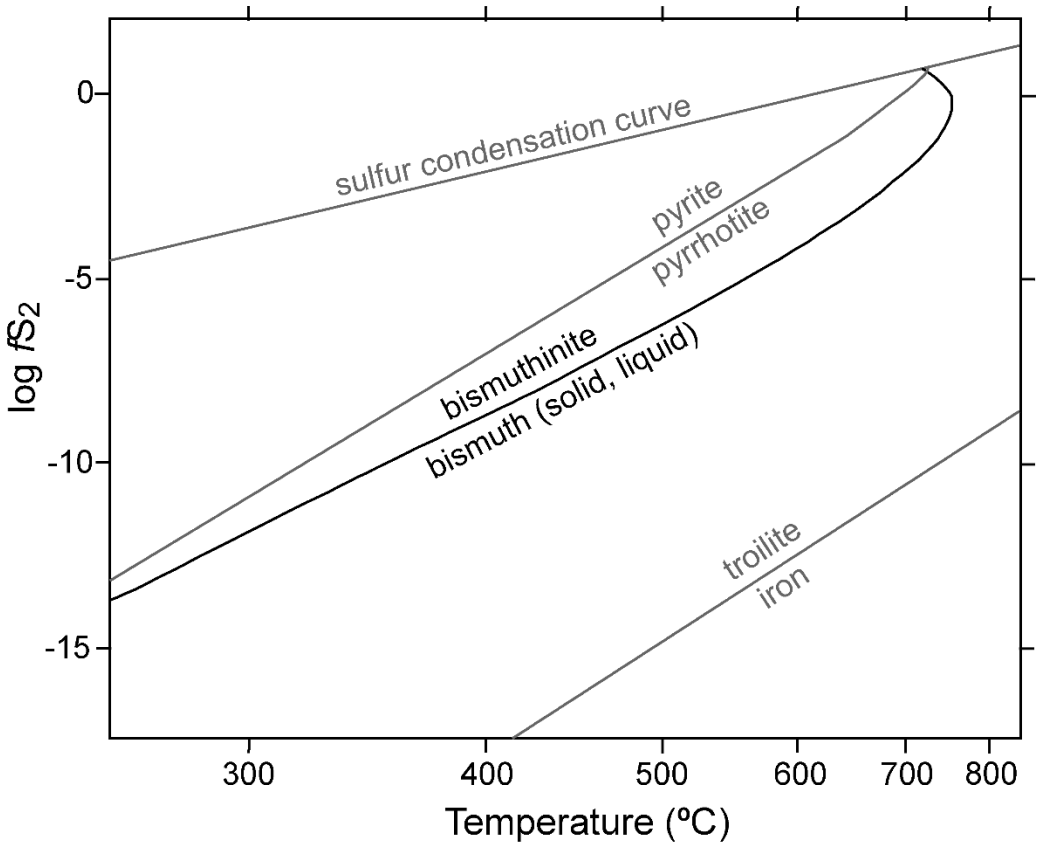

Figure 3.15 – Phase diagram of the Fe-S system in T – fS_2 space with the boundary between bismuthinite and bismuth superimposed; data are from Barton and Skinner (1979), and this iteration of the plot is drawn after Cockerton and Tomkins (2012).

4.1 – Conclusions and recommendations for future research

It is emphasized in this research the extent to which a single occurrence of primary Au enrichment can be modified to produce temporally, mineralogically, and geochemically diverse gold-bearing assemblages. The mechanisms behind this redistribution (e.g., CDR reactions in Au-bearing sulfides, polymetallic melting) were instrumental in the development of native gold from solid-solution Au. When considering the unanswered questions in gold deposit research that relate to the source of Au-bearing fluids, it is clear that any meaningful investigation should be targeted at events that introduced new Au to a system. So, the impact of gold mobilization and redistribution within a deposit must be assessed before the original source of Au can be resolved. This can be accomplished in part with mass-balance calculations based on sulfide trace-element chemistry. This study has characterized Au mineralization by means of sulfide chemistry and mineral associations. However, the minor- and trace-element composition of gold could also potentially be used as a method of discrimination between gold generated during different events (primary or secondary). Given the importance of differentiating between multiple episodes of Au introduction and mobilization within a single deposit, this idea is a clear candidate for future investigation.

Gold deposits in the MGB appear to be characterized by pre-deformation, syn-deformation, and post-deformation hydrothermal activity. Unlike other systems in the MGB (e.g., Missanabie-Renabie (McDivitt et al. 2017, 2018, 2020) and possibly Magino (Haroldson 2014)), however, the pre-deformation event did not introduce substantial amounts of Au to the WGC. Two hypotheses are proposed: (1) the pre-deformation hydrothermal event comprised fluids from a different source reservoir than the Au-bearing syn-deformation fluids; and (2) the two events comprised fluids from

the same source, but the onset of deformation and development of shear zones was instrumental in focusing fluid flow and thus concentrating gold + sulfide mineralization. These hypotheses can in part be tested through micro-analysis (e.g., mineral chemistry, stable isotopes) of minerals that are common to both events, such as arsenopyrite, pyrite, biotite, and chlorite. The relationship between the pre- and syn-deformation fluid events could be further investigated through Re-Os dating of arsenopyrite, which would also help to link Au + sulfide mineralization in the WGC to other deposits in the MGB where geochronological studies have been conducted (i.e., Island Gold (Jellicoe 2019) and Missanabie-Renabie (McDivitt et al. 2020)).

4.2 – References

Haroldson, E.L., 2014, Fluid inclusions and stable isotope study of magino; a magmatic related Archean gold deposit: Unpublished M.Sc. thesis, Madison, University of Wisconsin-Madison, 81 p.

Jellicoe, K., 2019, Structural Controls and Deformation History of the Orogenic Island Gold Deposit, Michipicoten Greenstone Belt, Ontario: Unpublished M.Sc. thesis, Waterloo, University of Waterloo, 84 p.

McDivitt, J.A., Lafrance, B., Kontak, D.J., and Robichaud, L., 2017, The Structural Evolution of the Missanabie-Renabie Gold District: Pre-orogenic Veins in and Orogenic Gold Setting and Their Influence on the Formation of Hybrid Deposits: Economic Geology, v. 112, p. 1959-1975.

McDivitt, J.A., Kontak, D.J., Lafrance, B., and Robichaud, L., 2018, Contrasting Fluid Chemistries, Alteration Characteristics, and Metamorphic Timing Relationships

Recorded in Hybridized Orebodies of the Missanabie-Renabie Gold District, Archean Wawa Subprovince, Ontario, Canada: Economic Geology, v. 113(2), p. 397-420.

McDivitt, J.A., Kontak, D.J., Lafrance, B., Petrus, J.A., and Fayek, M., 2020, A trace metal, stable isotope (H, O, S), and geochronological (U-Pb titanite) characterization of hybridized fold orebodies in the Missanabie-Renabie district, Wawa subprovince (Canada): Mineralium Deposita, doi.10.1007/s00126-020-00983-9

APPENDICES

Appendix A – Box-whisker plots displaying the limits of detection (LOD) and 2σ errors for individual transect analyses by LA-ICP-MS. Within the box, the white circles indicate the mean and the white lines indicate the median. The approximate values are given in the tables below each plot (all values in ppm).

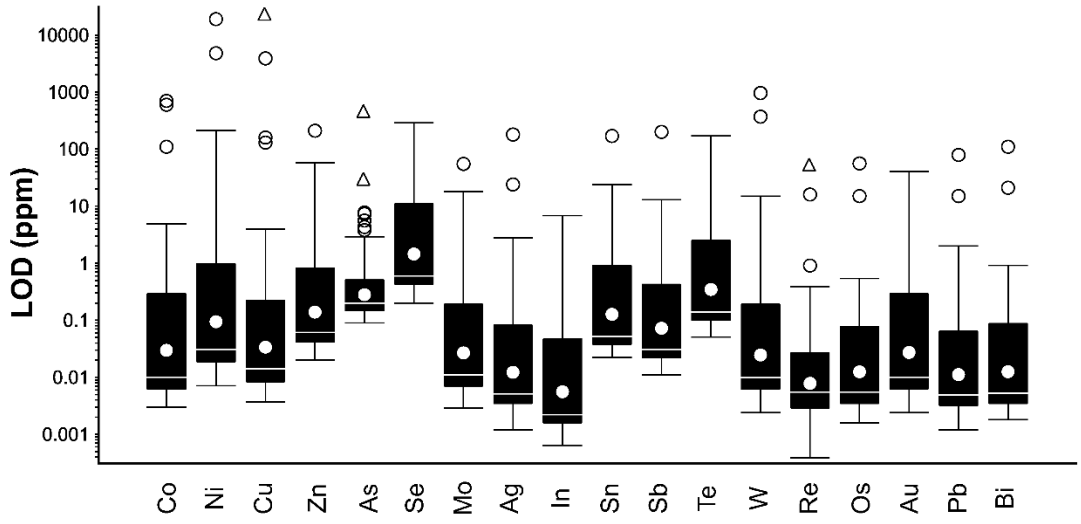

	Co	Ni	Cu	Zn	As	Se	Mo	Ag	In	Sn	Sb	Te	W	Re	Os	Au	Pb	Bi
LOD (mean)	0.03	0.09	0.03	0.14	0.2	1.45	0.03	0.01	0.005	0.12	0.07	0.35	0.02	0.008	0.01	0.03	0.01	0.01
LOD (median	0.01	0.03	0.01	0.06	0.28	0.6	0.01	0.005	0.002	0.05	0.03	0.14	0.01	0.005	0.005	0.01	0.005	0.005

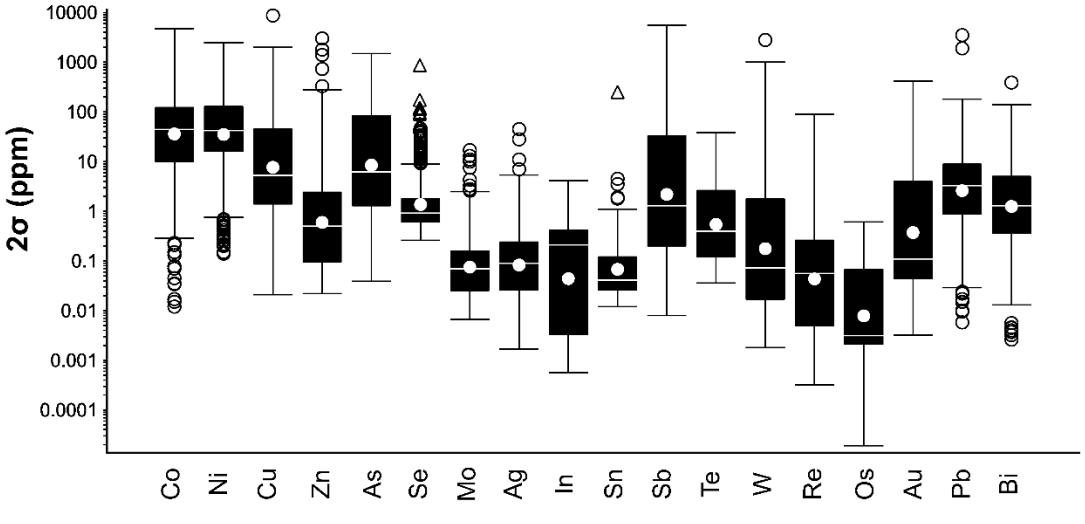

	Co	Ni	Cu	Zn	As	Se	Mo	Ag	In	Sn	Sb	Te	W	Re	Os	Au	Pb	Bi
2σ (mean)	36	35	7.7	0.6	8.5	0.9	0.08	0.08	0.04	0.07	2.2	0.5	0.2	0.04	0.008	0.4	2.6	1.2
2σ (median)	44	42	5.3	0.5	6.2	1.4	0.07	0.09	0.2	0.04	1.3	0.4	0.07	0.06	0.003	0.1	3.3	1.3

Appendix B – Results of LA-ICP-MS analysis of individual sulfide grains. All concentrations are in ppm. The mean, minimum, maximum, and standard deviation for each sulfide population are given. "LOD" means the minimum value was below the detection limit for the analysis. Note that the values of As for arsenopyrite are not given ("N/A"), given that As is a major element in arsenopyrite.

	Co	Ni	Cu	Zn	As	Se	Mo
Arsenopyrite (n = 188)							
Mean	660	440	65	11	N/A	51	0.57
Min.	3.6	75	0.57	0.45	N/A	3.4	0.055
Max.	2900	2400	3000	110	N/A	1010	14
St.Dev.	560	320	280	16	N/A	120	1.4
Py_{1A} (n = 14)							
Mean	12000	640	6.5	0.64	620	6.3	2.0
Min.	850	9.7	0.16	0.18	6.7	2.2	LOD
Max.	39000	2800	58	1.7	3200	11	25
St.Dev.	11000	850	15	0.46	870	2.4	6.6
Py_{1B} (n = 60)							
Mean	790	3100	1100	15	700	13	1.0
Min.	0.23	130	1.8	0.23	0.31	LOD	LOD
Max.	14000	7600	10200	210	4400	28	4.8
St.Dev.	2100	1800	1800	38	1100	7.0	0.9
Py_{2A} (n = 59)							
Mean	170	180	90	730	4800	15	1.7
Min.	3.3	0.71	0.20	0.19	0.85	LOD	LOD
Max.	800	1700	850	6500	16000	80	25
St.Dev.	170	240	160	1700	4400	13	4.9
Py_{2B} (n = 108)							
Mean	330.0	270	14	260	1200	13	0.50
Min.	19	0.71	0.074	0.14	4.3	LOD	LOD
Max.	1300	1100	170	2600	7300	39	10
St.Dev.	300	320	38	470	1700	11	1.7
Py_{3A} (n = 29)							
Mean	3500	230	92	0.7	12	8.8	0.09
Min.	0.14	3.1	0.84	0.23	0.3	3.1	0.019
Max.	22000	1600	530	3.5	66	16	0.48
St.Dev.	6200	400	170	0.84	18	3.4	0.10
Py_{3B} (n = 87)							
Mean	920	2100	1300	2.2	15	13	0.63
Min.	0.048	2.4	8.2	0.16	LOD	8.9	LOD
Max.	10000	15000	42000	27	120	28	4.0
St.Dev.	1800	1900	4600	3.6	23	3	0.48

Py_4 (n = 108)							
Mean	830.0	260	36	1.2	66	13	0.35
Min.	LOD	1.1	0.27	0.20	LOD	1.2	LOD
Max.	15000	2300	570	33	1700	25	15
St.Dev.	2600	410	86	3.4	240	4.3	1.5

	Ag	**In**	**Sn**	**Sb**	**Te**	**W**	**Re**
Arsenopyrite (n = 188)							
Mean	0.79	3.4	1.8	1600	19	49	2.3
Min.	0.033	0.0079	LOD	4.5	LOD	0.090	LOD
Max.	12	7.2	4.9	32000	270	3300	110
St.Dev.	1.6	0.87	1.2	3300	29	280	11
Py_{1A} (n = 14)							
Mean	0.10	0.0033	LOD	0.47	2.0	0.10	0.0053
Min.	LOD	LOD	LOD	LOD	LOD	LOD	LOD
Max.	0.30	0.0048	LOD	2.0	11	0.80	0.019
St.Dev.	0.11	0.00083	N/A	0.57	2.9	0.21	0.0065
Py_{1B} (n = 60)							
Mean	1.5	0.010	0.93	9.0	1.3	0.46	0.017
Min.	LOD	LOD	LOD	LOD	LOD	LOD	LOD
Max.	5.8	0.025	3.9	53	35	7.5	0.15
St.Dev.	1.8	0.0062	0.90	13	4.8	1.4	0.039
Py_{2A} (n = 59)							
Mean	3.0	31	0.21	2.2	3.0	2.6	0.057
Min.	LOD	LOD	0.024	LOD	LOD	LOD	LOD
Max.	48	210	2.5	24	19	51	0.39
St.Dev.	6.6	46	0.52	4.8	3.9	7.1	0.096
Py_{2B} (n = 108)							
Mean	1.0	0.030	0.097	0.31	0.83	0.41	0.018
Min.	LOD	LOD	LOD	LOD	LOD	LOD	LOD
Max.	26	1.1	0.39	3.4	14	8.4	0.23
St.Dev.	4.4	0.16	0.10	0.57	2.6	1.5	0.049
Py_{3A} (n = 29)							
Mean	0.16	0.0019	LOD	0.97	0.49	0.0060	LOD
Min.	0.0021	LOD	LOD	0.0070	0.039	0.0019	LOD
Max.	0.64	0.0027	LOD	6.0	2.2	0.028	LOD
St.Dev.	0.19	0.00059	N/A	1.4	0.58	0.0055	N/A
Py_{3B} (n = 87)							
Mean	1.5	0.0069	0.18	14	0.27	0.042	0.0042
Min.	0.12	LOD	LOD	LOD	LOD	LOD	LOD
Max.	23	0.041	1.1	93	3.7	0.47	0.0080

St.Dev.	2.5	0.012	0.19	17	0.6	0.071	0.0025
Py_4 (n = 108)							
Mean	0.22	0.0060	0.091	3.9	0.4	1.2	0.026
Min.	LOD	LOD	LOD	LOD	LOD	LOD	LOD
Max.	14	0.033	0.63	59	5.8	60	0.17
St.Dev.	1.3	0.0084	0.12	8.0	0.8	5.9	0.052

	Os	Au	Pb	Bi
Arsenopyrite (n = 188)				
Mean	0.10	180	46	62
Min.	LOD	0.39	1.7	2.6
Max.	0.26	2300	310	430
St.Dev.	0.071	280	49	65
Py_{1A} (n = 14)				
Mean	LOD	0.25	9.3	11
Min.	LOD	0.018	0.55	0.62
Max.	LOD	1.5	78	59
St.Dev.	N/A	0.39	20	15
Py_{1B} (n = 60)				
Mean	0.0005	4.5	48	45
Min.	LOD	LOD	0.12	LOD
Max.	0.0006	73	470	850
St.Dev.	0.00014	15	91	140
Py_{2A} (n = 59)				
Mean	0.0011	14	200	31.0
Min.	LOD	0.037	0.032	0.032
Max.	0.0028	54	5700	210
St.Dev.	0.0014	15	780	46
Py_{2B} (n = 108)				
Mean	0.0017	1.5	17	13
Min.	LOD	LOD	0.013	0.011
Max.	0.0035	14	290	380
St.Dev.	0.0013	3.4	55	59
Py_{3A} (n = 29)				
Mean	LOD	0.28	4.5	4.1
Min.	LOD	0.0044	0.055	0.0019
Max.	LOD	1.6	24	23
St.Dev.	N/A	0.40	6.1	5.6

Py_{3B} (n = 87)				
Mean	0.0017	0.47	40	19
Min.	LOD	0.016	0.33	0.027
Max.	0.0051	2.8	520	510
St.Dev.	0.0010	0.43	67	63
Py_{4} (n = 108)				
Mean	0.0028	0.55	23	7.1
Min.	LOD	LOD	0.086	LOD
Max.	0.015	32	330	230
St.Dev.	0.0040	3.2	50	23

Appendix C – Results of SIMS S isotope analysis of pyrite (Py) and chalcopyrite (Ccp). All values are given in ‰ and are reported with respect to V-CDT

	$\delta^{33}S$	2σ (‰)	$\delta^{34}S$	2σ (‰)	$\Delta^{33}S$	2σ (‰)
Ccp (n = 54)						
Mean	0.58	0.24	1.30	0.12	-0.09	0.28
Min.	-0.01	0.13	-0.07	0.12	-0.34	0.17
Max.	1.10	0.41	2.09	0.12	0.28	0.48
St.Dev.	0.30	0.06	0.46	0.00	0.14	0.06
Py_{1B} (n = 23)						
Mean	0.68	0.28	1.26	0.15	0.04	0.28
Min.	-0.01	0.13	-0.07	0.12	-0.34	0.18
Max.	1.16	0.33	2.22	0.20	0.22	0.28
St.Dev.	0.30	0.05	0.47	0.02	0.14	0.05
Py_{2A} (n = 20)						
Mean	1.26	0.27	2.35	0.13	0.05	0.28
Min.	0.95	0.23	1.73	0.11	-0.26	0.28
Max.	1.87	0.34	2.99	0.17	0.39	0.28
St.Dev.	0.29	0.03	0.34	0.01	0.18	0.00
Py_{2B} (n = 20)						
Mean	1.74	0.28	3.26	0.12	0.06	0.28
Min.	0.59	0.22	0.98	0.12	-0.20	0.28
Max.	2.20	0.36	4.09	0.13	0.18	0.28
St.Dev.	0.45	0.03	0.90	0.01	0.10	0.00
Py_{3B} (n = 25)						
Mean	0.73	0.28	1.50	0.13	-0.04	0.26
Min.	0.35	0.25	1.00	0.12	-0.23	-0.28
Max.	1.04	0.34	1.92	0.15	0.14	0.28
St.Dev.	0.20	0.03	0.36	0.01	0.10	0.11
Py_{4} (n = 19)						
Mean	0.76	0.28	1.57	0.13	-0.04	0.28
Min.	0.23	0.25	0.89	0.12	-0.33	0.28
Max.	1.12	0.32	2.09	0.16	0.14	0.28
St.Dev.	0.29	0.02	0.36	0.01	0.14	0.00

Appendix D – Results of IRMS C and O isotope analysis of carbonate minerals. $\delta^{13}C$ values are reported with respect to PDB and $\delta^{18}O$ values are reported with respect to V-SMOW. All values are given in ‰. "Syn-def." = syn-deformation; "Lamp." = lamprophyre; "Post-def." = post-deformation. Precision is ±0.1 ‰.

Mineral	Type	$\delta^{13}C$	$\delta^{18}O$
Calcite	Syn-def.	-6.1	8.9
Calcite	Syn-def.	-5.2	23.1
Calcite	Syn-def.	-5.6	22.3
Calcite	Syn-def.	-6.8	9.0
Calcite	Lamp.	-3.2	10.8
Calcite	Lamp.	-2.6	10.2
Calcite	Lamp.	-3.9	9.5
Calcite	Lamp.	-4.2	11.9
Dolomite	Syn-def.	-6.2	20.0
Siderite	Post-def.	-4.1	9.7
Siderite	Post-def.	-3.7	9.1
Siderite	Post-def.	-4.5	9.6
Siderite	Post-def.	-4.0	9.0

Appendix E – Results of whole-rock geochemistry of lamprophyre dikes. The unit, level of detection, and analytical method are given for each element. INAA = instrumental neuron activation analysis; ICP = inductively coupled plasma spectroscopy; ICP/MS = inductively coupled plasma mass spectrometry. For certain elements, multiple methods were used if a single method was not adequate to measure total concentrations.

Element	Ag	Al	As	Au	Ba	Be
Unit	ppm	%	ppm	ppb	ppm	ppm
LOD	0.05	0.01	0.5	2	1	0.1
Method	INAA, ICP, & ICP/MS	ICP	INAA	INAA	INAA & ICP/MS	ICP & ICP/MS
769129	0.06	2.22	1.5	5	749	3.2
769133	0.06	2.65	0.9	< 2	560	2.9
769136	0.08	2.52	2.4	< 2	1070	3.9
769139	0.08	1.42	3.3	8	954	4.8
769141	0.05	1.7	3.5	< 2	652	3.4
Element	Bi	Br	Ca	Cd	Ce	Co
Unit	ppm	ppm	%	ppm	ppm	ppm
LOD	0.1	0.5	0.01	0.1	0.1	0.1
Method	ICP & ICP/MS	INAA	ICP	ICP & ICP/MS	INAA & ICP/MS	INAA & ICP/MS
769129	< 0.1	< 0.5	9.36	0.3	182	79.2
769133	< 0.1	< 0.5	7.11	0.2	141	92.8
769136	0.1	< 0.5	8.26	0.2	219	74.7
769139	< 0.1	< 0.5	9.08	0.3	315	83.6
769141	< 0.1	< 0.5	8.89	0.1	205	82.3
Element	Cr	Cs	Cu	Dy	Er	Eu
Unit	ppm	ppm	ppm	ppm	ppm	ppm
LOD	1	0.05	0.2	0.1	0.1	0.05
Method	INAA & ICP/MS	INAA & ICP/MS	ICP & ICP/MS	ICP/MS	ICP/MS	INAA & ICP/MS
769129	418	2	118	7.7	2.4	5.3
769133	696	2.85	102	5.9	2	3.6
769136	599	2.63	79.6	7.9	2.5	5.16
769139	341	1.05	105	12.5	3.8	8.65
769141	606	2.6	64	6.2	2	4.51
Element	Fe	Ga	Gd	Ge	Hf	Hg
Unit	%	ppm	ppm	ppm	ppm	ppb
LOD	0.01	0.1	0.1	0.1	0.1	10
Method	INAA	ICP/MS	ICP/MS	ICP/MS	INAA & ICP/MS	ICP/MS
769129	11.3	15	14.3	< 0.1	0.5	70
769133	10.6	11.5	10.2	< 0.1	0.2	60
769136	9.85	11.7	14.2	< 0.1	0.3	70
769139	12	15.3	25	< 0.1	0.3	70
769141	8.68	9.3	13.8	< 0.1	0.1	70

Element	Ho	In	Ir	K	La	Li
Unit	ppm	ppm	ppb	%	ppm	ppm
LOD	0.1	0.1	5	0.01	0.1	0.5
Method	ICP/MS	ICP/MS	INAA	ICP	INAA & ICP/MS	ICP/MS
769129	1.2	<0.1	< 5	1.85	78.5	10
769133	0.9	< 0.1	< 5	1.3	68.1	9.7
769136	1.2	< 0.1	< 5	1.83	99.5	18.6
769139	1.9	0.1	< 5	1.53	118	20.8
769141	0.9	< 0.1	< 5	1.39	93.3	31.8

Element	Lu	Mg	Mn	Mo	Na	Nb
Unit	ppm	%	ppm	ppm	%	ppm
LOD	0.1	0.01	1	1	0.01	0.1
Method	ICP/MS	ICP	ICP	ICP	INAA	ICP/MS
769129	0.2	7.37	1360	< 1	0.48	0.1
769133	0.2	10.1	1480	< 1	0.42	0.3
769136	0.2	8.81	1450	< 1	0.9	0.2
769139	0.3	7.19	1850	< 1	0.21	0.2
769141	0.2	7.73	1280	< 1	1.48	1.1

Element	Nd	Ni	P	Pb	Pr	Rb
Unit	ppm	ppm	%	ppm	ppm	ppm
LOD	0.1	0.5	0.001	0.5	0.1	0.2
Method	INAA & ICP/MS	INAA, ICP, & ICP/MS	ICP	ICP & ICP/MS	ICP/MS	INAA & ICP/MS
769129	105	302	0.081	5.6	24.2	59
769133	72.8	599	0.165	6.3	17.7	46.1
769136	111	457	0.106	10.9	26.5	71.7
769139	179	345	0.075	8.2	40.7	43.8
769141	103	519	0.098	4.4	24.9	67.2

Element	Re	S	Sb	Sc	Se	Sm
Unit	ppm	%	ppm	ppm	ppm	ppm
LOD	0.001	0.01	0.1	0.1	0.1	0.1
Method	ICP/MS	ICP	INAA	INAA	INAA & ICP/MS	INAA & ICP/MS
769129	< 0.001	0.03	< 0.1	23.3	0.4	20.7
769133	< 0.001	0.05	< 0.1	23.9	0.5	14.8
769136	< 0.001	0.03	< 0.1	21.3	0.5	22.4
769139	< 0.001	0.04	0.2	14.1	0.3	36.9
769141	< 0.001	0.07	0.6	16.6	0.5	18.8

Element	Sn	Sr	Ta	Tb	Te	Th
Unit	ppm	ppm	ppm	ppm	ppm	ppm
LOD	1	0.2	0.1	0.1	0.1	0.1
Method	ICP/MS	ICP/MS	INAA & ICP/MS	INAA & ICP/MS	ICP/MS	INAA & ICP/MS
769129	< 1	> 1000	< 0.1	1.4	< 0.1	7.9
769133	< 1	694	< 0.1	1	< 0.1	8.5
769136	< 1	870	< 0.1	1.4	< 0.1	14.7
769139	< 1	> 1000	< 0.1	2.3	< 0.1	14.9
769141	< 1	876	< 0.1	1.1	< 0.1	13.7

Element	Ti	Tl	Tm	U	V	W
Unit	%	ppm	ppm	ppm	ppm	ppm
LOD	0.01	0.05	0.1	0.1	2	1
Method	ICP	ICP/MS	ICP/MS	INAA & ICP/MS	ICP	INAA
769129	0.17	0.37	0.3	2.4	83	< 1
769133	0.16	0.46	0.2	2.6	55	< 1
769136	0.17	0.47	0.3	4.5	61	< 1
769139	0.21	1.04	0.4	5.2	98	< 1
769141	0.47	0.78	0.2	2.7	109	< 1

Element	Y	Yb	Zn	Zr
Unit	ppm	ppm	ppm	ppm
LOD	0.1	0.1	0.5	1
Method	ICP/MS	INAA & ICP/MS	INAA, ICP, & ICP/MS	ICP/MS
769129	24	1.5	111	30
769133	20.8	1.5	103	10
769136	26	1.8	100	19
769139	37.4	2.3	136	22
769141	20.8	1.5	89.3	8

Appendix F – List of figure images and associated sample information (sample ID, drill hole number, and depth in drill hole).

Figure	Sample ID	Drill hole	From (m)	To (m)
2.2d	N/A	SD-18-264	N/A	N/A
2.3a	ASP_02B	SD-14-05	158.71	159
2.3b	N/A	SD-18-229	N/A	N/A
2.4a	ASP_06B	SD-16-40	228.08	228.28
2.4b	ASP_02B	SD-14-05	158.71	159
2.4c	JSZ_06F	SD-14-04	271.35	271.45
2.4d	ASP_04B	HS-15-31	351.32	351.52
2.4e	ASP_02B	SD-14-05	158.71	159
2.4f	ASP_02B	SD-14-05	158.71	159
2.5a	JSZ_06C	SD-14-04	264.92	265.03
2.5b	JSZ_16A	SD-18-229	282.1	282.3
2.5c	JSZ_16A	SD-18-229	282.1	282.3
2.5d	JSZ_16A	SD-18-229	282.1	282.3
2.6a	MA_08A	SD-17-110	113.45	113.68
2.6b	JSZ_05A	SD-15-11	216.48	216.6
2.6c	QT_03C	SD-18-225	200.78	200.9
2.6d	JSZ_05A	SD-15-11	216.48	216.6
2.6e	MA_04B	SD-17-78	55.55	55.63
2.7a	JSZ_05A	SD-15-11	216.48	216.6
2.7b	MA_12A	SD-17-88	110.25	110.46
2.7c	MA_04B	SD-17-78	55.55	55.63
2.8a	ASP_07B	DG-17-54	49.33	49.5
2.8b	JSZ_06A	SD-14-04	256.6	256.76
2.8c	ASP_03	SD-14-03	256.83	256.93
2.8d	ASP_01A	SD-17-97	215.68	215.85
2.8e	JSZ_05A	SD-15-11	216.48	216.6
2.8f	MA_12A	SD-17-88	110.25	110.46
2.11	ASP_02B	SD-14-05	158.71	159
2.12	ASP_03	SD-14-03	256.83	256.93
2.13	JSZ_16A	SD-18-229	282.1	282.3
3.2d	LAMP_07F	SD-18-243	230.2	230.3
3.2e	LAMP_07F	SD-18-243	230.2	230.3
3.2f	LAMP_07F	SD-18-243	230.2	230.3
3.3a	ASP_02B	SD-14-05	158.71	159
3.3b	ASP_07B	DG-17-54	49.33	49.5
3.3c	JSZ_06G	SD-14-04	275.33	275.45
3.3d	JSZ_06G	SD-14-04	275.33	275.45
3.3e	MA_01C	SD-17-101	226.12	226.31
3.3f	JSZ_05A	SD-15-11	216.48	216.6
3.4a	MA_08E	SD-17-110	122.9	123
3.4b	JSZ_05A	SD-15-11	216.48	216.6
3.4c	MA_01B	SD-17-101	222.61	222.79
3.4d	MA_11A	SD-17-106	137.28	137.4
3.4e	QT_03C	SD-18-225	200.78	200.9

Figure	Sample ID	Drill hole	From (m)	To (m)
3.4f	JSZ_05A	SD-15-11	216.48	216.6
3.5a	MA_11B	SD-17-106	137.9	138
3.5b	MA_11B	SD-17-106	137.9	138
3.5c	QT_03C	SD-18-225	200.78	200.9
3.4f	JSZ_05A	SD-15-11	216.48	216.6
3.5a	MA_11B	SD-17-106	137.9	138
3.5b	MA_11B	SD-17-106	137.9	138
3.5c	QT_03C	SD-18-225	200.78	200.9
3.6b	LAMP_07F	SD-18-243	230.2	230.3
3.6c	JSZ_08A	SD-17-104	181.57	181.75
3.6d	LAMP_02B	SD-17-90	167.8	168
3.7a	JSZ_05A	SD-15-11	216.48	216.6
3.7b	JSZ_05A	SD-15-11	216.48	216.6
3.7c	JSZ_05A	SD-15-11	216.48	216.6
3.7d	JSZ_05A	SD-15-11	216.48	216.6
3.7e	N/A	SD-15-11	195.5	195.6
3.8a	MA_12A	SD-17-88	110.25	110.46
3.8b	MA_01A	SD-17-101	207.06	207.16
3.8c	MA_12A	SD-17-88	110.25	110.46
3.8d	MA_11C	SD-17-106	142.38	142.6
3.8e	MA_04B	SD-17-78	55.55	55.63

VITA AUCTORIS

NAME:	Elliot A. Wehrle
PLACE OF BIRTH:	Ottawa, ON
YEAR OF BIRTH:	1996
EDUCATION:	St. Mother Teresa High School, Ottawa, ON, 2014
	Laurentian University, Hons. B.Sc. Earth Sciences, Sudbury, ON, 2018